An Investigation of Ferroelectric and Ferromagnetic Oxide Systems

Fatma Abdulhalim Shanaishah

School of Science and Technology

A thesis submitted in partial fulfillment of the requirements of Nottingham Trent University for the degree of

Doctor of Philosophy

May 2022

DEDICATION

I grant great thank to the Almighty Allah, for everything that has happened in my life.

I dedicate this thesis to ***my glorious father*** (***Abdulhalim***), who has planted me on the path which made me to realize my dreams and I extend my great gratitude to him, for all his great efforts and his attentions, for all the years of my study.

I dedicate this thesis ***purely to my mother's spirit*** (***Khadija***), and I extend the great thanks to her help and support to me during her short life.

I dedicate this thesis to the most beautiful thing in my life ***my daughter (Amira)***, who is the eternal smile that has painted the predestination on my lips, and I extend my greatest thank to her for making me happy.

Finally, I also dedicate this thesis to ***my sisters, brothers and their children***, particularly my sister (***Halima***), who always helped me, and to all my family great thanks.

ACKNOWLEDEMENTS

The work described in this thesis was carried out at Nottingham Trent University, while the researcher was working as a full-time doctoral research student.

I owe my utmost sincere gratitude to my honorable director of studies and patience with me, ***Dr Gareth Cave*** for his guidance over the last four years. Also, I apologize to him for any dereliction during the study period. He was very kind, and he always helps me to resolve any problem. His office was always open for me for any inquiry despite his many responsibilities. Also, his relentless effort and extensive suggestions around my work were indispensable to the accomplishment of this research.

I Thanks God that my second supervisor was ***Prof. Brown, Carl***, where he was also very pleasant. I would like to extend a huge thank to him for his advice, support, feedback, and knowledge throughout the development of my thesis.

The financial support of School of Science and Technology at Nottingham Trent University to participate in some various conferences, where all employees are doing what they can to provide comfort for the students during the study period. Therefore, special thanks and appreciation for all the staff in the Office of Graduate Studies.

I would also like to thank many of the people who have help me over the years and my colleagues in Nottingham Trent University.

Fatma Abdulhalim Shanaishah

May 2022

Abstract

This work presents an experimental study of perovskites, in terms of the structural, dielectric, and magnetic and optical properties. Perovskites are interesting materials to simultaneously have dielectric, magnetic properties known as Multiferroic material; these properties emerge from the coupling of spin, charge, and orbital degrees of freedom. In this work, solid state method was used to prepare the samples at three different sintering temperatures 800^0C, 850℃ and 875^0C at ambient pressure to determine the effect of sintering temperature on the varying value of x=0.0 to 0.2 in the perovskite structure. The compounds $Bi_2Mn_xNi_{2-x}O_6$, $Bi_2Mn_xCo_{2-x}O_6$ and $Bi_2Mn_xZn_{2-x}O_6$ observed to have better dielectric, magnetic and optical properties as a function of varying x values as confirmed by X-ray diffraction and Rietveld refinement for structural analysis, dielectric measurement for electrical properties and magnetic moment spectroscopy for magnetic properties. However, the addition of Mn in the $BiNiO_3$, $BiCoO_3$ and $BiZnO_3$ resulted in the formation of many impurities, and it was difficult to achieve single phase in any composition. The electrical properties of all compounds showed improvement in conductivity with the rise in frequency which indicates better conductive properties with the Mn addition and shows good semiconductor nature. The magnetic moment analysis at room temperature of all compounds showed that the antiferromagnetic material become ferromagnetic with the increasing content of Mn.

Contents

List of Figures

List of Tables

1 Introduction

1.1 Background

The research in inorganic chemistry has expanded rapidly, particularly in areas of materials science. Materials science generates renewed knowledge and aims to obtain new materials with distinctive properties. The earth's crust consists of materials, and these have led the researcher's interests in studying many of these materials for use in everyday life. Majority of materials are of great importance such as oxides, which represent one of the most widely studied groups of materials.

In the late nineteen fifties, there have been investigations about a wide range of physical properties *e.g.,* in magnetic and electrical.[1-3] These characteristics differ from one material to another and with the development of electronic technology. These properties are of interest for diverse applications, where composite materials have commonly been used in electronic devices that require higher densities, limited space, and multifunctional.[4-6] This work focuses on materials that have ferroelectric and ferromagnetic properties simultaneously which are known as multiferroic materials. These materials have generated a great deal of attention regarding storage media manufacture.[7-11] Although the possibility of coexistence of these properties together is unique in itself, their existence in a single material has been studied widely but rarely observed.[12-14] These properties also have been applied in several applications. For example, magnetic–electric sensors in radio-electronics, optoelectronics, microwave electronics, transducers, and compact electrical filters for suppressing electromagnetic interference (EMI).[4-6]

This thesis is leads towards the applications in experiential study of multiferroic material named perovskites materials, in terms of the structure and properties. Perovskite-type transition metal oxides are of huge significance due to their dielectric, magnetic and the transport properties which emerge from the coupling of spin, charge and orbital degrees of freedom. Several attractive properties can be presented in the literature review which explaining transition metal, ferroelectricity and ferromagnetism and perovskites materials.

1.2 Literature Review

1.2.1 Transition Metal Oxides

Transition metal oxides constitute one of the most exciting categories of inorganic solid. These oxides also display an extensive range of phenomena, structures and characteristics. The exceptional characteristics of transition metal oxides are due to the unique nature of the valence d electrons structure of the base transition metal and its bonding with oxygen.[15-17] The electrons such as s and p electrons behave in the manner of collective electron model while the f electrons which are bonded strongly to the nuclei behave by localized electron model. The d electrons of outer shell are not monitored from the neighbouring atoms or by the outer core electrons, and these electrons show intermediate characters and behave as localized electrons in some oxides, and in some oxides behave as collective electrons; in a few instances both electrons can also exist simultaneously.[16] Because the nature of Transition metal oxides it can become complicated. It states with an understanding of the relationship between their complex properties and their electrical and physical structure, in order to comprehend the behaviour of all other inorganic solids.[15,16] Therefore, the study of transition electron has been a subject by chemists and other scientists interested in solid state materials.[16]

Transition metals oxides are also have been of great interest because of the fact that the same electron, which is originally lined with the d orbitals of transition ions, is the reason not only of the excellent magnetic properties, but also the electrical and low-energy optical properties of transition metal oxides. For example, the d electron in the transition metals which is the mainly responsible for the magnetic properties is overlapped by the s band from above and below, and s band is mainly responsible for metallic properties in which the d electrons are primarily responsible for the magnetic properties. As a result, the study of electrical properties investigates the s band and provides us the information of d band.[18] The most important properties of these materials are electronic and magnetic properties; they are also highly dependent on material defects such as dislocations, vacancies, grain boundaries and stacking faults.[19]

The transition metals are complicated to understand but are simpler in one respect, in that it is the s band that spreads the anti-bonding orbitals between anions and cations and increases its energy, so that the orbital is empty and starts with a few eV above the Fermi energy. The band of oxygen ions is of the great interest, which is 2p band, arising from the bonding orbitals which are filled and ends with the few eV below the Fermi energy level. Thus, only the d-electrons states are nearer the Fermi energy and all the low-energy research investigates the d-band only.[18]

Generally, transition metal oxides have a formula which is M_xO_y where x= 1, 2, …, n and y=2x, these oxides formula are different from each other in terms of bonding and the crystal structure; where the transition metal oxides are held together by three types of chemical bonding: Ionic bonding, Covalent bonding and Metallic bonding. These bonds are explained below:

- The first type is ionic bonding (*e.g.*, NiO, CoO), which arises between two different atoms with the ability to gain or lose electrons. The bonding occurs between the positive and negative ions of those atoms, from an electric attraction power between them.[16,20,21] In the sense explained The Ionic bonds occurs between charged particles either in atoms or groups

of atoms. It normally takes place between metal and non-metal atoms. In general, there are 1, 2, or 3 electrons in the outer shell of metals and 5, 6, or 7 electrons in the outermost shell of non-metals. The outermost shell atoms are unstable and partially filled. An electron in outer shell of metal atoms will transfer to non-metal outer shell in to order to become stable. The loss of electrons results in an empty outer shell or close to empty outer shell. This is the preferred states of the metal atom because the next energy shell with lower energy is a stable with completely filled shell. The atoms which gain an electron become negatively charged ions, also known as anions, because the added electron has a negative charge and has more electrons than protons. However, the atom which losses the electron become positively charged ion also known as cations. These cations and anions are held together because of the attraction of opposite charged particles.[22] The most common example of ionic bonding is NaCl shown in Figure (1.1).[23]

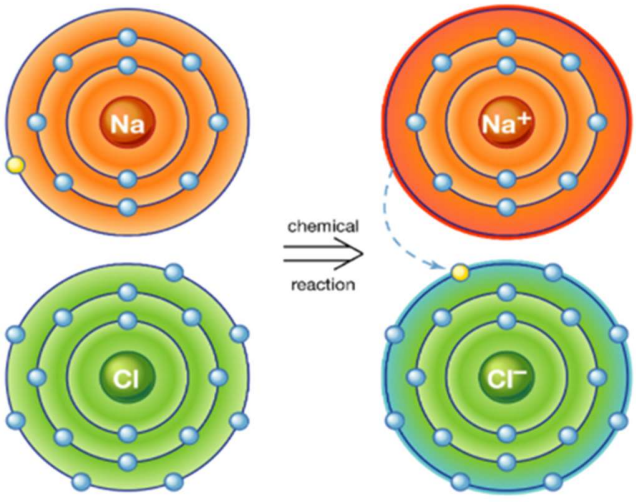

Figure 1.1: The ionic bonding of NaCl.[23]

- The second type is covalent bonding (*e.g.* OsO_4, RuO_2), this bond is formed between the non-metals atoms and the sharing of two or more

electrons. In general, the nonmetals except boron have 4 or more electrons in their outermost shells. Thus, more energy is required to form a bond between the two non-metal atoms with this proportion of electrons in outermost shell. Hence, both atoms have a shared pair of electrons. Both the atoms provide an electron from their outer shell to other atom and thus both are bonded together via a shared electron pair.[8,16,21,22] The example of covalent bond is shown in Figure (1.2).

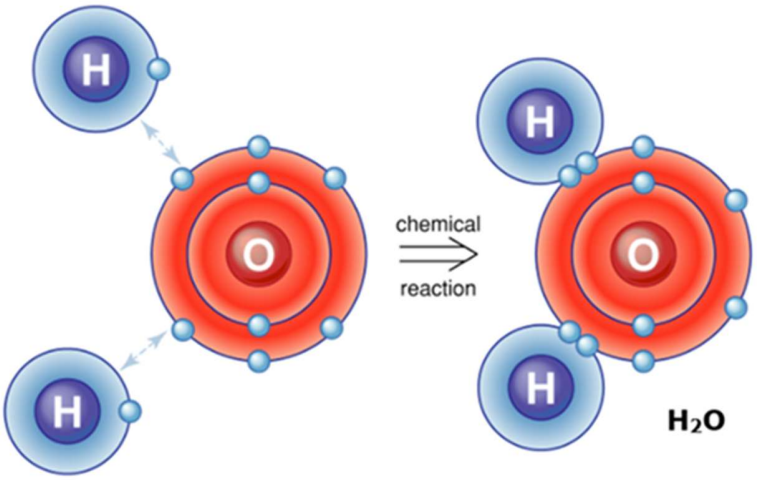

Figure 1.2: The covalent bonding of H_2O.[24]

- The third type is metallic bonding (*e.g.* TiO, NbO, and ReO_3), where in the chemical bond occurs between two metals, and the resultant forces from an electrical attraction between the positive ions and the negatively charged electrons. This bonding, metallic crystal is completely due to the band structure of the oxide and gives rise to metallic-like properties such as conductivity.[8-16,21] The metallic elements typically contain between one and three electrons in their outer shell. The bond between these electrons and to their nucleus is relatively weak. Therefore, the electron from outer shell leaves the atom and form an electro positive ion. The valance electron in this arrangement has good mobility and can conduct electricity and heat. In the case of aluminium, atoms lose two electrons and have a

positive charge in the end and are designated as Al^{3+}. These ions are held together but repel each other because the positive charge attracts the negative charged ions. This result in an arrangement of shared cation electrons in a regular pattern which is the crystalline structure of metal atoms.[25] The example of metallic bonding is shown in Figure (1.3).

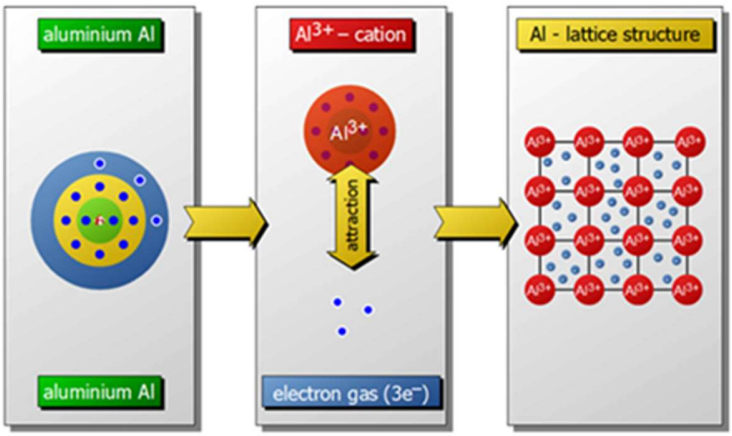

Figure 1.3: The metallic bonding between Al^{3+} ions.[26]

With regard to the crystal structure of the transition metal oxides, where several of these oxides appear to transform from one crystalline phase to another; different phases of the oxides demonstrate changes in electrical, magnetic, as well as other properties.[16] In addition, some of the structures have an important role in the classification of complex structures of transition metal oxides; five structures are considered a basis in the crystal chemistry of these oxides. The oxides of transition metals have simple formulas and metals occur in one oxidation states, for example M_2O, MO and M_2O_3. Some oxides also show formula of this type, *e.g*. M_3O_4, in which both $M^{2+}$and M^{3+} exist. These stoichiometric oxides have more complex oxidation states in which the metals present two oxidation states and have a number of examples of it, Mn_5O_8, V_6O_{13}, and Cr_5O_{12}. Furthermore, an extensive series of oxides is formed by some metals for example Ti_nO_{2n-1} or Mo_nO_{3n} with simple oxides structures, such as MO_2 or MO_3.[2] The different types of crystal structures with respect to different stoichiometries

are shown in Figure (1.4). These basic structures are the rock salt, rutile, cuprite, fluorite, and corundum type structures.[15]

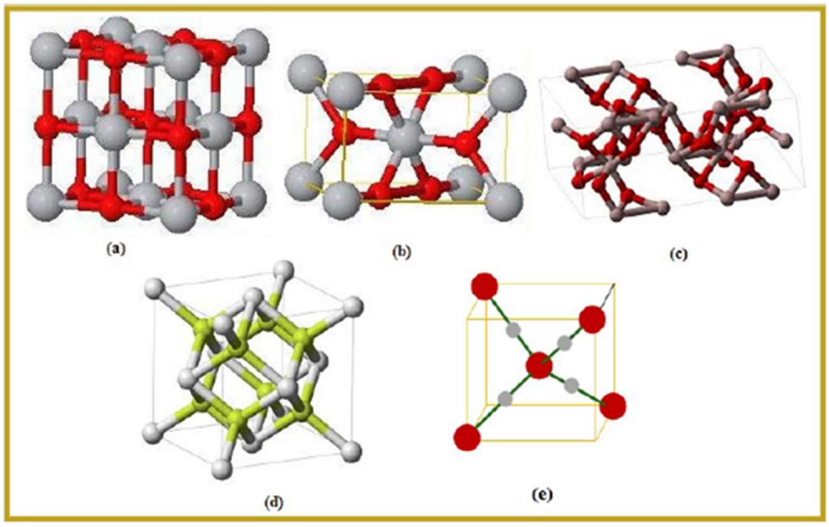

Figure 1.4: The crystal structure of (a) rock salt,(b) rutile, (c) corundum, (d) fluorite, (e) cuprite (the corner grey ions are anions and the other ones are cations, and in (e) red are anions and the grey are cations).

The simplest structure in transition metal is rock salt (NaCl) structure as shown in figure 1.4a which is normally adopted by NaCl. The other oxides can adopt a wurtzite structure normally observed in ZnO (similar to NaCl) and Cuprite structure as shown in figure 1.4(e), which is normally observed in CuO and PdO. This structure has metal cations surrounded by the square planar coordination. In NbO, a unique structure has been observed in which both Nb and O have four alternatively positioned coplanar bonds in one of the simplest 3D connected nets.[27] In other words, this stricture is referred as a defect in rock salt structure by having three NbO the unit cell. One of the two simple structures such as fluorite and rutile as shown in figure 1.4b and d, are adopted by most of the transition metal dioxides. In fluorite structure, the larger M^{4+} cations are octa-coordinated and in the rutile structure the smaller M^{4+} are hexacoordinated. Each M^{4+} in the normal rutile form is equally distant from each other in every chain of octahedra. V, Nb, Mo, Tc, W, and Re dioxide are crystalized with less symmetrical structural variants and show the successive metal atoms pairs which are closed

together alternatively and further apart. The electrical conductivity of these structures is related to this closed linking of these metal atoms. The crystal structures corundum as shown in figure 1.4c is adopted by these compounds of C-M_2O_3 type. It is depicted as the oxide anions have hexagonally closed packed array in which the two-thirds octahedral holes are occupied by M^{3+} cations. On the other hand, it is also known that C-M_2O_3 is derived from fluorite with the removal of one-quarter of the anions that form two types of distorted octahedral.[27] Transition metal oxides have been characterised as having numerous types of complex structures such as pyrochlore, spinel, perovskite and hexagonal ferrite structures.[15] Despite the fact that transition metal oxides are widely studied, they are still not fully understood.[28-30]

1.2.2 The Perovskites

Perovskites have received considerable attention, because they have useful physical characteristics such as superconductivity, ionic conductivity, and a multitude of dielectric properties, which can be used in many important fields,[31] such as in the field of microelectronics and superconductors and giving them enormous commercial importance.[32] Perovskites are named after L. A. Perovski, who identified perovskite structure and named the mineral calcium-titanium oxide ($CaTiO_3$) as perovskite. Moreover, perovskites have general formula ABO_3, where A and B are cations while X is an anion. The A and B cations can have a variety of charges and in the original perovskite mineral ($CaTiO_3$) the A cation is divalent and the B cation is tetravalent, where both the A and B cations adopt a trivalent state, the A cations are restricted to being rare earths.[32] For example, the $SrTiO_3$ is a perovskite, which has a cubic structure with the strontium and titanium atoms indicated as the A cation and B cations respectively. Figure (1.5) illustrates the perovskite structure with the A and B cations at the unit cell origin. This figure shows the coordination of the perovskite structure, wherein the B cation is octahedral while the A cation is 12-fold.[8,33]

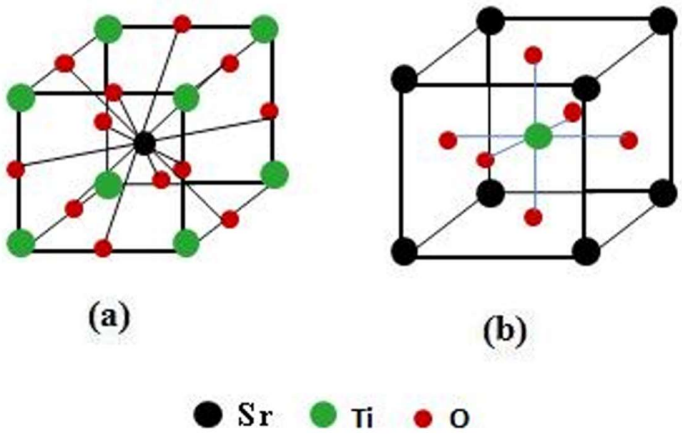

Figure 1.5: The perovskite structure of $SrTiO_3$ at the B (a) and A (b) cations.

The simple perovskite structure, represented by $SrTiO_3$, has a cubic symmetry (space group $Pm\bar{3}m$) as illustratedin Figure (1.5).[34] Generally, the ABO_3 perovskite structures are distorted and do not have cubic symmetry such as $CaTiO_3$. Table (1.1) shows stoichiometric ABO_3 perovskites, which are divided into three classes according to the oxidation state of the A and B elements.[15]

Table 1.1: Stoichiometric ABO_3 perovskites.[15]

$A^IB^VO_3$		$A^{II}B^{IV}O_3$		$A^{III}B^{III}O_3$	
A	**B**	**A**	**B**	**A**	**B**
Na	Nb	Ba	Ti	Ln	Fe
Ag	Ta	Sr	Sn	Bi	Cr
K	I	Ca	Zr	Y	Co
		Pa	Hf		Mn
Rare		**Rare**	Mn		Ti
Rb		Cd	Mo		V
Tl			Th		Al
Cs			Fe		Sc
			Ce		Ga
			Pr		In
			U		V

Distortions of most perovskite oxides are usually caused by cation displacements inside the octahedra and tilting of these surfaces, which is related to the properties of the A and B replaced cations. There are factors that contribute to the distortion in the perovskite structures including radius size effects and the Jahn-teller effect.[35] Studies have been conducted to understand distortions from the cubic structure of the ABO_3 perovskites of oxides are purely ionic. Considering the structural geometry, the first of these was a study of octahedral tilting distortions in 1926 by Goldschmidt.[35] According to Goldschmidt, there is relation between the radii of A, B, and O^{2-} ions that determines the degree of distortion in the ABO_3 perovskites, this relationship is described by the following equation:

$$t = (R_A + R_B)/\sqrt{2}\,(R_B + R_O) \qquad (1.1)$$

where t is the tolerance factor, R_A is the ionic radius of A, R_B is the ionic radiuof B, and R_O is the ionic radius of oxygen.[36,37]

There are three assumptions for the calculation of the degree of distortion or tolerance factor. Firstly, the ionic sizes are absolute; secondly the structure is electrically neutral; finally, the summation of charges on A and B cations is 6. The value of tolerance factor for all types of perovskite structures was found to lie between 0:80 and 1:00. For example, in ilmenite, which is a weak magnetic metal oxide, and has a chemical composition of $FeTiO_3$, where the lower value of the tolerance factor t must be bigger than 0:89 for the model cubic structure. In each of the crystals, the effective ionic radii are not constant, and for this reason the use of a self-consistent set of these radii does not allow the use of tolerance factor to forecast an outcome close to model structure, and it is not impossible to compare two series of perovskites in which both A and B have been changed.[36]

Most of the oxides which have ferroelectric properties are found as shown in first and second column ($A^{I}B^{V}O_3$) and ($A^{II}B^{IV}O_3$) of table (1.1). These series of oxides

are distinguished by small distortions of the cubic cell, for example, $BaTiO_3$, which was found to be a typical example of perovskite structure and has several useful properties such as electrical properties such as high dielectric constant.[38] For this reason, $BaTiO_3$ perovskite is used in several technological applications for example multilayer ceramic capacitors.[39] The perovskite structure of this oxide is a tetragonal cell when prepared at room temperature. This is the result of the process of changing the titanium from the center of the TiO_6 octahedron leading to a non-coincidence of the centers of positive charges (cations) and negative charges (anions), as shown in Figure (1.6).[15,40] This type of perovskite structure is the first class of titanium inside its octahedron, which creates a permanent dipoles moment which orientation can be reversed in the electric field direction, thus obtaining ferroelectric perovskite structure.[15]

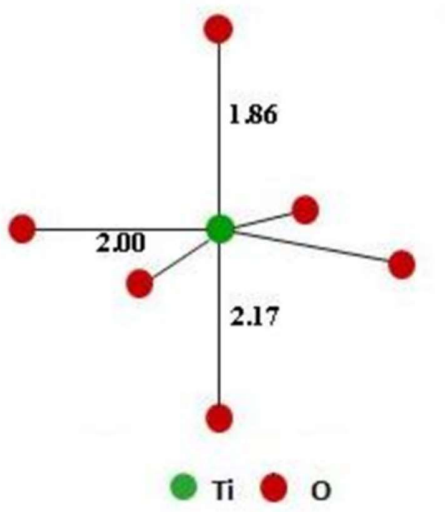

Figure 1.6: Tetragonal $BaTiO_3$ showing distortion of TiO_6 octahedron.

However, most perovskites structures in the third column ($A^{III}B^{III}O_3$), displayed in table (1.1), have a different kind of distortion and are orthorhombic. An example of this is $GdFeO_3$, which is shown in Figure (1.7).

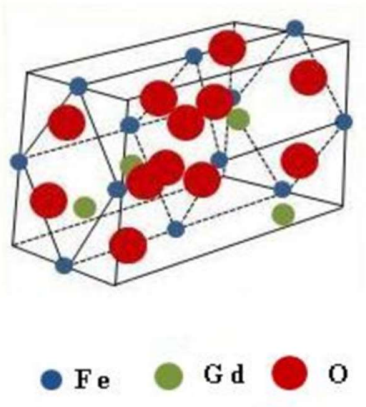

Figure 1.7: The orthorhombic structure of $GdFeO_3$.

The orthorhombic cell of this perovskite structure has the following parameters:

$$a \approx a_p\sqrt{2}, b \approx a_p\sqrt{2}n, c \approx 2a_p$$

where is the parameter of the cubic cell of perovskite.[41]

In addition, there are other perovskite structures such as quaternary perovskite oxides that are the subject of this thesis which are described in Section (1.2.5). These perovskite oxides can have two or more cations. A complicated looking formula such as La_2MgRuO_6 can be rewritten as $La(Ru_{\frac{1}{2}}Mg_{\frac{1}{2}})O_3$, in which a perovskite with La is on the A site and a mixture of Ru and Mg are on the B sites.[33] As such there are millions of potential materials, each with a specific stoichiometry. However, it does not follow that a material with the correct stoichiometry will necessarily have a perovskite structure.

1.2.3 Ferromagnetic Materials

Magnetic properties of materials arise from the interaction between the atomic centers in the extended lattice. A ferromagnetic material is one in which all the

unpaired electrons align themselves parallel in the absence of external magnetic field.[42] Moreover, the extent of this effect in ferromagnetic material inside the external magnetic field is very large. Sections of these materials may retain magnetism despite the disappearance of the external magnetic field, and hence convert into permanent magnets, or they may lose magnetism upon removal of the magnetic field (paramagnetic). Ferromagnetism occurs as a result of the spontaneous direction for permanent magnetic dipoles in material, which result from the spin movement of electrons, where a group of magnetic dipoles couple to induce a magnetic field. Thus, they constitute nano-metric scale magnetic particles called magnetic domains. These magnetic domains are separated from each by walls as shown in Figure (1.8).[43] Therefore, ferromagnetic materials are defined as those materials that are subject to a transition from a high-temperature phase which have no macroscopic magnetic moment to the low-temperature phase containing a spontaneous magnetization even in the absence of an applied magnetic field.[7,44]

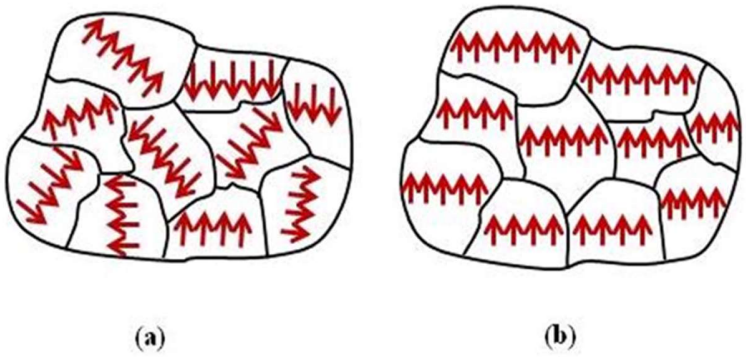

Figure 1.8: The behaviour of ferromagnetic materials (a) without magnetic field B_o (randomly oriented arrows) and (b) with magnetic field (aligned arrows in same direction).[43]

Magnetic properties are generally found in metals, where their compounds have partially filled d orbitals and often a proportion of unpaired electrons engaging these orbitals.[33,45] Ferromagnetism occurs from disparity of the electrons spin, where this disparity of spin, whether up or down, produces a magnetic moment

in a material. If the materials have the same number of up-spin and down-spin of electrons, it means that these materials are non-magnetic such as copper. Where the electrons of these materials take a place in the top level of the filled state; this level is called the Fermi level, then cannot be found any magnetic moment and the electrons are un-polarized. While if the materials have an imbalance of the spin, it produces a magnetic moment, then the materials become ferromagnetic as has illustrated in Figure (1.9).[45,46]

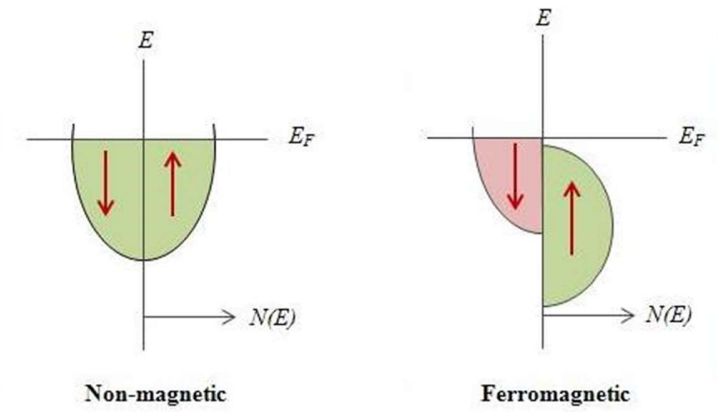

Figure 1.9: A schematic representation of the density of electronic states. Where (E) is the electron energy; (EF) is the Fermi level; N(E) is the density of states.[46]

Due to the exchange interactions, which result from the application of a magnetic field on these materials, the following can occur:

1. The unpaired electrons line up with one another easily in the direction of this field.
2. A strong induction interaction occurs of the materials with this field.
3. Below a certain temperature, these materials remain permanently magnetized even in the absence of an external magnetic field, this temperature is called the Curie temperature.
4. The materials will acquire an important property which is spin polarization (P), which can be calculated from the following equation:

$$P = \frac{n\uparrow - n\downarrow}{n\uparrow + n\downarrow} \qquad (1.2)$$

where ($n\uparrow$) is the number of spin up, and ($n\downarrow$) is the number of spin down.[45,46]

Ferromagnetic materials such as iron (Fe), cobalt (Co) and nickel (Ni), are characterised as, when a correlation occurs between the spin of electrons located in the 3d orbital. The neighboring atoms create the direction of their magnet since all atoms take the same direction that appears in the form of a magnetic field. This occurs only in the iron, cobalt and nickel, because in these materials quantitative interaction occurs between magnetic spins of atoms occurs that its potential energy is minimised when spins are aligned with the same direction.[47,48]

1.2.4 Ferroelectric Materials

A ferroelectric material possesses a permanent dipolar axis, which may only exist under certain conditions, such as pressure and high temperature.[49] A ferroelectric material reveals a hysteresis loop in the connection between polarization and electric field and displays spontaneous polarization in the absence of an external electric field.[7,40] Ferroelectric materials possess permanent dipole moments arising from the absence of a center of symmetry in the crystal structure.[7,40] Furthermore, ferroelectric materials reveal a dielectric constant anomaly at a critical temperature, but this is only observed in the polarization electric field hysteresis loop.[15] The spontaneous polarization above this critical temperature, named as Curie point, Tc, decreases to zero and changes the properties that before as a paraelectric material.[50,51]

In addition, ordinary dielectrics can be characterised as ferroelectric materials; this occurs due to their extremely large permittivity and the possibility of preserving some residual electrical polarization after the disappearance of the applied voltage. Additional augmentation occurs in the potential difference

applied to a dielectric substance; this relative augmentation exists in the form of induced polarization, or stored charge. Figure (1.10) illustrates a simple linear relationship with ferroelectrics; this relationship does not hold.[7,31]

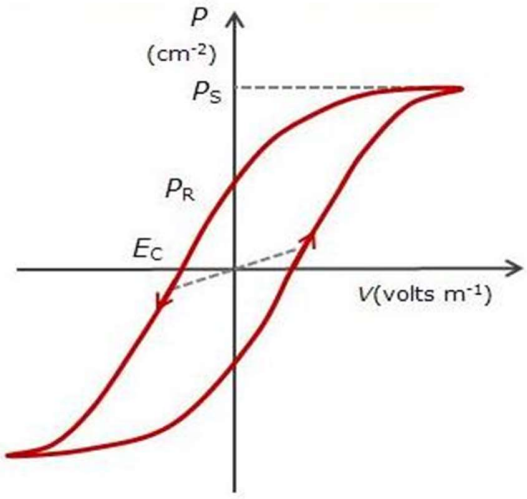

Figure 1.10: Hysteresis loop of a ferroelectric.[7]

As shown in figure (1.10), the relationship between the induced polarization P and the applied voltage V displays a complicated behaviour with a hysteresis loop. P_S is a saturation polarization which is shown exhibited by ferroelectric at high field strength, and P_R is a permanent polarization, which is the value retained as V is reduced to zero after saturation. E_C is the coercive field, which is the reverse field required to reduce the polarization to zero.[31] Ferroelectric materials have a very high permittivity value which is useful for capacitors. Permittivity values change considerably by changing the temperature and applied field strength which normally reaches a peak point at the Curie temperature and falls away at elevated temperatures.[50,51]

The term "Ferroelectric" is the relationship between the electric field and polarization for the ferroelectric material with the electrodes and from a hysteresis loop resembles to magnetic field and magnetization in a ferromagnetic material. There are different models that have been proposed to

elaborate this phenomenon of ferroelectricity, among them the current model is the consideration of the vibrational states of the crystal lattice.[50,51]

Ferroelectric materials undergo a phase transition from a high-temperature phase in which it is an ordinary dielectric to a low temperature phase when the electric polarization induced by applied current returns to zero when the field is removed.[31]

The first ceramic material in which the ferroelectric behaviour was observed was Barium titanate ($BaTiO_3$) which is isostructural with the mineral perovskite ($CaTiO_3$). The ABO_3 type structure can be observed on the basis of Face-Cantered Cubic (FCC) structure of O_2 anions placed at the center of cube faces and A cations at the corner and B cations at the center of cube. This geometry consideration is best fit for the relationship between the ionic radii holds as shown below:[50,51]

$$R_A + R_O = \sqrt{2}(R_B + R_O) \qquad (1.3)$$

This relationship with the perovskite structure is not definitive as due to the small changes in the sizes of the A and B cations. These changes can significantly affect the dielectric properties of perovskite materials.[51] Hence, the above equation (1.3) can be written as:

$$R_A + R_O = t\sqrt{2}(R_B + R_O) \qquad (1.4)$$

where t is the tolerance factor with the normally ranged in 0:95< t <1:060

The unit cell of barium titanate above its Curie point (close to $130\ ^0\mathrm{C}$) is cubic with the ions placed in the way as mentioned above and below the Curie point, the geometry is little distorted to the tetragonal structure with the dipole moment along the c-axis. Other structural transitions take place at temperatures

close to $0\ ^0\mathrm{C}$ and $-80\ ^0\mathrm{C}$.[51] The unit cell, below $0\ ^0\mathrm{C}$, is orthorhombic with the polar axis along the face diagonal and below $-80\ ^0\mathrm{C}$, is rhombohedral with the polar axis parallel to body diagonal as shown in Figure (1.11).[50,51]

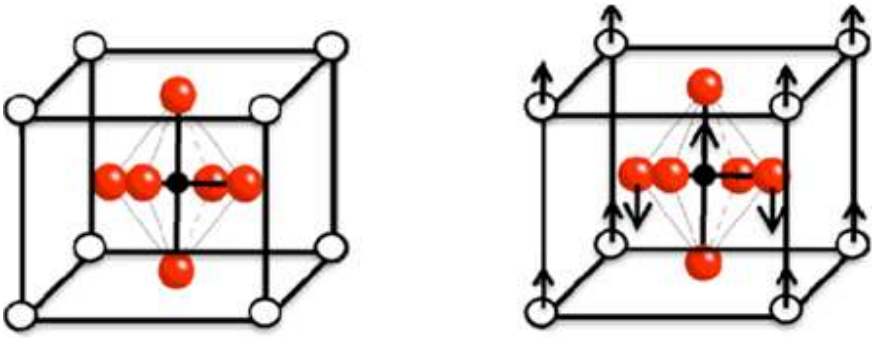

Figure 1.11: Unit cell of barium titanate above and below the Curie point.[52]

In 1943, after the discovery of high permittivity value of ferroelectric barium titanate, the barium titanate ceramics were produced by the conventional methods.[51] And after that the applications of such materials have been expanded broadly and many different ferroelectric materials are developed such as: strontium titanates ($SrTiO_3$), lead magnesium niobate, lead titanate ($PbTiO_3$), lead lanthanum zirconate titanate, lead zirconate titanate, lithium niobate ($LiNbO_3$). The response of ferroelectric materials to both polarization and electric displacement when electric field is applied means that they find applications in data storage, capacitors (due to electric flux density resulting in dielectric permeability), electromechanical transducers and actuators because of the change in shape caused by electric polarization. These are now greatly used in different electronic devices like multilayer capacitors, sensors, electro-optic devices for data storage and displays thermal imaging, thermal switches, radio communication filters ultrasonic transducers, piezoelectric sonar and ferroelectric thin film memories.[31,51]

1.2.5 Related Research

Materials which possess perovskite structures are observed to have ferromagnetism and ferroelectricity properties simultaneously and for that reason these materials are considered to offer potential as multiferroic materials.[53] For example, the $BiMnO_3$ has been found with multiferroic properties when synthesized at high pressure and high temperature. This material has a metastable phase at ambient conditions. The investigation also demonstrated the presence of polymorphism at room temperature, which was evident during the electron diffraction and high-resolution electron microscopy in all the samples.[54]

Sugawara *et al*.[55,56], and Bokov *et al*.[57] studied the perovskite materials and their ferromagnetism properties which was later confirmed by numerous studies such as Chiba *et al*.[58], and Faqir *et al*.[59] The $BiMnO_3$ perovskite has ferromagnetic ordering temperature at ~100 K and substantial magnetization of ~3*:*2 μB per formula unit. Furthermore, two recent structure determinations by room temperature,[60] and low temperature powder neutron diffraction found that crystallization in the non-centrosymmetric *C*2 space group can also create the ferroelectricity.[61]

Baettig *et al*.[53] have studied the behaviour of $BiMnO_3$ perovskite structure, specifically the polar behaviour of these materials analysed by applying first principles density functional (DFT) calculations to the stereochemical activity of the Bi^{3+} $6s^2$ lone pair.[53,62-64] It was observed that off-centering towards the anions in stereo chemically lone pair-active cation is escorted with the charge transfer into proper empty cation states (in Bi 6p orbitals). Off-centering is then stabilized by the resulting covalent bond formation and produces featured lobe-shaped "lone pairs" in the region of the cation as shown in Figure (1.12). However, an unstable zone-center photon was suggested to be ferroelectric behaviour as found by the prior first-principles calculations for the high

symmetry cubic structure.[53] Later, experimentation showed the local Bi-O displacements in fact anti-align,[64] and an almost antiferroelectric structure with small inequivalences between sites was observed with net polarization from ferrielectric arrangements. Ferromagnetism was observed from the unusual orbital ordering because of strain in the lattice introduced by off-centering of the Bi ions.[53]

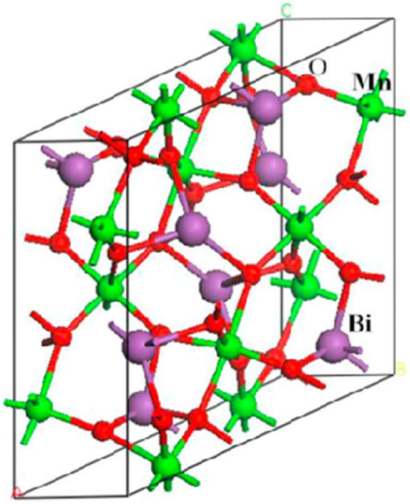

Figure 1.12: Crystal structure of monoclinic $BiMnO_3$: Bi is denoted as large black spheres and Mn as smaller white spheres and O is at six-coordinate.[65]

A different distortion in perovskite basic cell of $BiMnO_3$ with non-centrosymmetric structure was observed and also showed ferroelectric behaviour at room temperature.[12] While the ferroelectric hysteresis loops were found in thin film and bulk samples of $BiMnO_3$. From X-ray powder diffraction, it was found that the compound $BiMnO_3$ was present with the contamination of bismuth oxycarbonate ($Bi_2O_2CO_3$) and traces of $Bi_2Mn_4O_{10}$. The reason was $Bi_2O_2CO_3$ is produced when using a metallic capsule during the synthesis of $BiMnO_3$ and by the CO_2 contamination from graphite heater multianvil apparatus. When the use of metallic capsule was avoided, the bismuth oxide was converted to oxycarbonate, without perovskite formation. To reduce contamination and obtain the best results, the applied pressure was maintained at 40 kbar and the

reaction temperature was reduced to 723 K and further confirmed by Rietveld analysis with the decrease to 10% in moles of undesired products.[12] The origin of ferromagnetism in $BiMnO_3$ was the result of specific orbital ordering which have not been observed in other structures; therefore, it is unknown. However, as per the Kanamori-Goodenough rules, the disturbance of two types of transition metal ions with and without electrons in a rock-salt configuration can help in obtaining a ferromagnetic insulator. The X-ray powder diffraction data showed that the compound Bi_2NiMnO_6 is a heavily distorted double perovskite with Ni^{2+} and Mn^{4+} ions ordered in a rock-salt configuration as shown in Figure (1.13) Therefore, the Bi_2NiMnO_6 is likely to be a ferromagnetic and ferroelectric, but it is difficult to form such compound under ambient conditions.[66]

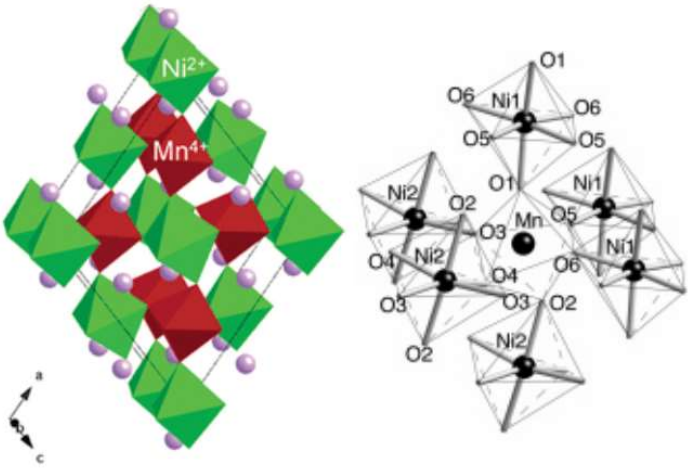

Figure 1.13: Crystal structure of Bi_2NiMnO_6.[66] The green ions showing Ni, red ions are Mn, and purple representing O ions.

The *C*2 symmetry was observed in this compound which was the result of pressure. This symmetry creates spontaneous polarization along the b-axis. The dielectric constant measurement showed that the ferroelectric transition occurs at 485 K in this compound. A ferromagnetic interaction is thought to exist between the adjoining spins.[66]

Another material $BaTiO_3$ has been studied, and has attended much interest.[4] In this compound, no other minority phase have been observed, and leading to the conclusion that there is no chemical reaction between the ferromagnetic components and the ferroelectric components. It was also observed that the ferromagnetic-ferroelectric $BaTiO_3$ composite materials have an excellent response at high frequency, and they are useful for the fabrication of compact electrical filters for suppressing electromagnetic interference (EMI). Furthermore, the initial permeability decreased significantly, and the permittivity increased with the increasing content of $BaTiO_3$.[4]

There are various other investigations in the detection of ferromagnetic-ferroelectric properties in materials such as $BiNiO_3$,[67] $BiCrO_3$,[44] $BiFeO_3$.[68] Through the investigation of $BiCrO_3$ perovskite, it was found that the structure of $BiCrO_3$ at room temperature is a highly distorted perovskite-type one with monoclinic *C*2 symmetry, indicating that $BiCrO_3$ has a polar structure.[44] Moreover, the perovskite of $BiCrO_3$ undergoes a structural phase transition from noncentrosymmetric to centrosymmetric structure occurring at about 420 K. Thus, the structure of $BiCrO_3$ is responsible for its electric polarization and ferromagnetic properties.[44] On the other hand in the investigation of $BiFeO_3$, prepared by rapid sintering of sol-gel derived powders, it was found that ferromagnetism in $BiFeO_3$ was attributed to the lattice distortion induced enhanced spin canting of Fe^{3+} ions at room temperature.[68]

Smolenskii *et al*.[69] synthesized $BiFeO_3$ perovskite as a single-phase multiferroic material, where the behaviour of this compound results in G-type antiferromagnetic below the Neel temperature T_N~643 K. However, it becomes ferroelectric below the Curie temperature $T_C \sim 1103\ K$.[69] A magnetic field around the $BiFeO_3$ compound results in a response to this field, due to the presence of the antiferromagnetic property. At the iron nuclei, the coupling of the directions of the magnetic and electric fields below the magnetic transition temperature

was observed. However, there was not enough coupling at room temperature between the ferroelectric and magnetic orders.[69] Therefore, several investigations have been made efforts to improve the $BiFeO_3$ perovskite to obtain ferroelectric and magnetic properties. For instance, Chen *et al*.[70] has described the fabrication of $BiFeO_3$ ceramics by using sol-gel methods; nevertheless, only minor weak ferromagnetism was observed at room temperature. Other investigations have revealed an efficient way to improve the magnetic properties, by the ion substitution and the room temperature magnetic hysteresis loops that have been found in $BiFeO_3$ doped by Sr, Eu, Gd, Ba, La, and Dy.[71-76]

Xu *et al*.[68] have revealed ferromagnetism in $BiFeO_3$ ceramic at room temperature, which was prepared by the rapid sintering of sol-gel derived powders. The observed ferromagnetism in $BiFeO_3$ was attributed to the enhanced spin canting of Fe^{3+} ions due to the lattice distortion induced by the rapid sintering and cooling process. Zn substitution of Fe improves the dielectric properties, but the room temperature ferromagnetism vanishes. This study reported that both composites have a rhombohedral perovskite structure (R3c), and difficult to obtain a single-phase $BiFeO_3$.[77] In addition, the results have shown that the rapid sintering method was useful in repression of the formation of undesirable phase like $Bi_{36}Fe_2O_{57}$. It was also reported the formation of single phase using high-pressure technique is problematic.[70]

Some oxides are often magnetic, *e.g.*, those containing V^{4+}, and there is an investigation indicating that $PbVO_3$ might be the basis for interesting magnetoelectric materials. $PbVO_3$ has high tetragonal distortions and that might be reason for large polarization of $PbVO_3$. It was observed that insulator-to-metal transition induced by pressure is associated with the tetragonal-to-cubic structural transition in $PbVO_3$.[78]

$MNiO_3$ perovskites (M is rare earth element) have been investigated widely because $MNiO_3$ perovskites are unique properties of metal to insulation transition at high temperatures.[79-82] The orthorhombic $MNiO_3$ perovskites have two transitions, one at T_t of insulation to metal transition and antiferromagnetic order below $TN \leq Tt$. The Rhombohedral $MNiO_3$ perovskites are metallic without long-range magnetic order at lower temperatures. The transition temperature (TMI) increases as the M ion becomes smaller, or when the tolerance factor becomes smaller as shown in Figure (1.14), implying that the related σ- band, comprised of Ni-3d and O-2p orbitals, becomes narrowest as the Ni-O-Ni bond angle reduces.[83]

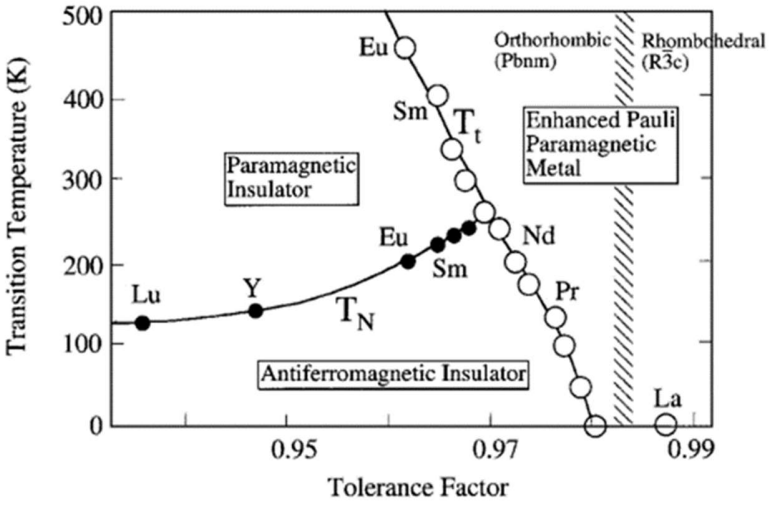

Figure 1.14: Insulator-metal transition T_t and the Néel temperature T_N for the $MNiO_3$ perovskites.[84]

Many of the previous studies using X-ray and neutron diffraction, have proved that the systematic related to the electronic structure in the dielectric phase are complex to some extent. In accordance with Alonso *et al*.[84-86], which investigated the $MNiO_3$ perovskites when M= Lu, Yb, Tm, E, and Ho, have revealed that there is a charge disproportionation to Ni(3+δ) and Ni(3-δ) by using neutron diffraction. This charge disproportionation is associated with an orthorhombic to monoclinic structural change. However, the investigations of $MNiO_3$ perovskites when M= Sm, Nd, and Pr have revealed there is no symmetry change in

perovskite structure,[87] but the lattice volume increases by 0.15 - 0.25% at the transition temperature (TMI). Rodríguez-Carvajal *et al*.[88] have reported that the $PrNiO_3$ perovskite has shown an orthorhombic (metallic) to rhombohedral (metallic) transition only above 700 K, whilst $LaNiO_3$ remained rhombohedral and metallic down to 1.5 K.[87-90] Ishiwata *et al*.[67] have suggested that the replacement of La^{3+} with Bi^{3+}, which resulted in cubic symmetry and metallic structure. Moreover, in this investigation of $BiNiO_3$ perovskite, it was reported that the possibility that the lattice volume might be large enough to make the Bi^{3+} oxide insulating.[53]

Therefore, the Bi^{3+} containing oxide becomes more interesting from the point of view of spin-orbital coupled physics. $BiNiO_3$ perovskite was successfully synthesized under high pressure of 6 GPa and has revealed the presence of the magnetic and electrical properties contrary to the proposed expectations.[53] The obtained data from powder XRD have been reported with a default distorted $GdFeO_3$-type structure.

Finally, Hughes *et al*.[91] have reported that the material, can be designed which demonstrate both ferromagnetic and ferroelectric characteristics simultaneously, but can be complicated due to the contradictory electronic requirements of these properties. In effect, ferromagnetism necessitates the existence of d-electrons, while ferroelectricity in $BaTiO_3$ come from structural displacements caused by the bonding characteristics of the d_0 Ti^{4+} center. The decoupling of the metal centers to overcome ferroelectricity and ferromagnetism can be achieved by using discrete ions in the composition the needed ordering. Ferromagnetism and ferroelectricity properties exist in $BiMnO_3$,[92] but the Mn^{3+} phase can occur only under high pressure, where the orbital ordering of Mn^{3+} brings out the ferromagnetism, while the lone pair at Bi^{3+} produces the ferroelectric distortion.[12,59]

This thesis investigates perovskites, in terms of the structure and properties. Perovskite-type transition metal oxides are of huge significance due to their dielectric, magnetic and the transport properties which emerge from the coupling of spin, charge and orbital degrees of freedom. Several attractive properties can be presented in the transition metal perovskites, such as ferroelectricity and ferromagnetism, which show conversion orientation states.

1.3 Aims and Objectives

The overall aim of this thesis is to investigate the ferromagnetic and ferroelectric behaviour of oxides systems, based on the quaternary perovskite oxide molecular structure. In this work, four different types of quaternary perovskite compositions have prepared with high temperature and ambient pressure to know the effect of high temperature on the varying composition of each quaternary perovskite. In their single-phase form, the quaternary perovskite oxides offer a viable application in data storage media. In order to realize their potential commercial applications, it is important to develop a simple and scalable synthetic route to these novel materials.

The objectives of study:

To achieve the objectives of this research, following aims are needed to be fulfilled which are:

1. To carry out the solid-state mixed oxide synthesis of $Bi_2X_xY_{2-x}O_6$, where X=Mn, Cr or V, while Y= Ni, Co, Cu, Zn, mixed of oxides *via* mortar and pestle, and high pressure followed high temperatures.
2. To determine the structural properties *via* X-ray diffraction, (Rietveld analysis of X-Ray diffraction data)
3. To determine the optical properties *via* UV-vis spectroscopy,
4. To determine the electrical properties *via* dielectric measurements

5. To determine the magnetic properties via magnetic moment measurements.

References

[1] H. Schmid. *Ferroelectrics.*, 1994, **162**, 317-338.

[2] R. Ramesh and N.A. Spaldin. *Nature materials.*, 2007, **6**, 21-29.

[3] G. K. Wertheim and S. Hüfner. *Physical Review Letters.*, 1972, **28**,1028-1031.

[4] H. Zhong and H. Zhang. *Journal of Magnetism and Magnetic Materials.*, 2005, **288**,74-78.

[5] A. Francis and W. Daoush. *Journal of materials processing technology.*, 2007, **181**, 213-216.

[6] Y. Bai, J. Zhou, Z. Gui, L. Li and L. Qiao. *Journal of applied physics.*, 2007, **101**, 083907(1-6).

[7] N. A. Hill. *J. Phys. Chem. B.*, 2000, **104**, 6694-6709.

[8] L. E. Smart and E. A. Moore, *Solid state chemistry: an introduction*. CRC press, 2012.

[9] J. Hemberger, P. Lunkenheimer, R. Fichtl, S. Weber, V. Tsurkan, and A. Loidl. *Nature.*, 2006, **378**, 363-366.

[10] J. Kaur, R. Kotnala, and K. C. Verma. *Materials Letters.*, 2011, **65,** 3160- 3163.

[11] R. Schmidt, W. Eerenstein and P. A. Midgley. *Physical Review B.*, 2009, **79**, 214107(1-6).

[12] E. Montanari, L. Righi, G. Calestani, A. Migliori, E. Gilioli and F. Bolzoni. *Chem. Mater.*, 2005, **17**, 1765-1773.

[13] Z. H. Chi, C. J. Xiao, S. M. Feng, F. Y. Li and C. Q. Jin. *Journal of Applied Physics.*, 2005, **98**, 103519(1-5).

[14] K. Ueda, H. Tabata and T. Kawai. *Applied Physics Letters.*, 1999, **75**, 555-557.

[15] C. N. R. Rao and B. Raveau, *Transition metal oxides: structure, properties, and synthesis of ceramic oxides*, John Wiley & Sons, 1998.

[16] C. N. R. Rao and G. V. SubbaRao, *Transition metal oxides: crystal chemistry, phase transition, and related aspects*, U.S. Department of Commerce, 1974.

[17] A. Pandurang. *Transition Metal Oxide Thin Film based Chromogenics and Devices*, U.S. Department of Commerce, Elsevier, 2017.

[18] D. ADLER. *Radiation* Effects., 1970, **4**, 123-131.

[19] J. J. Gilman. *Electronic Basis of the Strength of Materials*, Cambridge University Press, 2003.

[20] S. Dogra, *Physical Chemistry Through Problems*, New Age International, 1984.

[21] D. W. Oxtoby., H. Pat Gillis., and A. Campion, *Principles of Modern Chemistry*, Cengage Learning, 2011.

[22] D. G. Pettifor. *Bonding and structure of molecules and solids*, Oxford: Clarendon Press; 1995.

[23] A. Chemistry. "Chemical bonding." https://alevelchemistry.co.uk/notes/chemical-bonding/ (accessed 2020).

[24] Britannica. "Covalent bonding." https://www.britannica.com/science/covalent-bond/ (accessed 2020).

[25] W. P. Anderson, J. K Burdett, and P. T. Czech. *J. Am. Chem. Soc*. 1994, **116**, 8808–8809.

[26] TECS. "Metallic Bond." https://www.tec-science.com/chemistry/chemical-bonds/metallic-bonding/ (accessed 2020).

[27] A. Munoz-Paez. *Journal of chemical education*, 1994, **71**, 381-388.

[28] S. E. Renfrew and B. D. McCloskey. *J. Am. Chem. Soc.* 2017, **139**, 17853−17860.

[29] Kapil Gupta, "Electronic, Magnetic and structural properties of transition metal oxides", PhD, Jadavpur University, Kolkata., 2012.

[30] E. Mete, "Electronic properties of transition metal oxides", PhD, The middle east technical university, Ankara., 2003.

[31] A. R. West, *Basic solid state chemistry*, John Wiley & Sons Incorporated, 1999.

[32] R. J. Cava.*Journal of Materials Chemistry,* 2001, **11**, 54-62.

[33] M. T. Weller, *Inorganic Materials Chemistry*, USA: Oxford University Press, 1995.

[34] P. W. Barnes, "Exploring structural changes and distortions in quaternary perovskites and defect pyrochlores using powder diffraction techniques", PhD, School of the Ohio State University., 2003.

[35] P. M. Woodward. *Acta Crystallographica Section B: Structural Science,* 1997,**53**,32-43.

[36] A. F. Wells, *Structural inorganic chemistry*. Oxford university press, 2012.

[37] L. G. Tejuca and J. L. Fierro, *Properties and applications of perovskite-type oxides*. CRC Press, 1992.

[38] G. Vasta, T. J. Jackson, and E. Tarte. *Thin Solid Films*. 2012, **520**,3071-3078.

[39] B. Ertuğ.*American Journal of Engineering Research (AJER),* 2013, **2**, 1-7.

[40] F. Jona and G. Shirane, *Ferroelectric Crystals* New York: Dover Publications, 1993.

[41] A. Wold and K. Dwight, *Solid state chemistry: synthesis, structure, and properties of selected oxides and sulfides*, Springer Science & Business Media, 2012.

[42] S. E. Dann, *Reactions and characterization of solids*, Royal Society of Chemistry, 2000.

[43] G. W. Rayner-Canham, G. Rayner-Canham, and T. Overton, *Descriptive inorganic chemistry*, Macmillan, 2003.

[44] S. Niitaka, M. Azuma, M. Takano, E. Nishibori, M. Takata, and M. Sakata.*Solid State Ionics*, 2004, **172**, 557-559.

[45] G. A. Prinz. *Science*, 1998, **282**, 1660-1663.

[46] G. A. Prinz. *Physics today*.1995, **48**, 58-63.

[47] A. Goldman, *Handbook of modern ferromagnetic materials*, Springer Science & Business Media, 2012.

[48] T. Moriya, *Spin fluctuations in itinerant electron magnetism*, Springer-Verlag, 1985.

[49] J. M. Herbert, *Ferroelectric Transducers and Sensors*, Gordon and Breach Science Publishers, 1982.

[50] P. Baettig, R. Seshadri, and N. A. Spaldin. *Journal of the American Chemical Society*, 2007, **129**, 9854-9855.

[51] H. Chiba, T. Atou, H. Faqir, M. Kikuch, Y. Syono, Y. Murakami, andD. Shindo. *Solid State Ionics*, 1998, **108**,193-199.

[52] P. Barber, S. Balasubramanian, Y. Anguchamy, S. Gong, A. Wibowo, H. Gao, H. J Ploehn, andH. C zurLoye. *Materials*. 2009,**2**, 1697-733.

[53] P. Baettig, R. Seshadri, and N. A. Spaldin. *Journal of the American Chemical Society*, 2007, **129**, 9854-9855.

[54] H. Chiba, T. Atou, H. Faqir, M. Kikuch., Y. Syono, Y., Murakami, andD. Shindo. *Solid State Ionics*, 1998, **108**,193-199.

[55] A. A. Belik, and E. Takayama-Muromachi. *Journal of Physics*, 2009, **165**, 012035(1)- 012035 (4).

[56] F. Sugawara, S. Iiida, Y. Syono, and S.-i. Akimoto. *Journal of the Physical Society of Japan,* 1968, **25**, 1553-1558.

[57] V. Bokov, M. IE, S. Kizhaev, M. Bryzhina, and G. NA. "Structure and magnetic properties of $BiMnO_3$," 1966, **7**, 2993-2994.

[58] H. Chiba, T. Atou, and Y. Syono.*Journal of Solid State Chemistry,* 1997, **132**, 139-143.

[59] H. Faqir *et al.Journal of solid state Chemistry,* 1999,**142**, 113-119.

[60] T. Atou, H. Chiba, K. Ohoyama, Y. Yamaguchi, and Y. Syono.*Journal of Solid State Chemistry,* 1999, **145**, 639-642.

[61] A. M. Dos Santos *et al. Physical Review B,* 2002,**66**, 064425(1-4).

[62] N. A. Hill and K. M. Rabe. *Physical Review B,* 1999, **59**, 8759-8797.

[63] R. Seshadri and N. A. Hill.*Chemistry of materials,* 2001,**13**, 2892-2899.

[64] T. Shishidou, N. Mikamo, Y. Uratani, F. Ishii, and T. Oguchi. *Journal of Physics: Condensed Matter,* 2004, **16**, S5677.

[65] X.H. Zhu, X.R. Chen, and B.G. Liu. *Solid State Communications,* 2016, **243**, 65-70.

[66] M. Azuma, K. Takata, T. Saito, S. Ishiwata, Y. Shimakawa, and M. Takano. *Journal of the American Chemical Society,* 2005, **127**, 8889-8892.

[67] S. Ishiwata *et al. Journal of Materials* Chemistry, 2002, **12**, 3733-3737.

[68] Q. Xu, H. Zai, D. Wu, Y. Tang, and M. Xu. *Journal of Alloys and Compounds,* 2009, **485**, 13-16.

[69] G. Smolenskiĭ and I. Chupis. *Soviet PhysicsUspekhi,* 1982,**25**, 475-493.

[70] F. Chen *et al. Applied physics letters,* 2006, **89**, 092910(1)- 092910(2).

[71] L. Wang *et al. Journal of alloys and compounds,* 2009, **469**, 1-3.

[72] V. R. Reddy, D. Kothari, A. Gupta, and S. Gupta. *Applied Physics Letters,* 2009, **94**, 082505(1-2).

[73] V. Khomchenko *et al. Applied Physics Letters,* 2008,**93**, 262905(1-3).

[74] M. Li, M. Ning, Y. Ma, Q. Wu, and C. Ong. *Journal of Physics D: Applied Physics,* 2007, **40**, 1603(1-5).

[75] V. Palkar and K. Prashanthi. *Applied Physics Letters,* 2008,**93**, 132906(1-3).

[76] Y.-H. Lin, Q. Jiang, Y. Wang, C.-W. Nan, L. Chen, and J. Yu. *Applied physics letters,* 2007, **90**, 172507(1-3).

[77] W. N. Su, D. H. Wang, Q. Q. Cao, Z. D. Han, J. Yin, J.R. Zhang, and Y.W. Du. *Appl. Phys. Lett*, 2007, **91**, 092905(1-3).

[78] A. A. Belik, M. Azuma, T. Saito, Y. Shimakawa, and M. Takano.*Chemistry of materials,* 2005,**17**, 269-273.

[79] P. Lacorre, J. Torrance, J. Pannetier, A. Nazzal, P. Wang, and T. Huang.*Journal of Solid State Chemistry,* 1991, **91**, 225-237.

[80] J. Torrance, P. Lacorre, A. Nazzal, E. Ansaldo, and C. Niedermayer.*Physical Review B,* 1992,**45**,8209.

[81] M. L. Medarde.*Journal of Physics: Condensed Matter,* 1997,**9**, 1679-1707.

[82] S.J. Kim, G. Demazeau, J. A. Alonso, and J.H. Choy.*Journal of Materials Chemistry,* 2001, **11**, 487-492.

[83] J.S. Zhou, J. Goodenough, B. Dabrowski, P. Klamut, and Z. Bukowski.*Physical review letters,* 2000,**84**, 526.

[84] J. A. Alonso, M. J. Martinez-Lope, M. T. Casais, M. A. Aranda, and M. T. Fernandez-Diaz. *Journal of the American Chemical Society,* 1999,**121**, 4754-4762.

[85] J. A. Alonso, M. J. Martínez-Lope, M. T. Casais, J. L. García-Muñoz, and M. T. Fernández-Díaz. *Phys. Rev. B,* 2000,**61**, 1756-1763.

[86] J. A. Alonso, M. J. Martínez-Lope, M. T. Casais, J. L. García-Muñoz, M. T. Fernández-Díaz, and M. G. Aranda. *Phys. Rev. B,* 2001,**64**, 094102.

[87] J. García-Muñoz, J. Rodriguez-Carvajal, P. Lacorre, and J. Torrance. *Phys. Rev. B,* 1992, **46**, 4414-4425.

[88] J. Rodríguez-Carvajal *et al. Phys. Rev. B,* 1998,**57**, 456-464.

[89] M. Zaghrioui, A. Bulou, P. Lacorre, and P. Laffez. *Phys. Rev. B,* 2001,**64**, 081102.

[90] K. Rajeev, N. Vasanthacharya, A. Raychauduri, P. Ganguly, and C. Rao. *PhysicaC:Superconductivity,* 1988, **153**, 1331-1332.

[91] H. Hughes *et al. Journal of the American Chemical Society,* 2005,**127**, 13790-13791.

[92] A. M. Dos Santos, S. Parashar, A. Raju, Y. Zhao, A. Cheetham, and C. Rao. *Solid State Communications,* 2002,**122**, 49-52.

2 Theoretical Aspects of Analytical Techniques

2.1 Introduction

Over the last century, there has been increasing interest in the study of crystallography, and the relationship between material structure and properties. In such studies, several analytical techniques were used to gather relevant data. Some techniques employed X-ray diffraction to find the complete structure and characterize crystalline materials. Electron diffraction was also used to find the distribution of atoms in solid materials. These techniques, in addition to spectroscopic methods, are of key importance in understanding the physical properties of materials, in addition to the study of crystalline and non-crystalline structures. Many experimental and characterization methods have been used in the research work described in this thesis.

This chapter considers the techniques used in this work. Each technique is explained in detail from the theoretical perspective, with a view to clarifying the relationships and equations that were useful to this work.

2.2 Crystal Symmetry

One of the conditions to be fulfilled in solid materials is the existence of an internal atomic arrangement. Not only is this internal arrangement regular, but it is also reflected in the materials outer shape. Furthermore, natural minerals solid existing in earth usually have consistent regular geometric forms called crystals. A crystal is defined as a homogeneous solid mass bounded by surfaces or faces called planes.[1-3] These surfaces are formed by natural factors under appropriate conditions of temperature and pressure. Physical and chemical

conditions are the decisive factor in the growth of crystals.[1-3] In contrast, nanocrystals are significantly small, and may only be seen under an electrons microscope. Under appropriate conditions, the crystal may form complete faces (Euhedral crystal) or none (Anhedral crystal) as shown in Figure (2.1).[1-3]

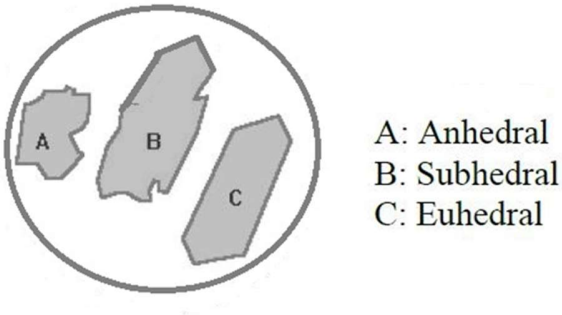

Figure 2.1: example of Crystal structure (Anhedral, Subhedral and Euhedral).

Crystalline structure is defined by the way that atoms are arranged in the crystal lattices, including forms, such as the three-dimensional Bravais lattices. The total number of Bravais lattice arrangements is fourteen, spread over seven crystal systems, as will be illustrated later. The smallest components of the crystal are called units cells. In fact, the unit cell that contains each lattice point can be repeated in three-dimensions to create the complete crystalline structure. The following four parts of the crystal are important in identifying crystalline structure:

1. Faces are defined as the outer surfaces that shape the crystal, both on the outside, and in its regular geometric shape. The faces of the crystal are usually plane, but in some metals, these are curved.
2. Edges are the border resulting from the confluence of two contiguous faces.
3. Solid angles arise from the correspondence of more than two faces.
4. Interfacial angles are formed by the confluence of two contiguous faces. The interfacial angle is estimated by the value of the restricted angle

between the two columns on both these sides or by the value of the complementary angle of the restricted angle between two contiguous faces.[1,3]

In fact, these parts of the crystal reflect the degree of regularity and consistency of the outer shape of the crystal. This is known as crystal symmetry and is the basis of study of crystals. The degree of symmetry may be identified in three elements:

1. **Plane of Symmetry:** the plane that divides the unit cell into two equal similar halves, meaning one being a mirror image of the other.
2. **Axis of Symmetry:** an imaginary straight line that passes through the centre of the unit cell. If the crystal is turned around on the axis of symmetry in a complete cycle without offsets, then it will return to the same position or repeat itself a number of times. The order of the symmetry axis is determined by the number of times that the crystal repeats its place. For example, if the crystal place is repeated twice, then the axis of rotation in this case is a two-fold axis symmetry 180°.
3. **Centre of Symmetry:** an imaginary point that mediates the crystal so that the linked line between each two sides, edges or opposite angles passes through the crystal centre.[4, 5]

The crystal axes are defined as imaginary axes intersecting at the center of the crystal, where the crystal face must intersect with one axis or more. In spite of the many and multiple forms of crystals, all these forms can be classified into seven systems, according to the unit cell. On the other hand, the unit cell in three dimensions is divided into four types as follows:

1. The primitive unit cell (P), which has a lattice point at each corner as shown in Figure (2.2).
2. The body-centred unit cell (I), which has a lattice point at each corner, and one at the centre of the cell as shown in Figure (2.2).

3. The face-centred unit (F), which has a lattice point at each corner and one in the centre of each face as shown in Figure (2.2).

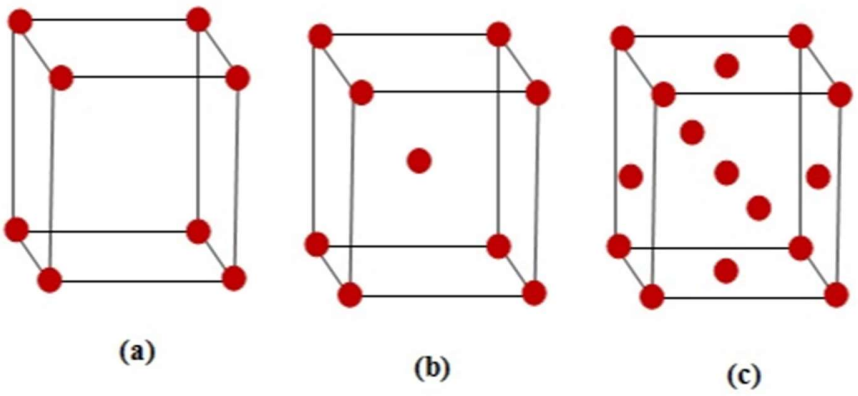

Figure 2.2: The unit cell. (a) primitive unit cell, (b) body-centered unit cell, (c) face-centered Unit.

The base-centered unit cell-symbol A, B, or C, which has a lattice point at each corner and one in the centers of one pair of opposite faces. Here, the unit cell depends on whether the opposing faces lie in the ab plane (C-centered), the ac plane (B-centered) or the bc plane (A-centered), as was illustrated in Figure (2.3).[6,7]

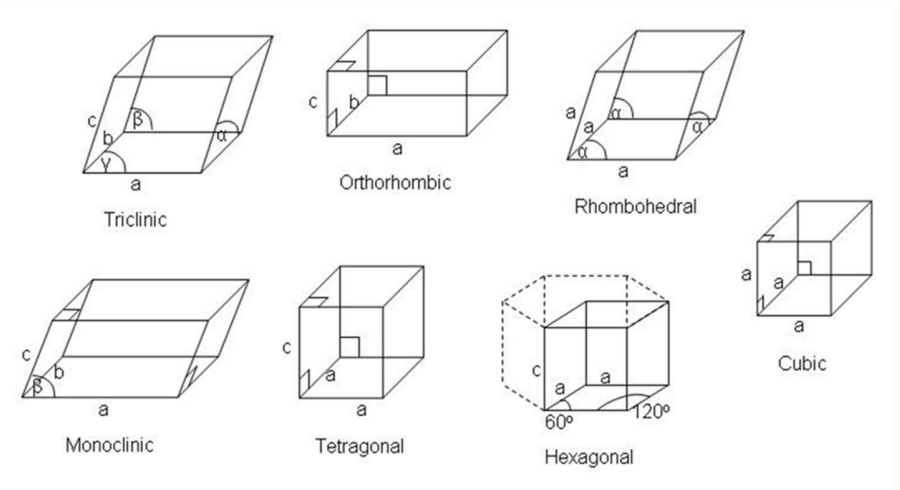

Figure 2.3: The seven crystal systems.

These unit cell shapes are determined by minimum symmetry requirements, which are also presented in Table (2.1).[6, 7]

Table 2.1: The seven crystal systems.[6]

CrystalSystem	Possible Bravais Lattice	Unit Cell Dimensions	Required Symmetry
Triclinic	(P)	$a \neq b \neq c$ $\alpha \neq \beta \neq \gamma$	None
Monoclinic	(P) (C)	$a \neq b \neq c$ $\beta \neq \alpha = \gamma = 90°$	One twofold axis or one symmetry plane
Orthorhombic	(P) (C) (I) (F)	$a \neq b \neq c$ $\alpha = \beta = \gamma = 90°$	Any combination of three mutually perpendicular twofold axes or planes of symmetry
Trigonal/Rhombohedral	(P)	$a = b = c$ $\alpha = \beta = \gamma \neq 90°$	One threefold axis
Hexagonal	(P)	$a = b \neq c$ $\alpha = \beta = 90°, \gamma = 120°$	One sixfold axis or one sixfold improper axis
Tetragonal	(P) (I)	$a = b \neq c$ $\alpha = \beta = \gamma = 90°$	One fourfold axis or one fourfold improper axis
Cubic	(P) (I) (F)	$a = b = c$ $\alpha = \beta = \gamma = 90°$	Four threefold axes

2.3 X-ray Diffraction

2.3.1 Characteristics and Uses of X-rays

X-rays are part of the invisible electromagnetic, where the X-ray site is between gamma rays that have high energy and ultraviolet rays that have low energy, as shown in Figure (2.4). Electromagnetic radiation such as visible light, radio

waves, gamma rays, and X-rays can be distinguished in terms of energy, wavelength, and frequency.[8]

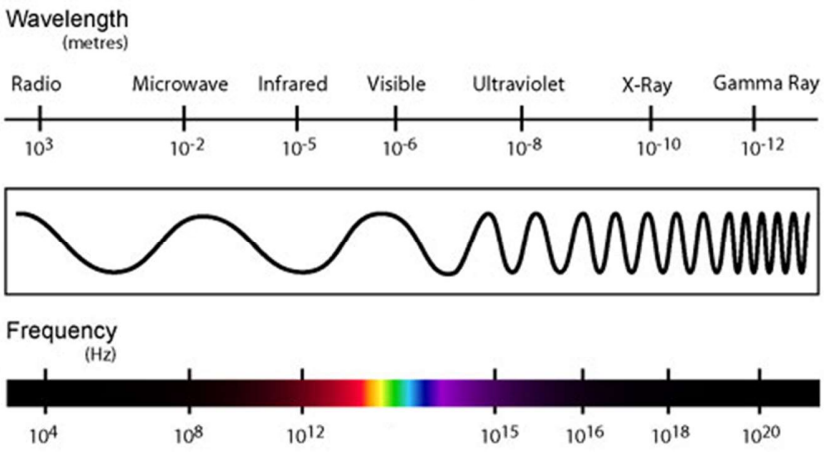

Figure 2.4: The Electromagnetic spectrum.

All these quantities are related to each other by the following equations:

$$\Delta E = \hbar \upsilon \qquad (2.1)$$

where ΔE is the energy difference (photo energy), υ is the frequency of the emitted radiation and $\hbar$ is Planck's constant (6.626×10^{-34} m^2kg/s). The frequency can be calculated from the following equation:

$$\upsilon = \frac{c}{\lambda} \qquad (2.2)$$

where c is the speed of light and λ is the wavelength.[9,10]

X-rays were discovered in 1895 by Wilhelm Rontgen, and this discovery has had a significant impact on human life in various medical, industrial, and scientific aspects. X-rays have very high energies and short wavelengths compared to the electromagnetic spectra except gamma-ray. X-ray wavelengths range between 0.1 to 100 Å, which gives them the ability to penetrate objects on an atom scale, and their energies are ranging between 102 to 105 eV. Therefore, X-rays use in crystalline characterization experiments such as phase identification, structure

determination, and analyzing the arrangement of atoms in many kinds of materials. The atoms of crystals organize in lattice planes, which are separated from each other by regular distances, where X-rays interact with the atoms in a crystal. One of the most critical properties of X-rays is that they flow in a straight line and at speed equal to the speed of light. Moreover, the X-rays are not affected by the presence of a magnetic or electric field, which indicates that the X- rays do not carry any electrical charge.[9, 11] The atoms of crystals are organized in planes, which are separated from each other by regular distances. These reflect X-rays like small mirrors when a beam falls on the crystal. The planes diffract the rays in a systematic pattern, where each crystal type has a different pattern of diffraction. The arrangement of atoms in a crystal can be determined by studying the different types of diffraction. X-rays are also used in the analysis of many complex chemicals, such as enzymes, proteins, and DNA.[9, 11, 12]

2.3.2 Generation of X-rays

The X-ray generating apparatus consists primarily of a ray-generating tube; historically, it was known as the Coolidge tube, as shown in Figure (2.5). This tube is a glass tube with a closed hole with a thin layer of beryllium that allows X-ray emission, and this tube contains an electrode, which is cathode and anode.

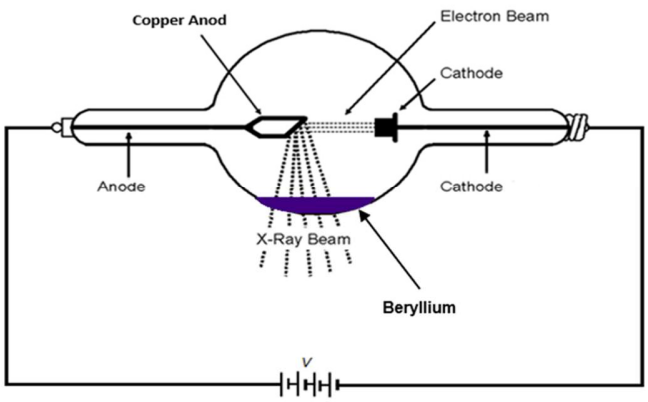

Figure 2.5: X-rays tube.

X-rays are generated in the laboratory by bombarding a metal with high energy electrons, which occurs when the electric current passes during the cathode. The cathode is composed of material rich in electrons, *e.g*. tungsten, which allows the emission of electrons from its surface. The anode is a metal disc (usually molybdenum or copper), which is positively charged and attracts liberated electrons from the cathode. In addition, a high voltage is applied between the cathode and the anode up to 200 kV to accelerate electrons rapidly in the direction of the anode. Electrons emitted from the cathode impinge on the electrons of the anode material, which are located in the core orbitals close to the nucleus; when the energy of electrons is high, the core electron ionises away from the target atom, leaving a vacancy. An electron in a higher orbit drops into the hole created by the departure of the electron, which then releases the difference of energy between the two levels in the form of electromagnetic radiation. Therefore, the emergent photon is the photon of X-rays because the difference in the two energy levels is significant.[1, 9] X-ray photons can also be obtained without the collision of the free electrons with atoms.

In general, the X-ray photon-generating effect is known as a braking action phenomenon, termed the Bremsstrahlung effect. Figure (2.6) shows a spectrum of peaks for the output from an X-ray tube, with sharp peaks characteristic of the electron transfers between discrete orbitals superimposed upon the broad Bremsstralung background.[9, 12]

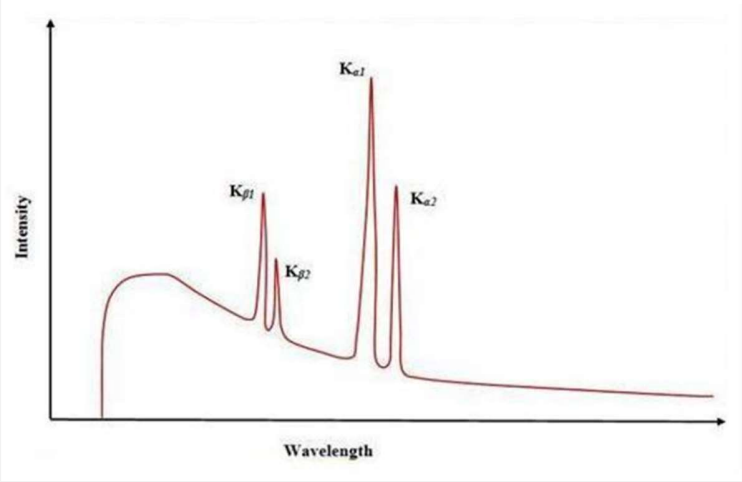

Figure 2.6: Schematic X-ray spectra obtained when an accelerated electron beam is incident to a metal target.

When X-rays penetrate the material with enough frequency or energy, an excitation will occur of the electrons in the inner shell of the atom. These excited electrons will move to the empty outer shells or will lose it, which allows ionization of the atom. In the event of the excited electrons returning to their stable state, they will lose energy, which comes out in the form of the emitted radiation, or this energy will remove the less bound electrons from the atom. The radiation emitted depends on the atomic shells that called in order (K, L, M, N, ..., *etc.*) that correspond with energy levels (n=1, 2, 3, ..., *etc*.), where to distinguish the transmission of electrons from high shell to low shell by symbols ($\alpha,\ \beta,\ \gamma,$ ..., *etc.*). For example, when a relaxed electron at the ground state in L shell moves to K shell will produce radiation usually named as Kα_1. While if the electron moves from M shell to K shell, the produced radiation is called K$_{\beta 1}$. whilst when a relaxed electron at the ground state in M shell moves to L shell will produce radiation usually named kα_2, if this electron moves from N shell to L shell, the produced radiation is called k$_{\beta 2}$. As is clear from Figure (2.6), the wavelengths kα are longer than k$_\beta$, while k$_\beta$ are more energetic than kα and less intensity, the reason for that is the reduced probability of transmission of electrons.[13]

In an X-ray experiment, a single wavelength output of X-rays is required. The wavelength must be selected, and the unwanted X-rays at other wavelengths can be removed by an easy filtering process. The K$_\beta$ lines are removed using a thin foil of the element one atomic number less than the target metal, *e.g*. a Ni (Z=28) foil is used to filter out the K$_\beta$ lines from a Cu target (Z=29). A single crystal monochromator is used to obtain a single wavelength from the remaining Kα lines, essentially in a direct application of Braggs Law in Section (2.3.3).[1,9,12]

2.3.3 Scattering from Crystalline Solids and the Bragg Equation

X-ray diffraction happens when a beam of X-rays interacts with a material. X-ray diffraction can be characterised using the Bragg method developed by W. L. Bragg.[14,15] The Bragg method clarified that X-ray beams fall on the material in straight lines. However, as a result of the interaction of X-rays with the electrons of the material, these rays become scattered in all directions. Constructive interference can occur between the X-rays scattered only in the case that scattering centers are separated by distances approximately equal to the wavelength of the X-rays, as is shown in Figure (2.7).

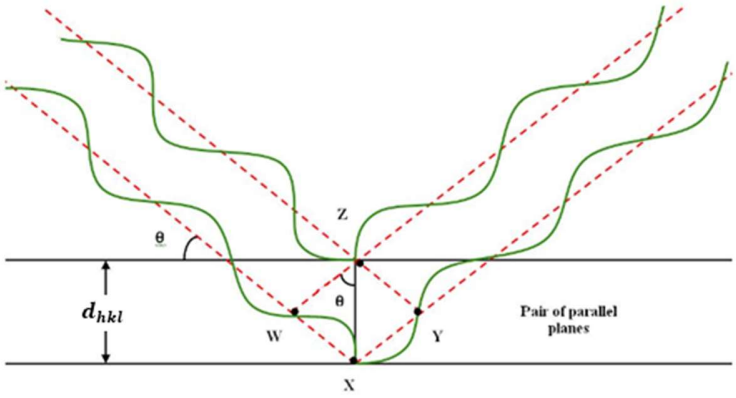

Figure 2.7: Scattering of X-rays from a parallel set of planes.

Figure (2.7) shows that the scattered X-ray beams from points X and Z can produce diffracted beams in phase. This occurs only when the additional distance travelled by the X-ray photon from W to X and X to Y is an integral number of wavelengths. This is dependent on both the lattice spacing d_{hkl} and the angle of incidence of the X-ray beam, θ.

$$\text{path difference} = WX + XY$$

Using trigonometry, the length of WX and XY can be expressed as:

$$WX + XY = 2\,d_{hkl} \sin\theta$$

since WX = XY are equal, and their sum must equal an integral number of wavelengths. Path length can then be expressed as:

$$d_{hkl} hkl \sin\theta + d_{hkl} \sin\theta = n\lambda$$

$$2\,d_{hkl} \sin\theta = n\lambda \qquad (2.3)$$

Equation (2.3) is known as the Bragg equation, where n is an integer and λ is the X-ray wavelength. In general n is always taken as unity.[12] The symbols h, k and l are known Miller indices.

2.3.4 Miller indices and Lattice Plares

Miller indices are used to describe directions and symmetric planes of atoms in a crystal. The Miller indices may take positive or negative integer values or zero. The Miller indices are defined as indicators of the usual three directions (x, y, z), and are perpendicular to each other, where h refers to the intersection of the plane on a; k refers to the intersection of the plane on b; and l refers to the intersection of the plane on c, as was illustrated in Figure (2.8).

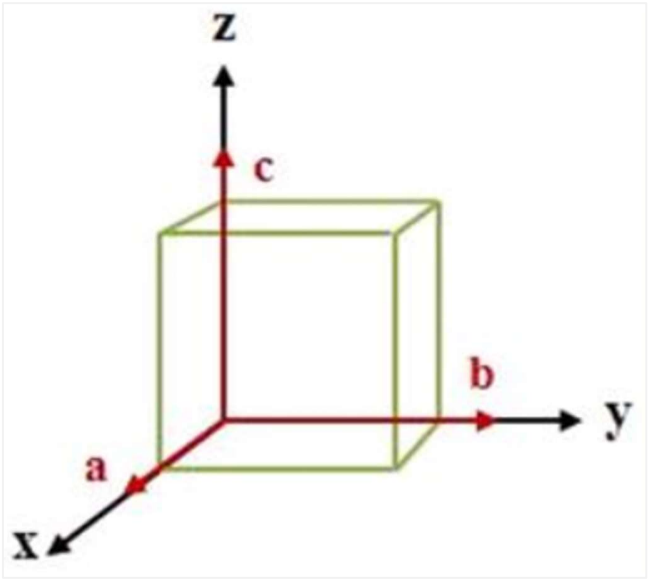

Figure 2.8: A cubic unit cell with dimensions $a \times b \times c$.

The orientation of a crystal face or a plane of atoms within a crystal lattice is determined and described through a series of steps. This can lead to notation of this orientation or plane using Miller indices.

1. First, identify the intercepts that the plane makes with the crystallographic x, y and z axes. For example, the point $(a, 0, 0)$, where a is the planeintersecting with the x axis, but not the y or z axes. In other words, the surface is parallel to the y and z-axes, but it may be assumed that it intersects with the y- and z- axes at infinity, thus the intercepts are (a, ∞, ∞).

2. Second, conversion of the coordinates (x, y, z) to fractional coordinates bydividing the coordinates by the intersections of the plane (a, b, c); thesewillbe in the following form$\left(\frac{x}{a}, \frac{y}{b}, \frac{z}{c}\right)$. In the case of a cubic unit cell as hasshown in the previous example, the coordinate (x, y, z) will be divided by$a$, which is the cubic cell constant; thus, the fractional intercepts are:

$$\left(\frac{x}{a}, \frac{y}{a}, \frac{z}{a}\right) \rightarrow \left(\frac{a}{a}, \frac{\infty}{a}, \frac{\infty}{a}\right) \rightarrow (1, \infty, \infty)$$

3. The final step generates the Miller indices by taking the inverse of the fractional intercepts. By applying this step to the previous example, the Miller indices are as follows:

$$\left(\frac{1}{1}, \frac{1}{\infty}, \frac{1}{\infty}\right) \rightarrow (1, 0, 0)$$

The plane with Miller indices (100), (110) and (111) was illustrated in Figure (2.9).[16]

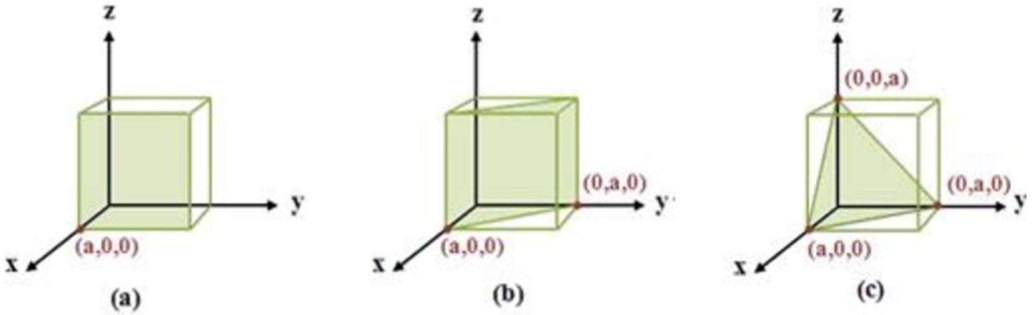

Figure 2.9: The plane with Miller indices (**a**) is the (100) surface, (**b**) is the (110) surface and (**c**) is the (111) surface.

When equation (2.3) is satisfied at a particular angle for a particular set of h, k and l values, the X-rays will constructively interfere, and X-rays will be recorded at the detector. Where the equation is not satisfied, *i.e.*, at another value of θ (since λ is fixed), the waves will destructively interfere, and X-ray intensity will not be recorded at the detector. As such, with a fixed value of λ, a sweep of the angular range will allow the values for which the Bragg equation is satisfied to be determined and the values of h, k and l to be determined for each peak, along with the lattice parameters of the unit cell.

There are an infinite number of lattice planes with various Miller indices, which exist in a crystalline material. Also, all planes will have a particular separation, d_{hkl}. Therefore, there will be a diffraction maximum at a particular angle θ, for any set of planes. In principle, through the Bragg equation, relationships between the diffraction angle and the lattice parameters can be obtained. For example, in the cubic system (where a is the lattice parameter):

$$\frac{1}{\mathrm{d}^2} = \frac{h^2 + k^2 + l^2}{a^2} \qquad (2.4)$$

and the Bragg equation

$$2\,\mathrm{d}_{hkl}\sin\theta = \mathrm{n}\lambda$$

where $n = 1$ and rearranging for d gives

$$\frac{1}{d} = \frac{2 \sin \theta}{\lambda}$$

squaring parties, leads to

$$\frac{1}{d^2} = \frac{4 \sin^2 \theta}{\lambda^2}$$

by compensation in equation (2.4), we get

$$\frac{4 \sin^2 \theta}{\lambda^2} = \frac{h^2 + k^2 + l^2}{a^2}$$

$$\sin^2 \theta = \frac{\lambda^2}{4a^2}(h^2 + k^2 + l^2) \qquad (2.5)$$

Structural information about the crystals under study can be obtained using equation (2.5) by simple comparison of the relative values of $\sin^2\theta$. It is more complex when the system is not cubic. These equations become more complex in other crystal classes where $a \neq b \neq c$ and the angles α, β and γ derivate from $90°$. In this case, computer-based algorithms, such as ITO (Infiiltration Tactics Optimization) or TREOR (Trial and error- based method), are used to index the observed X-ray powders pattern. ITO is a deductive search program employing zone-indexing in the index space. It performs best when given 30 to 40 accurately measured powder lines. It is optimized for low symmetry systems (orthorhombic downwards). Indeed, high-symmetry lattices may be reported wrongly in an orthorhombic setting.[17] On the other hand, TREOR is a semi-exhaustive, heuristic search method in the index space; it requires about 25 accurately measured powder lines. It is effective for searches down to triclinic symmetry.[18]

2.3.5 Powder X-ray Diffraction

The powder X-ray diffraction method is one of the most important techniques used in solid-state chemistry. There are numerous applications of X-ray powder

diffraction, such as structure determination and particle size measurements. Moreover, powder X-ray diffraction is used in single crystal experiments, which are very useful in the qualitative analysis phase. Each material has a crystalline powder pattern distinct from others.[1] The X-rays used in this method have a single energy, and one wavelength. The X-ray is directed at a crystalline material after crushing it to a fine powder and placing it in a capillary tube or into a recess in a plate. The reflected X-rays are recorded as a function of 2θ. In the infancy of powder diffraction, the diffracted X-rays would have been recorded using photographic film. The purpose of crushing of the materials is to is to more evenly distribute the small crystals randomly in all directions. The angle between the surface and beam is θ, where θ is a reflector of beams in the direction, which creates a constructive interference, and follows Bragg's law. The reflected X-rays disperse from the granules powder in the concentric conical form as shown In in Figure (2.10). surrounding the center of the incident beam. The cone angle can be measured, where equal to (2θ). Since the wavelength can be designated, it is possible to find the distance between lattice plares and study the crystal structure of the material. This is an appropriate method to use when it is not possible to obtain a single crystal.[16]

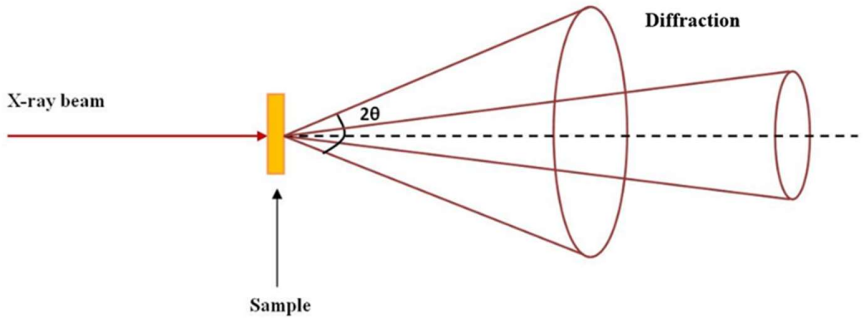

Figure 2.10: Diffraction cones obtained from a polycrystalline sample.

The method of powder X-ray diffraction is a non-destructive technique and requires only a small sample amount. This method is also able to distinguish

between the different crystalline polymorphs of the same compound. Identifying powder X-ray diffraction patterns depends on two main factors, namely:

- The size and shape of the unit cell.
- The atomic number and position of the multiple atoms in the cell. Thus, two materials that may have the same crystal structure, but different compositions will give rise to quite distinct powder patterns. The resulting powder patterns have two characteristic features:
- The d-spacings of the lines.
- The relative intensities of the lines, where intensity is a function of scattering angles.

The quantitative measurement of intensities is much more difficult than measuring the d-spacings. Mostly, this measurement often varies from one sample to another. On the other hand, the d-spacings have to be reproducible from one sample to another, except when impurities are present to form a solid solution, or the material is in some stressed, disordered or metastable condition. Thus, the d-spacing is far more useful and capable of precise measurement.[1]

2.4 Rietveld Analysis

Rietveld method is for analysing the powder diffraction data in which the crystal structure is refined by profile fitting of diffraction pattern to a calculated profile. The pattern analysed is containing many overlapping Bragg peaks without the intermediate steps of extracting structure factors.[19] The 'Rietveld method' or 'Rietveld refinement' was named after Dr Rietveld, who first calculated analytical procedures to provide detailed crystal structural information from the powder diffraction pattern.[20] The first application of this method was in 1969 for neutron powder methods (Rietveld, 1969),[21] especially for refining nuclear and magnetic structures, but then it was modified and used for X-ray powder diagrams and for various analysis like structural analysis which includes occupancies, lattice parameters, and atomic position, quantitative phase (grain sizes and micro-

strain), temperature vibrations (isotropic and anisotropic) and stacking fault and twining.[22]

In structural analysis, two main steps are involved which structure solving and model are refining. In single crystals, the reliable procedure requires the estimation of structure factors moduli which are derived from the diffraction experiments and related with the reflections. This condition can easily be accomplished in case of single crystal and the analysis can be carried out easily. The experimental moduli, in general, are proficiently be used as observations in the nonlinear least-squares calculations for structural parameters refining.[22]

In powder refinement, the results are not satisfactory because the information of three-dimensional reciprocal lattices is compressed to one-dimensional information and resulted in lower reliability of moduli estimates. In this way, the experimental structure factor moduli as observations in the least squares minimization for refining structural parameters have low accuracy and can be unsuccessful.[19] In short, least squares method is used as statistical tool frequently for comparing the specific certainty value obtained from model or solution with the experimentally obtained data. In other words, least squares method of statistical analysis provides numerical confirmation of agreement of structural model with the experimental diffraction data.[22] Wherefore, the least squares method is relied on an assumption of having high ratio ofexperimental observation for defined parameters and also the experimental errors in data having Gaussian or normal distributions (bell-shaped curve). The structural model is refined by least-squares minimization of the residual.[19]

$$S_y = \sum_{i=1}^{N} w_i[y_i(obs) - y_i(calc)]^2 \qquad (2.6)$$

Where, $y_i(obs)$ is observed intensity at the ith point in diffraction pattern corrected at b_i (background intensity) w_i is the statistical weight assigned to each point, $y_i(calc)$ is calculated intensity the ith point. If at each point, background assumed

to be zero and the only error source in intensity measurement is from counting statics then the weight would be:

$$w_i = [y_i(obs)]^{-1} \qquad (2.7)$$

2.4.1 Criteria of Fit

The Rietveld refinement process requires refinable parameters until a 'best fit' where the residual S_y is minimised in equation (2.6). Several criteria, such as the adequacy of the model and whether a global minimum is reached, are required to obtain a 'best fit'. In order to make good judgements on refinement, indicators to monitor the proceedings satisfactorily to completion before it can be stopped must be available. Using the Rietveld method, several R-values are now commonly used. These are 'R-Bragg' and 'R-structure factor', which are based on a deduced model and not on actual observed Bragg intensities. However, 'R-weighted pattern' is the most meaningful of these R's, and are comparably quoted in the literature on single-crystal structure refinements, as they serve a proper function, are insensitive to misfits, and do not involve the Bragg intensities of the phases being modelled.[20]

Therefore, in the least square method, there are two types of parameters used: structural parameters and profile parameters. The first contains the fractional coordinates of each atom within the asymmetric unit, along with its isotropic or anisotropic displacement. It is not feasible to refine a single crystal based purely on profile parameters, which include the half-width parameters and the unit cell dimensions. Additional parameters can be added to both groups to model the background and the asymmetry of reflections. The maximum number of parameters added in Rietveld evaluation is appreciably characterised by the diffraction pattern quality; however, intrinsic line bordering set a higher limit to this amount.[19] The following equation can give the estimate of Bragg R factor

agreement with the model during refinement I_k denotes integrated intensity of kth reflection:[19]

$$R_I = \frac{\sum_k [I_k(obs.) - I_k(calc.)]}{\sum_k I_k(obs.)} \qquad (2.8)$$

A residual index, which known as the R-value or profile R-factor, is used to monitor the refinement process in the least squares approach. The profile R Factor, R_p, is defined mathematically as:[13, 19, 23]

$$R_p = \frac{\sum_i [y_i(obs) - y_i(calc)]}{\sum_i y_i(obs)} \qquad (2.9)$$

Similarly, R_{wp} gives a measurement value similar to R_p for the difference between the observed and calculated values. However, R_p does not consider the peak height and the standard deviation of the background radiation, which makes R_{wp} a more helpful metric for measuring the similarity of two data sets. R_{wp} can be calculated using the following formula:[23, 24]

$$R_{wP} = \sqrt{\frac{\sum_i w_i [y_i(obs) - y_i(calc)]}{\sum_i w_i y_i^2(obs)}} \qquad (2.10)$$

Preferably, the R_{wp} value should ideally be close to the predicted R value, which is a measure of the experimental data's quality. The following equation gives the predicted R value R_E, where an independent observation is denoted by N, while a refined parameter is denoted by P:[19]

$$R_E = \sqrt{\frac{N - P}{\sum_i w_i y_i^2(obs.)}} \qquad (2.11)$$

A successful refinement depends on the best quality-of-fit ratio of R_{wp}, R_E, these values are used to calculate χ^2, and it should reach unity in a successful refinement. Mathematically, χ^2 is calculated via the following equation:[24, 25]

$$\chi^2 = \left(\frac{R_{wp}}{R_E}\right)^2 \qquad (2.12)$$

All of these parameters are variables that are refined by least squares. Since each of these parameters is dependent on numerous variables, the minimization process can sometimes fall into false minima or diverge. This risk can be reduced and even avoided if the diffraction pattern obtained during experiments is of sufficiently high quality,[22] suitable functions for defining peak and background and mainly the structure model with physical and chemical sense. The better results of the Rietveld method are possible by adjusting the structure model as close as possible to the true one.[13, 22]

Using the Rietveld method, several R-values are now commonly used. Figure (2.11) shows the graph of refinement process, in which the R-value changes with the change in parameters during the refinement.[13]

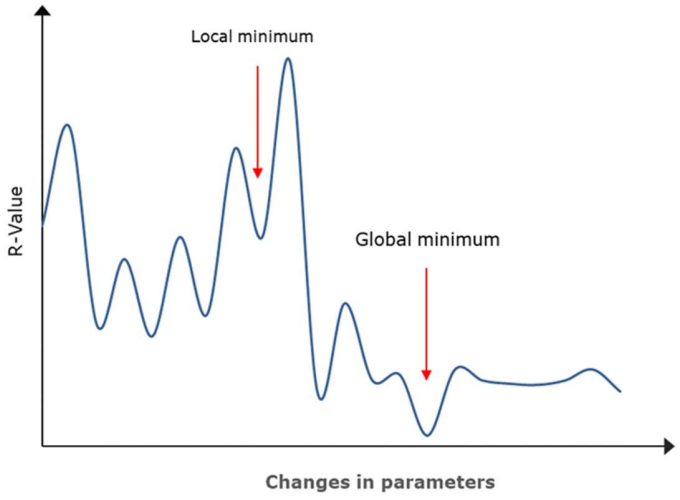

Figure 2.11: Minima in the least square's refinement.

The Rietveld refinement process requires refined parameters until a 'best fit' where the residual S_y, in equation (2.6) is minimised. Several criteria such as

adequacy of model, and whether a global minimum is reached, are required to obtain 'best fit'. In order to make good judgments on refinement, indicators to monitor the proceedings satisfactorily to completion before it can be stopped, must be available. In case of non-accurate structure, the refinement can trap the model in a local energy minimum, which in turn not the true structure. These conditions can be minimised by ensuring the model to be close to the true structure by monitoring R-value and the various shifts in the atomic parameters (fractional coordinates) and displacement parameters of the structure.[13]

In the Topas academic program, computational models are used to alter unit cell and instrumental parameters in order to create the best theoretical fit between the calculated and observed data sets.

2.5 Dielectric Materials

Dielectric can be defined as the medium that cannot fully monitor a static, external, macroscopic electric field from its interior because of the physical constraint on charge rearrangements. The dielectric materials are those non-conductive materials that become polarised under the application of electric field.[26] In addition, dielectric materials are often characterised by the fact that there are no free electrons, and separation of electrons in orbits around atoms of those materials is difficult, except in particular situations. Moreover, these materials are able to endure high voltages without suffering degradation and becoming electrical conducting. Examples of such materials include air, glass, plastic, rubber, and cotton, which are typically used to separate or isolate electrical conductors and prevent the transmission of electrons, or electricity, of the connector to any other body. Dielectric materials are used principally in capacitors to increase the ability of capacitors to store electric charge. Most capacitors include dielectric materials between their panes. The dielectric material in electrolytic capacitors is usually a dielectric oxide; for example, $BiFeO_3$ and $BiMnO_3$ perovskites.[1] The voltage applied across an insulator restricts

electron or ion movement, leading to the polarization of charge. After the voltage is removed, this polarization disappears. However, there are dielectric materials, which maintain a polarised state after removing the electric field. These are called ferroelectric materials such as $Bi_{4-x}La_xTi_3O_{12}$.[27] The polarisation phenomenon alters the electromotive force of materials. Since the polarisation and voltage relationship is linear, increased polarization results in a lower electric potential; this results in a significant change in voltage.[28] The charges behaviour of the material is in a parallel plate capacitor, which can be used as dielectric properties. To explain this, consider an idealized parallel plate capacitor, with A plate area and d gap between the plates as illustrated in Figure (2.12).

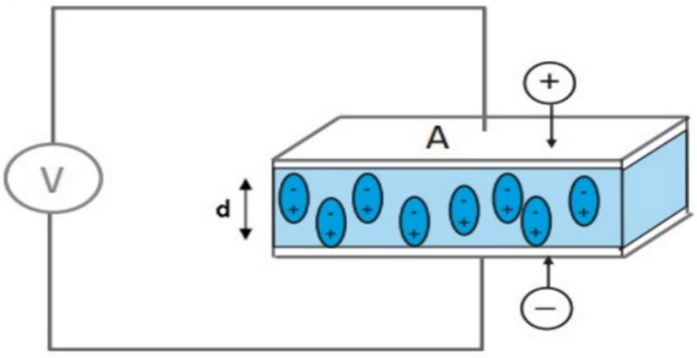

Figure 2.12: Ideal parallel-plate capacitor circuit filled with conductivity (σ) and dielectric constant (ε′) material.[29]

Initially, consider the area between the plates as a vacuum, where the d distance between these pairs of parallel plates is small compared with the linear dimensions of these plates. A constant voltage difference V between the plates will induce a charge density D or σ will be induced by a constant potential difference of (V) between the plates as:

$$D = \varepsilon_0 \frac{V}{d} \qquad (2.13)$$

The proportionality between the charge Q and potential is known as the capacitance between the plates C and is given by:

$$C = \frac{Q}{V} \qquad (2.14)$$

According to Gauss's law, the electric field E between the capacitor plates is described by the relationship:

$$E = \frac{\sigma}{\varepsilon_0} \Rightarrow \sigma = \varepsilon_0 E \qquad (2.15)$$

Further, the charge and the potential difference or voltage between the plates are defined by following equations:

$$V = Ed \qquad (2.16)$$

$$Q = \sigma A \qquad (2.17)$$

Therefore, the capacitance C_0 is the total charge induced on the plates divided by the voltage applied and is given by:

$$C_0 = \frac{\varepsilon_0 A}{d} \qquad (2.18)$$

where, ε_0 is the permittivity of free space, which equals (8.85 x 10^{-12}F/m), and A is the plate area. There is small additional amount of capacitance in a real circuit from the wandering fields in air outside of the material.
Now, if a material is added between the plates, it will induce an additional charge density P_0 on the plates from the charged polarization in the material. The charge density is proportional to electrical field (E) for sufficiently low voltages and can be given as:

$$D = \varepsilon_0 E + P_0 = \varepsilon_1 \varepsilon_0 E \qquad (2.19)$$

And the capacitance is given as:

$$C = \frac{\varepsilon_1 \varepsilon_0 A}{d} \qquad (2.20)$$

Where, ε_0 (or sometimes ε_V) is material static permittivity.

The quantity of charge, Q_0 is stored in the plates, can be found from:

$$\mathrm{Q}_0 = \mathrm{C}_0\mathrm{V} \qquad (2.21)$$

The charge stored amount of Q_0 is increased to Q_1. Therefore, the quantity of capacitance increases to C_1, which occurs when the insulating material is placed between the plates, and the same potential difference applied. The relative permittivity or dielectric constant (ε') can be calculated using the following equation:

$$\varepsilon' = \frac{\mathrm{C}_1}{\mathrm{C}_0} \qquad (2.22)$$

Where, C_0 is the capacitance of vacuum and C_1 is the capacitance in dielectric medium. The dielectric constant is always greater than one, where $\mathrm{C}_1 > \mathrm{C}_0$. Furthermore, its value is not fixed at all, and changes depending on conditions of use such as the temperature. For example, the dielectric constant for ferroelectric materials such as $BaTiO_3$ is in the range 10^3 to 10^4. For air, $\varepsilon'' \simeq 1$, while for most ionic solids, $\varepsilon'' = 5$ to 10.

The Conductance (G) might also be induced in the circuit in parallel with the capacitance as:

$$\mathrm{G} = \frac{\sigma_0 \mathrm{A}}{\mathrm{d}} \qquad (2.23)$$

Where, σ_0 is material static conductivity. The electrical properties of circuit of the figure (2.12) can be written for sinusoidally oscillating fields in many ways.

At angular frequency ω the complex admittance Y which is measurement of how easily current flow from circuit, and it is reciprocal of impedance, will be as:

$$Y^* = G + j\omega C = \frac{A}{d}(\sigma + j\omega\varepsilon_0\varepsilon) \qquad (2.24)$$

The complex conductivity σ^* the material will be as:

$$\sigma^* = \sigma + j\omega\varepsilon_0\varepsilon \qquad (2.25)$$

The complex capacitance C^* will be as:

$$C^* = \frac{Y^*}{j\omega} \qquad (2.26)$$

And that can define the complex relative permittivity ε^*.

$$\varepsilon^* = \varepsilon' - j\varepsilon'' = \varepsilon' - j\frac{\sigma}{\omega\varepsilon_0} \qquad (2.27)$$

Permittivity and complex conductivity are related as:

$$\sigma^* = j\omega\varepsilon^*\varepsilon_0 \qquad (2.28)$$

And then, the series equivalent impedance Z^* (the reciprocal of admittance) will be given as:

$$Z^* = \frac{1}{Y^*} = R + jX = \frac{G - j\omega C}{G^2 - (\omega C)^2} \qquad (2.29)$$

By which the complex specific impedance of the material Z^* will be defined as:

$$Z_1^* = = \frac{1}{\sigma^*} = \frac{\sigma - j\omega\varepsilon_0\varepsilon}{\sigma^2 - (\omega\varepsilon_0\varepsilon)^2} \qquad (2.30)$$

By considering only the dielectric reaction of the electrical charge density in the small, static, and linear limit, the dielectric will obey the constitutive equation (2.18):

$$E = \frac{D}{\varepsilon(\omega)} = \frac{D - 4\pi P}{\varepsilon_0} \qquad (2.31)$$

Where, $\varepsilon(\omega)$ is dielectric permittivity and $D = \varepsilon_0 E_0$ is an auxiliary vector. The dielectric permittivity is a complex function of frequency of applied

electrical filed (ω) which measures the linear dielectric reaction of a material in the constant field as shown in Figure (2.13).

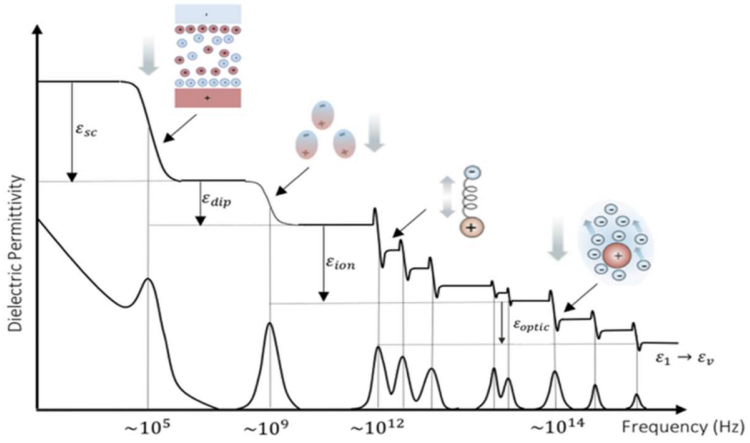

Figure 2.13: Frequency dependent dielectric spectrum of perovskites.[30]

In complex materials, like perovskites, multiple dielectric mechanisms are present. With the same assumptions, the contributions from this dielectric permittivity mechanism are added in this way:

$$\varepsilon_r = \varepsilon_{optic} + \varepsilon_{ion} + \varepsilon_{dip} + \varepsilon_{sc} \qquad (2.32)$$

Where, $\varepsilon_r = \varepsilon/\varepsilon_0$ is the relative permittivity. The ε_{optic} is the response of electrical density. The ε_{ionic} is the reaction of lattice vibrations and related to the chemical bond polarity and softness of vibrations. The ε_{dip} is because of the slower realignment of dipole species. The ε_{sc} is the charge distribution from free charges redistributing over macroscopic distance in materials.[30]

The high value of dielectric constant (ε) such as in perovskite $BaTiO_3$ helps in the generation of larger electrostatic forces which are accountable for

the actuation stress and strain, whereas the material strength denotes the elastic ability to survive the electrostatic forces generated. The atomic movement changes the phase from the cubic to the tetragonal and leads to the development of the dipole moments along the [100] direction. The crystal structure transformation and the high polarization due to dipole moment is the reason of high dielectric constant in $BaTiO_3$.[31]

2.6 Electronic Spectroscopy

2.6.1 Introduction

Visible light exhibits the behaviour of ultraviolet light in several of its manifestations, where both result from absorbed of electronic excitation in the molecules. In addition, most instruments that use the methods of spectral analysis in the field of visible radiation are the same as that used in the methods of spectral analysis in the field of ultraviolet radiation. Therefore, have been the practice to their study together.[32] UV and visible spectroscopy studies, which depend on absorption of ultraviolet or visible, lead to the exciting electrons in the molecule that absorbs the rays enabling us to determine the electronic behavior in the outrushes of the complexes.

2.6.2 Electronic Excitation

As is known, the molecules consist of atoms, each of which consists of a nucleus and electrons orbiting around it in the levels of specific energy. The electrons would move from the ground state to the excited state if the molecules absorbed specific energy. This transition is called electronic excitation. For a beam of light

to create an electronic excitation, this beam should be in the visible radiation field or ultraviolet. Furthermore, the frequency of the absorptive beam is associated with energy by the following relationship:

$$\mathrm{E} = h\upsilon \qquad (2.33)$$

where E is the energy of a photon, h is Planck's constant and υ is the frequency.[32,33] There are three types of electrons:

1. The first type are electrons common in the saturated bond such as the bond between hydrogen and carbon, and carbon and carbon in saturated compounds. This bond is called the σ bond, where the quantity of required energy to excitation for the electrons of bond σ is usually much greater than the energy of ultraviolet radiation. Accordance with that, the saturated compounds do not absorb in this field, so they are often used as solvents.
2. The second type are electrons common in the unsaturated bond. These compounds contain a σ bond, and a π bond.
3. The third type of electrons are those which do not take part in forming bonds between atoms. These electrons are called free electrons n. Indeed, saturated organic compounds do not contain n electrons, because all the electrons in the external levels of carbon and hydrogen take part in the formation chemical bonds. However, the organic compounds which contain nitrogen, oxygen, sulfur and halogens, they contain n electrons. These compounds can absorb ultraviolet or visible radiation, because this radiation can excite electrons n.

2.6.3 Electronic Spectra

Electronic spectrum of a compound is a curve shows the absorption intensity change (absorbability) with the change of the wavelength of radiation passing through the compound under study. The significance for this curve is to know

the wavelength which is the intensity of its absorption and symbolized by the symbol λ_{max}. The intensity of absorption correlates with the solid concentration and the length of the cell the following equation:

$$\mathrm{A} = \varepsilon\, cl \qquad (2.34)$$

where ε is the coefficient of molar absorption at this wavelength, and sometimes called the molar extinction coefficient, c is the concentration of the solid, and l is the length of the cell containing the solid. The equation (2.34) called the Beer-Lambert law.[34] Furthermore, this relationship is not suitable in the case of very high concentrations. Therefore, in practical application are advised use the calibration curve of the absorption in terms of concentration at the peak of the optical absorption of the compound.

References

[1] R. West, *Basic solid state chemistry*, John Wiley & Sons Incorporated, 1999.

[2] D. E Sands, *Introduction to Crystallography*, Courier Dover Publications, 1969.

[3] K. Hefferan. and J. O'Brien, *Earth Materials*, John Wiley & Sons, 2010.

[4] F. C. Phillips, *An introduction to crystallography*, Longmans, Green, 1971.

[5] C. Hammond, *The Basics of Crystallography and Diffraction*, Oxford University Press, 2009.

[6] L. Smart. and E. A. Moore, *Solid State Chemistry: An Introduction*, Boca Raton: CRC Press, 2005.

[7] J.-J. Rousseau, *Basic crystallography*, John Wiley & Sons, 1998.

[8] P. Luger, *Introduction to Crystallography*, Walter de Gruyter, Berlin, New York, 1980.

[9] M. T. Weller, *Inorganic Materials Chemistry*, Oxford University Press, USA, 1995.

[10] C. Suryanarayana. and M. Grant Norton, *X-Ray diffraction: a practical approach*, Plenum Press, New York, 1998.

[11] A. Wold. and K. Dwight, *Solid State Chemistry: Synthesis, Structure, and Properties of Selected Oxides and Sulfides*, Springer, 1993.

[12] S. E. Dann, *Reactions and Characterization of Solids*, The Royal Society of Chemistry, 2000.

[13] L. Ooi, *Principles of X-ray Crystallography,* OUP Oxford, 2010.

[14] W. H. Bragg, *Proc. R. Soc. Lond*, 1913, **88**, 428 -438.

[15] N. Kasai. and M. Kakudo, *X-Ray Diffraction by Macromolecules*, Springer, 2005.

[16] R. J. D. Tilley, *Crystals and Crystal Structures*, John Wiley & Sons, 2006.

[17] A. Altomare., C. Giacovazzo., A. Guagliardi., A. Moliterni., R. Rizzi., and P. Werner, *J. Appl. Cryst*, 2000, **33**, 1180 -1186.

[18] P. E. Werner., L. Eriksson., and M. Westdah, *J. Appl. Cryst*, 1985, **18**, 367 -370.

[19] A. Albinati., and B. T. M. Willis, *International Tables for Crystallography*, 2006, **C**, 710 -712.

[20] R. A. Young, *The Rietveld method*, Oxford University Press, 1995.

[21] H. M. Rietveld*, J. Appl. Cryst*, 1969, **2**, 65-71.

[22] A. Altomare., F. Capitelli., N. Corriero., C. Cuocci., A. Falcicchio., A. Moliterni., and R. Rizzi, *Crystals*, 2018, **8**, 203 (1-18).

[23] A. Coelho, Topas-academic v4.1, 2008.

[24] W. I. F. David, *J. Res. Natl. Inst. Stand. Technol*, 2004, **109**, 107–123.

[25] B. H. Toby, *Powder Diffr*, 2006, **21**, 67 – 70.

[26] G. Psarras, *Elsevier*, 2018, 11-57.

[27] Y. Shimakawa., Y. Kubo., Y. Tauchi., H. Asano., T. Kamiyama., and Z. Hiroi, *Applied Physics Letters*, 2001, **79**, 2791 – 2793.

[28] W. L. Warren., H. N. Al-Shareef., D. Dimos., B. A. Tuttl., and G. E. Pike, *Applied physics letters*, 1996, **68**, 1681 – 1683.

[29] A. Note, *Agilent basics of measuring the dielectric properties of materials*, 2006.

[30] J. N. Wilson., J. M. Frost., S. K. Wallace., and A. Walsh, *APL Materials*, 2019, **7**, 010901.

[31] J. Garche, C. K. Dyer, P. T. Moseley, Z. Ogumi, D. A. Rand, and B. Scrosati, *Encyclopedia of electrochemical power sources*, Newnes, 2013.

[32] B. J. Clark, T. Frost, M. A. Russell, and Ultraviolet Spectrometry Group (Great Britain), *UV spectroscopy: techniques, instrumentation, data handling*, Springer, 1993.

[33] P. S. Kalsi, *Spectroscopy of Organic Compounds*, New Age International, 2007.

[34] R. J. Anderson, D. J. Bendell, P. W. Groundwater, and Royal Society of Chemistry (Great Britain), *Organic spectroscopic analysis*, Royal Society of Chemistry, 2004.

3. Experimental Details and Analytical Techniques

3.1 Introduction

This chapter describes the synthesis of quaternary perovskite, and their analyses via X-ray powder diffraction. The dielectric measurements of these new quaternary perovskite materials are described as well as their effective magnetic moments, and UV-vis absorption spectra.

All chemicals were used as received by the suppliers (Sigma Aldrich, Acros, Alfa Aesar) unless stated otherwise. All solvents were used as supplied (Laboratory, Analytical or HPLC grade), without further purification.

3.2 Chemicals and Synthesis

Starting materials were applied as received from their sources; bismuth oxide (Bi_2O_3), manganese oxide (MnO_2), nickel oxide (NiO), zinc oxide (ZnO), cobalt oxide (CoO), copper oxide (CuO), and chromium oxide (Cr_2O_3) from Sigma-Aldrich. Potassium bromide (KBr) was sourced from Sigma-Aldrich.

3.2.1 Perovskites Synthesis

The combination of the quantities of bismuth oxide, Bi_2O_3, manganese oxide, MnO_2, and nickel oxide NiO, were used to prepare the perovskite quaternary samples, $Bi_2Mn_xNi_{2-x}O_6$. The value of x was adjusted in 0.1 increments to identify composition that would give rise to a single phase. The quantity of Bi_2O_3 used

was 5 g for across all sample preparations. The mass of each oxide was calculated based on the values of x, which are listed in Table (3.1).

Table 3.1: The mass of oxides [in grams (g)].

The value of x	Mn_xO_2	$Ni_{2-x}O$	$Co_{2-x}O$	$Zn_{2-x}O$	$Cu_{2-x}O$	Cr_xO_3	$Ni_{2-x}O$
0	0.000	1.603	1.608	1.747	1.707	0.000	1.603
0.1	0.093	1.523	1.528	1.659	1.622	0.107	1.523
0.2	0.187	1.443	1.447	1.572	1.537	0.215	1.443
0.3	0.280	1.363	1.367	1.485	1.451	0.322	1.363
0.4	0.373	1.282	1.287	1.397	1.366	0.429	1.282
0.5	0.467	1.202	1.206	1.310	1.280	0.537	1.202
0.6	0.560	1.122	1.126	1.223	1.195	0.644	1.122
0.7	0.653	1.042	1.045	1.135	1.110	0.751	1.042
0.8	0.746	0.962	0.965	1.048	1.024	0.858	0.962
0.9	0.840	0.882	0.884	0.961	0.939	0.966	0.882
1.0	0.933	0.802	0.804	0.873	0.854	1.073	0.802
1.1	1.026	0.721	0.724	0.786	0.768	1.180	0.721
1.2	1.120	0.641	0.643	0.699	0.683	1.288	0.641
1.3	1.213	0.561	0.563	0.611	0.598	1.395	0.561
1.4	1.306	0.481	0.482	0.524	0.512	1.502	0.481
1.5	1.399	0.401	0.402	0.437	0.427	1.609	0.401
1.6	1.493	0.321	0.322	0.349	0.341	1.717	0.321
1.7	1.586	0.240	0.241	0.262	0.256	1.824	0.240
1.8	1.679	0.160	0.161	0.175	0.171	1.931	0.160
1.9	1.772	0.080	0.080	0.087	0.085	2.039	0.080
2	1.866	0.000	0.000	0.000	0.000	2.146	0.000

Then, the quantities of oxides were mixed with each other by grinding in an agate mortar and pestle. The milling was also carried out in a planetary mono mill called Fritsch Pulverisette 6 classic line, which is a high-performance ball mill with a single grinding bowl mount with adjustable imbalance compensation system. This grinding machine provides a high-energy grinding effect of up to

650 rpm. This provides a consistently high grinding output with low space requirements, in order to achieve loss-free grinding of hard, medium-hard, brittle and moist materials, dry in suspension or in inert gas.

After this the three reagent mixture was compressed to 8 ton pressure utilising a KBr die and hydraulic press to create pellets. The oxide pellets were heated in either platinum or porcelain crucibles, in order to prepare the pellets. The temperature profile of the high temperature stage was 800 ℃ for 9h, 850 ℃ for 15h and 875 ℃ for 9h. This process was repeated twice, with intermittent grinding between each heating cycle.[1-2] The selected heating cycle implemented to obtain a dense structure of perovskite with controlled grain growth. The densification was occurred by the grain boundary migration and grain boundary diffusion. This migration results in densification with rapid grain growth and the other heating temperature was to suppress the grain growth.[3]

3.3 The Characterisation and Data Collection

3.3.1 Fourier transform infrared spectra were acquired by FT-IR spectrum

FT-IR spectroscopy can be used to determine the information about the wavelength and the adsorption intensity. This information helps to investigate the existing functional groups in the compounds. The FT-IR spectrum is consisted of absorption peaks which are associated with the vibration frequencies of atomic bonds in the compound. This technique is good for qualitative analysis because the peak intensities are the direct indications of the nature of the given materials.

In this work, FT-IR analysis was utilized to determine the characteristic wave numbers and the adsorption intensities before and after sintering of perovskite characteristic material, $Bi_2Mn_xNi_{2-x}O_6$.

3.3.2 Scanning Electron Microscopy and Energy Dispersive X-Ray Spectroscopy

For scanning electron microscopy and Energy Dispersive Spectroscopy (EDS), the JEOL JSM-7100F LV FEG microscope was used. This microscope provides imaging of samples using Secondary (SEI) and Back-scatter electron imaging (BEI) modes for the elemental analysis and mapping. The microscope is equipped with the low vacuum (LV) detector option and an Oxford Instruments X-Maxn EDS with 80 mm 2 window along with the Aztec analysis software for imaging. The images were taken on 20 kV accelerating voltage and with the 10.0 mm distance. The samples are shown below representing the before (sample 1) and after (sample 2) carbon coating for SEM analysis as shown in Figure (3.1).

Figure 3.1: Carbon coating for SEM analysis, (sample 1) is the quaternary of perovskite samples $Bi_2Mn_{1.3}Ni_{0.7}O_6$ before heating, and (sample 2) after heating.

3.3.2.1 Sputter coating

The instrument used for sputter coating was a Quorum Q150R ES Sputter Coater for the sample preparation of SEM and EDS analysis. This equipment coated the sample with gold deposition (nm accuracy) for SEM analysis and coated carbon for EDS analysis.

3.3.3 X-ray diffraction

The X-ray diffraction (XDF) instrument was used to measure 2θ. This process was performed through the following steps:

• The diffraction patterns for the samples were recorded on a Philips X'PertPro diffractometer in Bragg-Brentano geometry using a monochromator C_u-$K_{\alpha 1}$ X-ray source with $\lambda = 1.54056$ Å.

• Samples in powder form were packed into holders as shown in Figure (3.2).

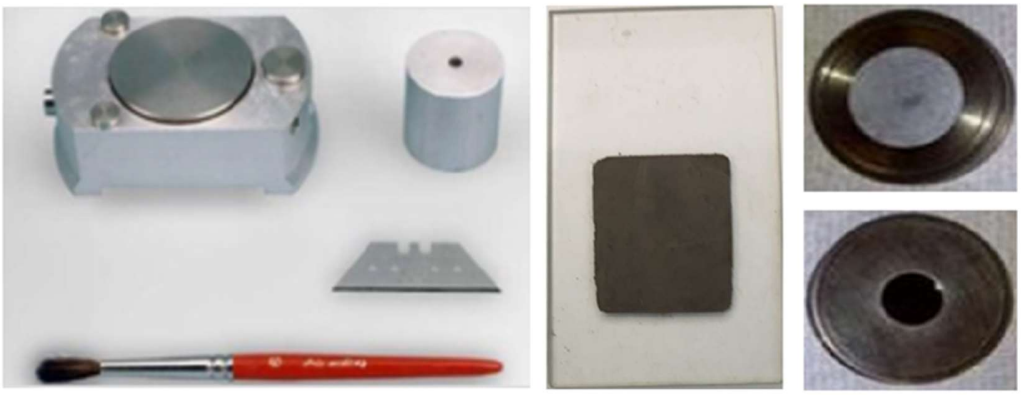

Figure 3.2: The cavity slide method of specimen preparation.

The diffractometer unit was controlled at 45 kV and 40 mA (a Philips X'PertPro) and (Smartlab Studio), and then data were collected within the range $5° \leq 2\theta \leq 90°$. In addition, scans were usually carried out with steps of $0.002°$.

3.4 Rietveld refinement

In this work, Rietveld analysis to refine of all samples was by using TOPAS Academic program,[4] which to be performed on powder X-ray data. The program operates by operating window called JEdit,[5] which is designed to interface with the full pattern analysis software suite TOPAS.

3.5 Dielectric Measurements

3.5.1 Sample Preparation

The dielectric measurements of the samples were recorded using an Agilent 4284A LCR meter. All samples were prepared by using the same as method that mentioned above in Section (3.2.1). After the thermal procedure, a small amount of the sample pressed under 8 tons in a 13 mm diameter die to form a pellet (disc). In the consideration that, the thickness of the pellet must be less than 1 mm to make the resistance of the pellet negligible. The pellets were then heated at 750 ℃ fortwo hours. After the first heating, the grinding procedure and the pressure was repeated. The samples were then reheated at the same period of time with the same temperature.

3.5.2 Gold Coating

An Edwards Sputter Coater S150B was used to coat the pellets with gold.[6-8] In the following step the two conductive surfaces were isolated by removing the gold from the sides. Soldering has been used to conduct the wires with the surfaces of the pellets, but this method was not used to make electrical connection because this led to the fragile pellets and sample breaking. Finally,

the wires were connected to the surfaces using silver impregnated super glue as shown in Figure (3.3).

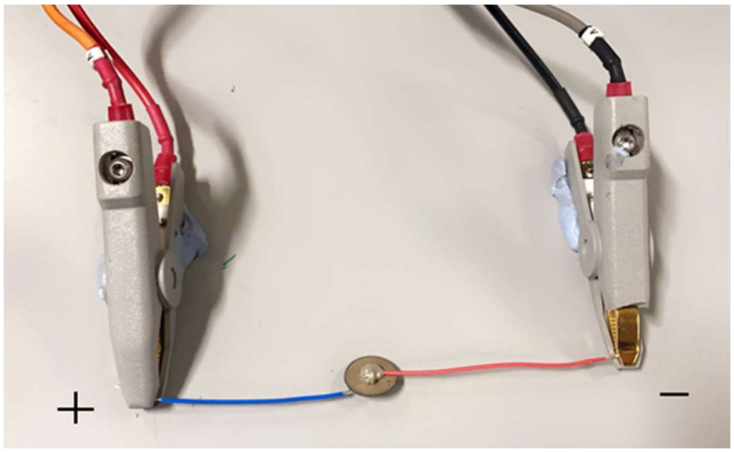

Figure 3.3: Circuit for dielectric measurements.

3.5.3 Calculation of Capacitance and Dielectric Constant

Dielectric measurements were carried out using an Agilent 4284A, which specifically applied to calculate the capacitance of samples at excitation voltage 1 Vrms.

Firstly, the conductivity of the samples was measured through the calculation of the resistance (R) of each sample, in order to decide whether the quaternary perovskite samples are insulating or conductive. The, the capacitance (C_1) of the samples was measured by LCR meter at different frequencies: 1 kHz, 10 kHz, and 100 kHz, and the C_0 was measured by the following equation:

$$C_0 = \frac{\varepsilon_0 A}{d} \qquad (3.1)$$

Where C_0 is capacitance of vacuum, C_1 is the capacitance of dielectric medium, A is the area of the capacitor plates which is equal to πr^2, r is the diameter of the surface and d is the distance among two surfaces (or the thickness of sample) as shown in figure (3.3); d and r was measured by Vernier calliper.[9]

The dielectric constant of a material is related to the increase in capacitance by the following equation:

$$\varepsilon'_r = \frac{C_1}{C_0} \qquad (3.2)$$

Where C_1 is capacitance with dielectric medium present, and ε'_r is the real dielectric constant or permittivity of the material.

3.6 Magnetic Moments Measurements

In general, ferromagnetic materials are defined as a unique constructions and structures, which have the capability to keep their single magnetic field, then this field turns to a permanent magnetic field. In this study, ferromagnetic materials were detected using Sherwood Scientic Magnetic Susceptibility Balance (MSB)Auto instrument, through four steps:

A specific quantity of samples that was prepared previously and heated to the appropriate temperature as described in Section (3.2.1) has put within a tube.

This tube was put in MSB instrument, where magnetic balance can create gram susceptibilities (χ_g) data for a specific paramagnetic substance.

The molar magnetic susceptibility (χ_m) of samples was calculated using the following equation:

$$\chi_m = \chi_g \times R.M.M \qquad (3.3)$$

where (R.M.M) is the molecular weight of the compound.

Calculating the effective magnetic moment (μ_{eff}) using the following equation:

$$\mu_{eff} = 2.83\sqrt{T_A \chi_m} \qquad (3.4)$$

Where T_A is the absolute room temperature

3.7 Measurement of Electronic Spectra

The spectrum of sample radiation absorption is important in showing the electronic construction and structure of a compound from absorption in the visible and ultraviolet region. The particular absorption can yield details of the electronic structure of a compound, and hence, assist in understanding of the conductive properties of the material.

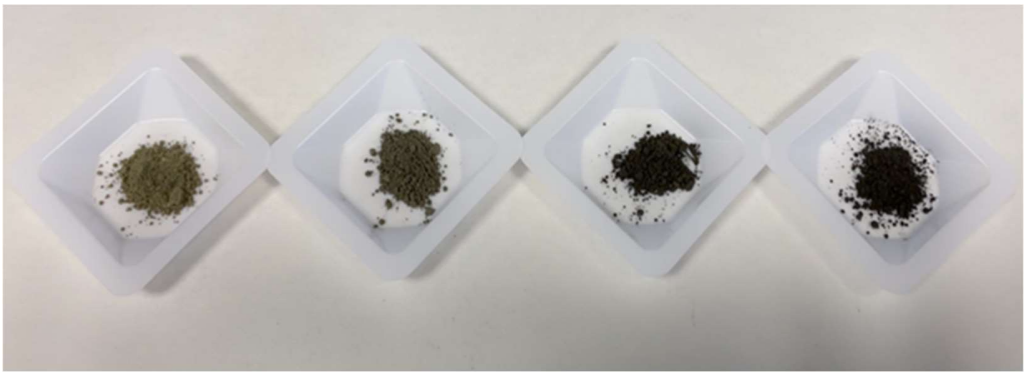

Figure 3.4: Color of UV-vis specimen before heating.

However, chemical compounds differ from one another, in terms of structure and composition, which may be reflected by similarities or differences in their color. While white light passes through or reflects from a material, a colored material absorbs part of the spectrum. Therefore, color is one of the most prominent features of oxides, as the absorptivity of these colors distinguishes the oxides from each other. The color of samples after heating also depends on the sintering conditions. In this work, all the samples had blackish color after heating which can be attributed to the fact that the blackish color is due to the

intervalence charge transferring resulting from the partially multivalent cations reduction.[10]

The electronic spectra of the samples were measured using a UV-vis spectrophotometer device (JASCO V-670 Spectrophotometer), in three steps, as follows:

- Taking a small amount of samples that had been prepared previously and that had been clarified in detail in Section (3.2.1).
- Each sample was ground into a soft powder, from which small samples were taken.
- Before analysis of the sample using the UV-vis spectrophotometer, a reading of background spectra was taken first, in order to register the back-ground spectrum of the air in the sample compartment.
- The sample was introduced into a holder with a circular hole of 1 cm (diameter).
- The holder was set vertically in the UV-vis spectrophotometer, the scanning speed was set at 400 nm/min and the wavelength of the absorption fixed in the range of 200−2000 nm.

References

[1] H. Hughes, M. M. B. Allix, C. A. Bridges, J. B. Claridge, X. Kuang, H. Niu, S. Taylor, W. Songand, and M. J. Rosseinsky, *J. Am. Chem. Soc.*, 2005, **127**, 13790 – 13791.

[2] J. B. Claridge, H. Hughes, C. A. Bridges, M. Allix, M. R. Suchomel, H. Niu, X. Kuang, M. J. Rosseinsky, N. Bellido, D. Grebille, O. Perez, C. Simon, D. Pelloquin, S. J. Blundell, T. Lancaster, P. J. Baker, F. L.Pratt, and P. Shiv Halasyamani, *J. Am. Chem. Soc.*, 2009, **131**, 14000 – 14017.

[3] U. Sutharsini, M. Thanihaichelvan, and R. Singh, *Two-step sintering of ceramics.* Sintering of Functional Materials, 2018.

[4] A. Coelho, *Topas-academic v4.1*, 2008.

[5] S. Pestov, *JEdit*, Ottawa, 1998.

[6] T. Ina, Y.Orikasa, H. Arai, Y.Uchimotoa, and Z.Ogumib, *J. Mater. Chem.*, 2011, **21**, 10061–10068.

[7] E.Bsaibess, F.Delorme, I.Monot-Laffez, and F. Giovannelli, *Scripta Materialia.*, 2021, **201**, 113950.

[8] M. M. A. Sekar, and A. Halliyal, *J. Am. Ceram. Soc.*, 1998, **81**, 380–88.

[9] S. Hajra, M. Sahu, V. Purohit, and R.N.P. Choudhary, *Heliyon.*, 2019, **5**, 01654.

[10] A. M. Hofmeister, *J. Appl. Phys.*, 2010, **107**, 103532.

4. The Bismuth-Manganese-Cobalt oxide system

4.1 Rietveld Analysis

This section presents the obtained x-ray powder diffraction results for the $Bi_2Mn_xCo_{2-x}O_6$ materials, where value of x is varied 0.0 to 2.0. The XRD results are shown in Figures (4.1), (4.2), (4.3) and (4.4) are for the values of x=0.0 to 2.0.

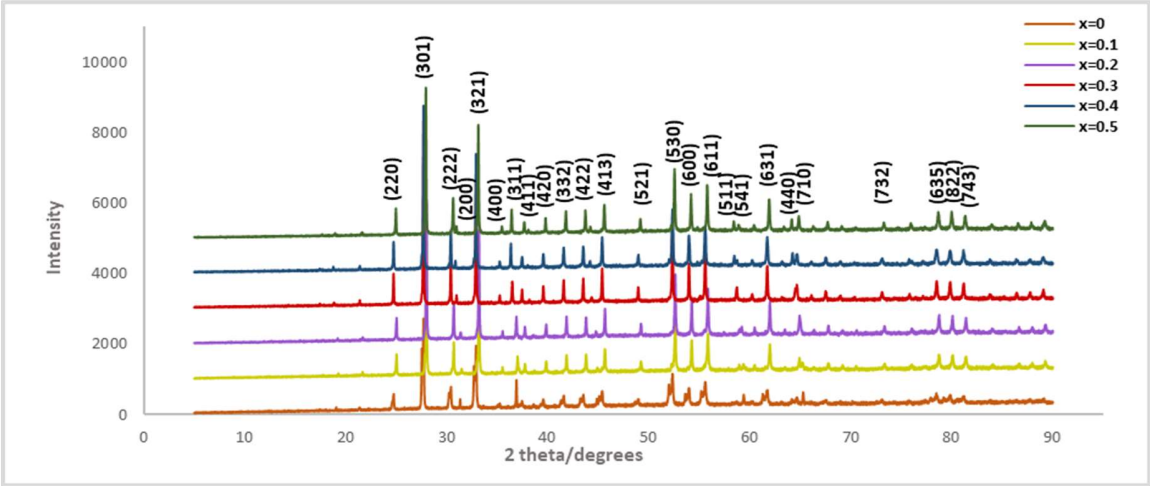

Figure 4.1: XRD results of $Bi_2Mn_xCo_{2-x}O_6$ for x= 0.0 to 0.5.

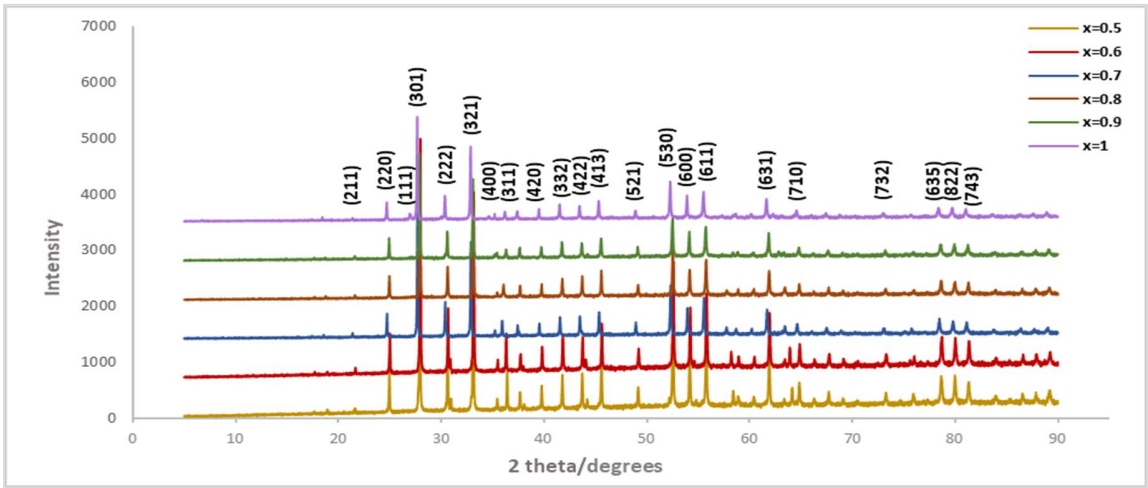

Figure 4.2: XRD results of $Bi_2Mn_xCo_{2-x}O_6$ for x=0.5 to 1.0.

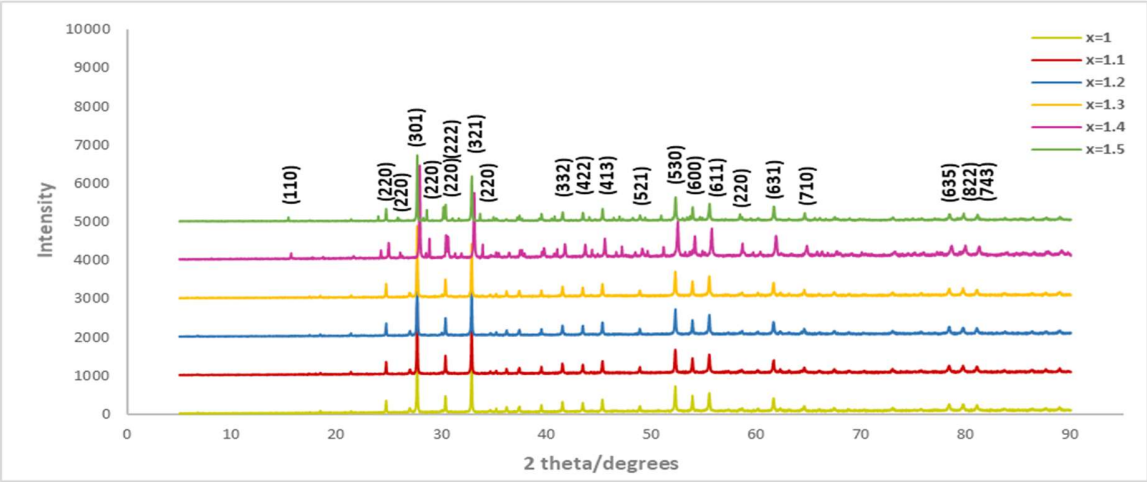

Figure 4.3: XRD results of $Bi_2Mn_xCo_{2-x}O_6$ for x= 1.0 to 1.5.

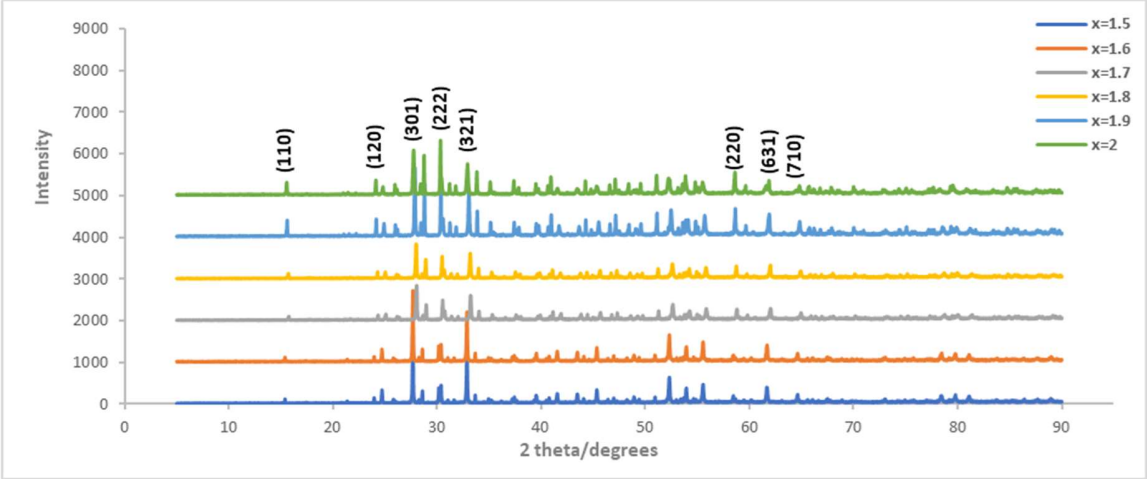

Figure 4.4: XRD results of $Bi_2Mn_xCo_{2-x}O_6$ for x= 1.5 to 2.0.

The x-ray powder diffraction data have been refined using Topas academic software, where results revealed that the $Bi_2Mn_xCo_{2-x}O_6$ compound at x=0.0 and x=2.0 showed crystal properties of each composition, but the structure of the $Bi_2Mn_xCo_{2-x}O_6$ at these values are not pure phase in any of the composition. The refinement confirms the presence of multiple phases with the reflection observed from the various planes in Figures (4.5) to (4.8). The prepared samples observed to have Fm3m, I23, and Pbam space groups which further confirm the cubic structure, tetragonal and orthorhombic structures respectively, in the compositions as discussed in Tables (4.1) and (4.2).

Table 4.1: The obtained data from the structure refinement by Topas Academic software of $Bi_2Mn_xCo_{2-x}O_6$ when x=0.0 and x=0.6.

The value of x	0			0.6	
Rwp	8.31%			10.42%	
Properties	$Bi_{12.24}Co_{12.8}O_{40}$ [1]	$Bi_{24.96}Co_1O_{40}$ [1]	Co_3O_4 [2]	$Bi_{12}MnO_{20}$ [3]	$Co_{2.2}Mn_{0.8}O_4$ [4]
a=b=c	10.198	10.255	8.087	10.205	8.274
α=β=γ	90^0				
Space group	I23	I23	Fd-3mS	I23	Fd -3mZ
Cell volume	1060.684	1078.575	528.955	1060.738	566.522
Number of equivalent positions	24		192	24	192
Number of independent parameters	31			19	

Table 4.2: Characteristics and properties of the obtained data from the structure refinement by Topas Academic software of $Bi_2Mn_xCo_{2-x}O_6$ when x=1.0 and x=1.7.

The value of x	1.0			1.7	
Rwp	14.44%			18.67%	
Properties	$Bi_{12}MnO_{20}$ [3]	$Co_{2.1}Mn_{0.9}O_4$ [4]	Bi_2O_3 [5]	$Bi_2Mn_4O_{10}$ [6]	$Bi_{19.68}Co_{6.2}O_{40}$ [1]
a	10.206	8.238	5.732	7.565	10.212
b				8.547	
c				5.770	
α=β=γ	90^0			90^0	
Space group	I23	Fd -3mZ	Fm-3m	Pbam	I23
Cell volume	1063.076	558.998	188.327	373.119	1064.830
Number of equivalent positions	24	192		8	24
Number of independent parameters	24			28	

Furthermore, the XRD patterns showed some presence of impurities as can be seen in XRD patterns which could not be identified fully. But some of the information about their classifications have been discussed in Tables (4.1), (4.2), and illustrated in Figures (4.5), (4.6), (4.7) and (4.8).

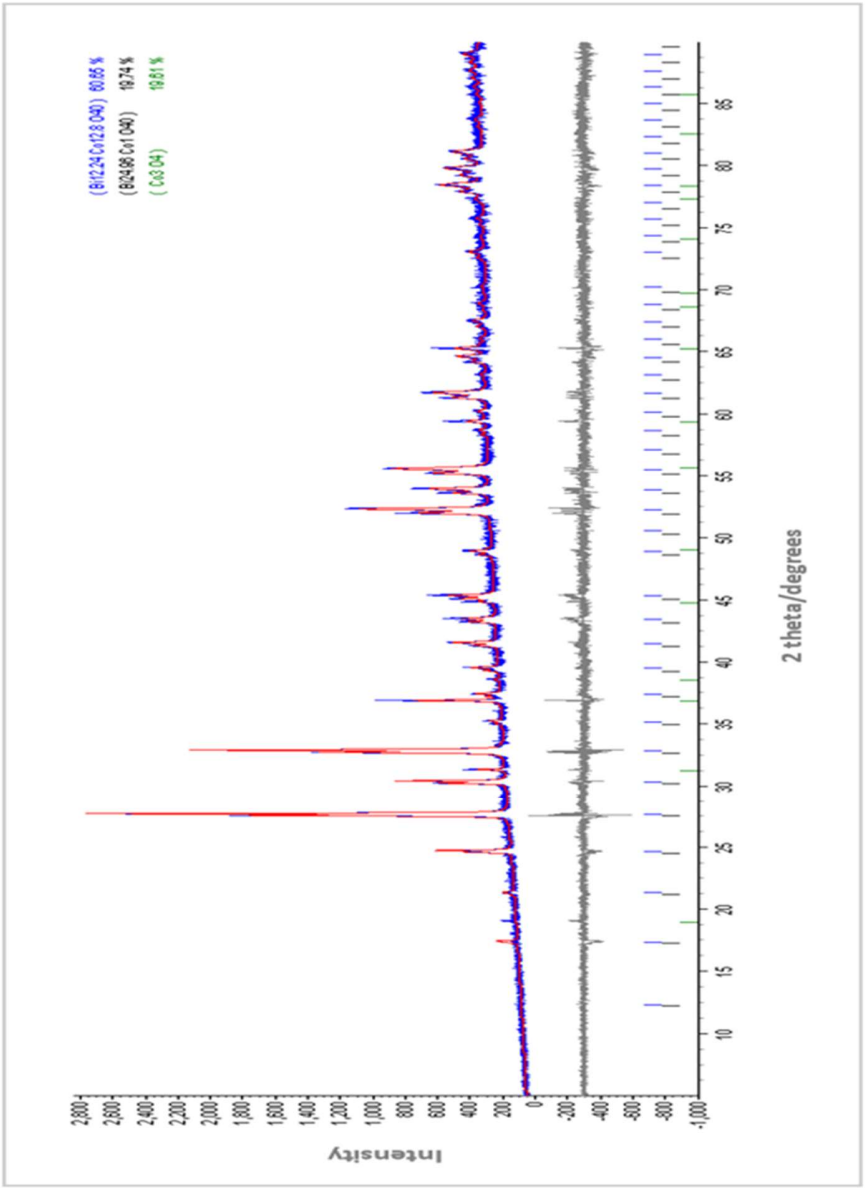

Figure 4.5: X-ray powder diffraction pattern Rietveld fit for $Bi_2Mn_0Co_2O_6$ (x=0.0).

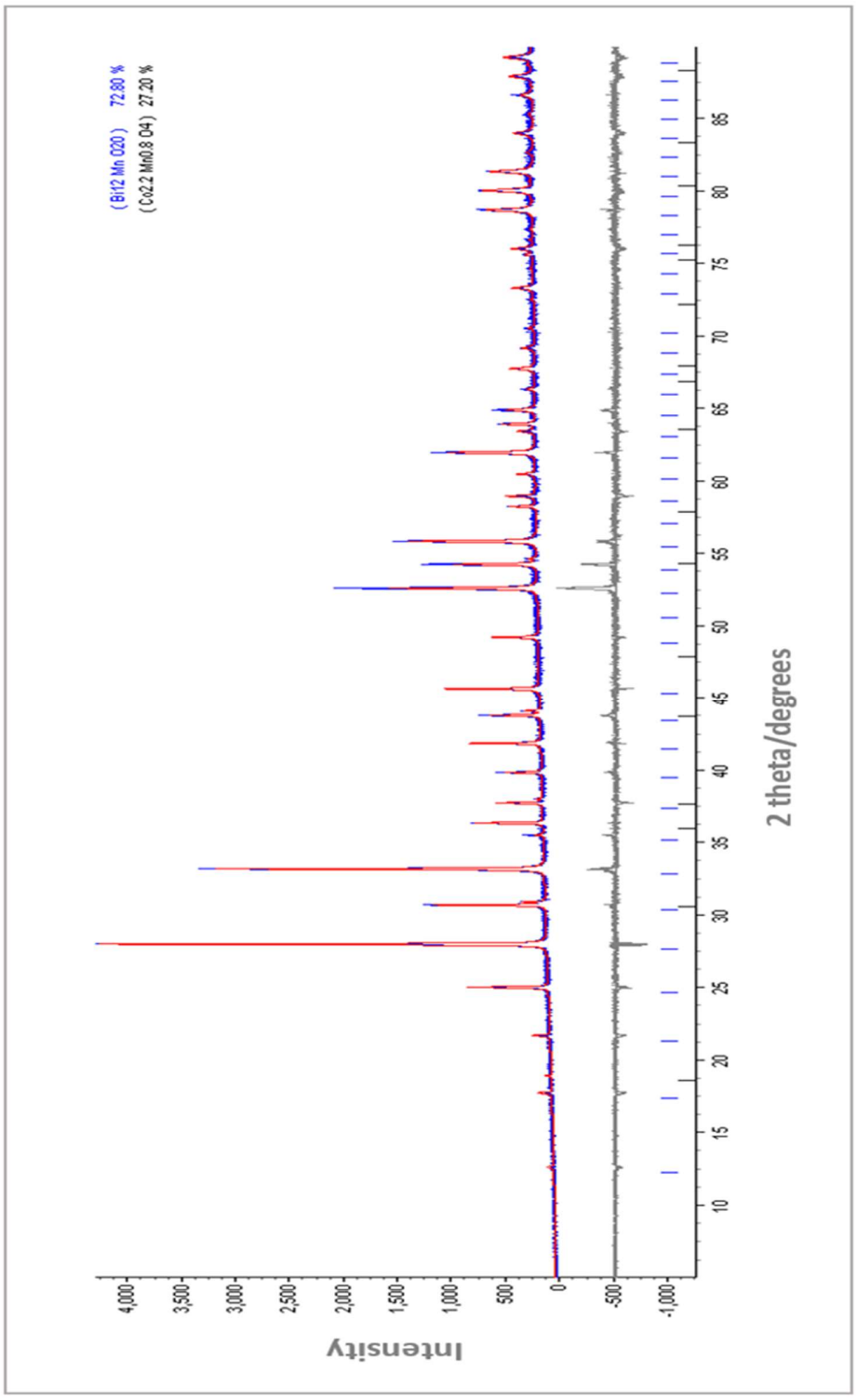

Figure 4.6: X-ray powder diffraction pattern Rietveld fit for $Bi_2Mn_{0.6}Co_{1.4}O_6$ (x=0.6).

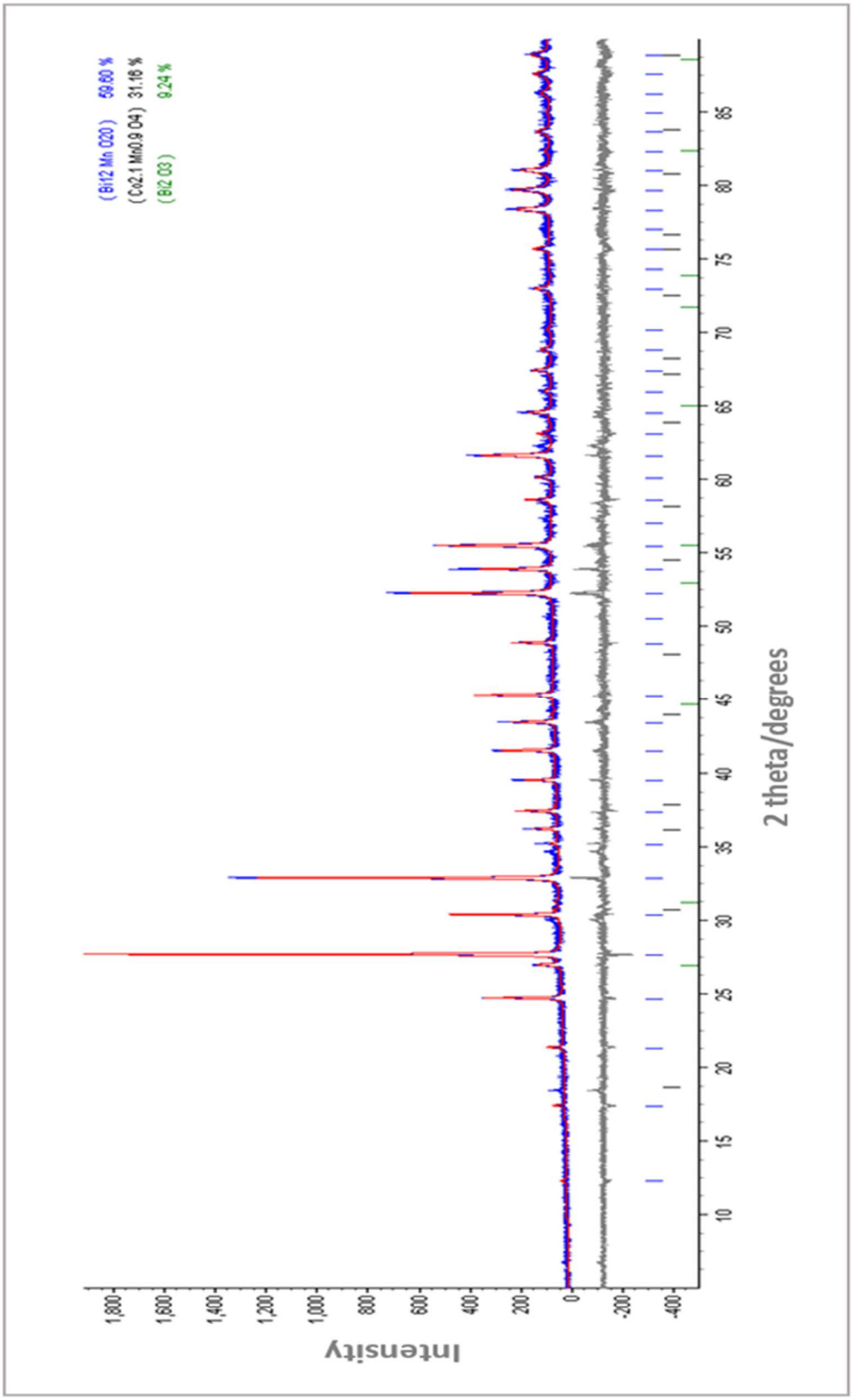

Figure 4.7: X-ray powder diffraction pattern Rietveld fit for $Bi_2Mn_1Co_1O_6$ (x=1.0).

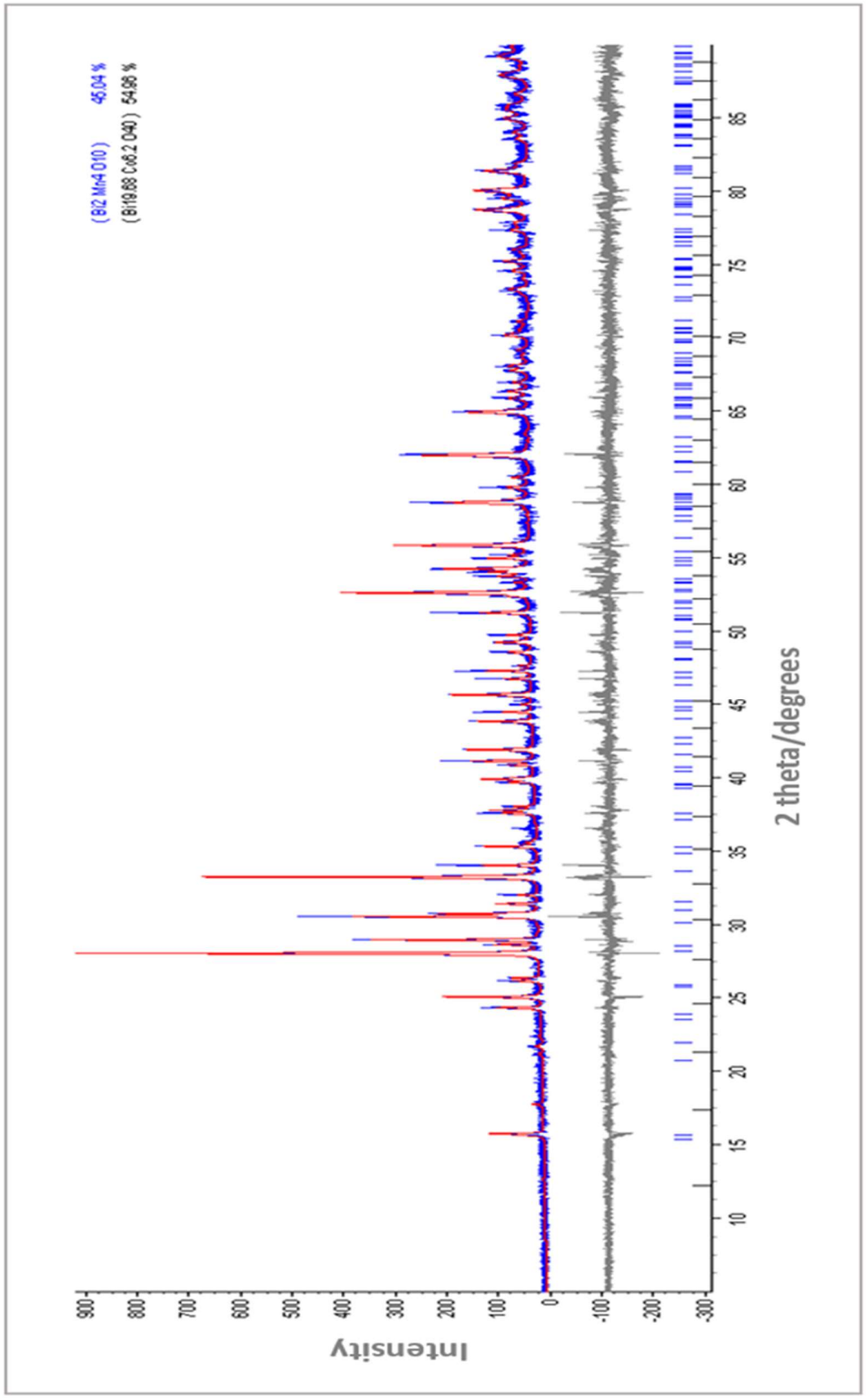

Figure 4.8: X-ray powder diffraction pattern Rietveld fit for $Bi_2Mn_{1.7}Co_3O_6$ (x=1.7).

Cobalt ions were replaced by manganese ions randomly at the octahedral 24 f-sites. This substitution has shown very little peak shifts in diffraction pattern towards higher 2θ. This shifting indicates the lattice contraction has occurred because of the manganese substitutions in cobalt. The ionic radius of bismuth is 1.030 Å, cobalt is 0.545 Å and Manganese is 1.790 Å.[7] Since the radius of Mn is higher than Co, therefore, the peaks are shifting towards the higher 2θ. However, this difference in peak was not that high what to be expected for x=0.1 to 1.7 as shown in figure (4.5) to (4.8), and the unfavourable presence of impurities. The reason can be attributed to the sintering and sample preparation conditions because high pressure synthesis is required for the fabrication of $BiCoO_3$ perovskite with the conventional methods such as solid-state method and in this work, the atmospheric pressure was used for the synthesis.[8, 9]

The Reitveld analysis of $Bi_2Mn_xCo_{2-x}O_6$ with the values of x=0.0, 0.6, 1.0 and 1.7 showed some the presence of impurity phases. The $Bi_2Mn_xCo_{2-x}O_6$ with x=0.0 is showing the composition and properties of original $BiCoO_3$in figure (4.5). The compound observed in this composition were $Bi_{12.24}Co_{12.8}O_{40}$ (60.65%), $Bi_{24.96}Co_1O_{40}$ (19.74%) and Co_3O_4(19.61%). The characteristics and properties of each compounds present in $Bi_2Mn_xCo_{2-x}O_6$ for x=0.0 is shown in table (4.1). It can be seen that multiple phases have been observed in this pure composition. The reason is the synthesis of perovskite in the ambient atmosphere and not utilizing the high pressure. The Bismuth based perovskites require high pressure synthesis to stabilize the perovskite structure in the composition because of the presence of Bi^{3+} lone pair which does not form the no centrosymmetric structure.[10] In the table (4.1), Rwp defines the weighted profile of Rietveld analysis which is good fit if <10. In this case, it is 8.31% which is said to be good fit results of refinement. The number of equivalent positions shows the number of positions occupied by atoms in a unit cell.

In figure (4.6), the Reitveld analysis of $Bi_2Mn_xCo_{2-x}O_6$ for x=0.6 has shown. The figure shows presence of two phases like $Bi_{12}MnO_{20}$ (72.90%) and $Co_{2.2}Mn_{0.8}O_4$

(27.20%). The characteristics and properties of each compounds present in $Bi_2Mn_xCo_{2-x}O_6$ for x=0.6 is shown in table (4.1). the Rwp in this analysis was 10.415% which is nearly good fit results of refinement. However, perovskite structure could not be stabilized due to ambient pressure synthesis.

In figure (4.7), the Rietveld analysis of $Bi_2Mn_xCo_{2-x}O_6$ for x=1.0 has shown. The figure shows presence of multiple phases like $Bi_{12}MnO_{20}$ (59.60%) and $Co_{2.1}Mn_{0.9}O_4$ (31.16%) and Bi_2O_3 (9.24%). The characteristics and properties of each compounds present in $Bi_2Mn_xCo_{2-x}O_6$ for x=1.0 is shown in table (4.2). the Rwp is high in his case which is 14.44% and representing less accuracy in goodness of fit results. Perovskite structure could not be stabilized due to ambient pressure synthesis.

In figure (4.8), the Reitveld analysis of $Bi_2Mn_xCo_{2-x}O_6$ for x=1.7 has shown. The figure shows presence of multiple phases like $Bi_2Mn_4O_{10}$ (45.04%) and $Bi_{19.68}Co_{6.2}O_{40}$ (54.96%). The characteristics and properties of each compounds present in $Bi_2Mn_xCo_{2-x}O_6$ for x=1.7 is shown in table (4.2). This composition confirms the presence of orthorhombic structure in $Bi_2Mn_4O_{10}$. But the Rwp showed very high value of 18.67% and representing low accuracy in refinement results. The purpose of presenting this result is due to the presence of ferroelectric properties in this composition which is further discussed in Section (4.2). But also in this case, perovskite structure could not be stabilized due to ambient pressure synthesis.

It can be seen that single phase could not be identified in any of the composition. The reason as mentioned before that all the other bismuth-based structure requires high pressures to stabilize the perovskite structures. The presence of 6s lone pair of magnetic Bi^{3+} ions in Bi-based compounds oxides shows at B-site has some magnetic properties because of the different exchange couplings obtain from their differing magnetic moment and involvement of orbital symmetry. Because these lone pair does not always form no centrosymmetric

structures.[10] The effect of these ions on the magnetic and electric properties has explained below.

4.2 Dielectric measurement

The obtained results of dielectric measurements for the $Bi_2Mn_xCo_{2-x}O_6$ combination have been conducted by using the same instrument LCR meter and the steps which are reported in detail in Chapter 3, where the measurements have observed under different frequencies. Table 4.3 shows the conductance and capacitance values of the $Bi_2Mn_xCo_{2-x}O_6$ with respect to varying x values.

Table 4.3: The dielectric results of the $Bi_2Mn_xCo_{2-x}O_6$ combination.

Value of x	Capacitance			Conductance		
	1 kHz	10 kHz	100 kHz	1 kHz	10 kHz	100 kHz
	C (pF)	C (pF)	C (pF)	G (μS)	G (μS)	G (μS)
0.0	695.70	463.60	233.20	52.60	61.60	121.27
0.1	101.41	71.76	50.56	2.14	3.09	8.83
0.2	120.40	82.28	57.09	3.01	4.14	10.70
0.3	106.14	68.41	47.81	2.33	3.23	8.20
0.4	122.63	76.18	53.02	2.53	3.61	9.11
0.5	177.12	118.01	80.49	4.50	6.25	15.80
0.6	211.50	133.30	87.30	5.67	7.80	19.36
0.7	127.08	77.47	53.18	2.52	3.76	10.16
0.8	185.15	118.43	80.02	4.53	6.36	16.85
0.9	253.70	150.90	99.66	6.06	9.00	21.89
1.0	385.40	233.40	153.63	10.90	15.07	35.94
1.1	139.30	88.06	57.46	4.02	5.25	14.06
1.2	175.57	105.62	69.27	3.44	4.93	16.11
1.3	128.08	79.76	50.87	2.83	3.89	12.45
1.4	197.53	111.23	69.40	4.07	5.28	17.45
1.5	166.83	100.44	65.09	3.67	5.36	16.65
1.6	204.67	127.92	91.55	3.94	5.81	17.25
1.7	809.30	231.08	63.80	9.10	21.50	43.70
1.8	146.30	88.65	56.71	2.61	4.07	15.04
1.9	192.51	113.62	72.84	3.33	5.17	19.29
2.0	55.51	40.62	29.95	0.13	0.57	3.82

Figure (4.9), (4.10) and (4.11) shows the graphs of capacitance (pF), conductance (μS) and conductivity (μS/cm) with respect to the value of x at different frequencies 1000Hz, 10000Hz and 100000Hz. The trends in all the graphs are identical. The values obtained for x=1.0 and x=1.7 has some higher values of capacitance (pF), conductance (μS) and conductivity (μS/cm) as compared to the other.

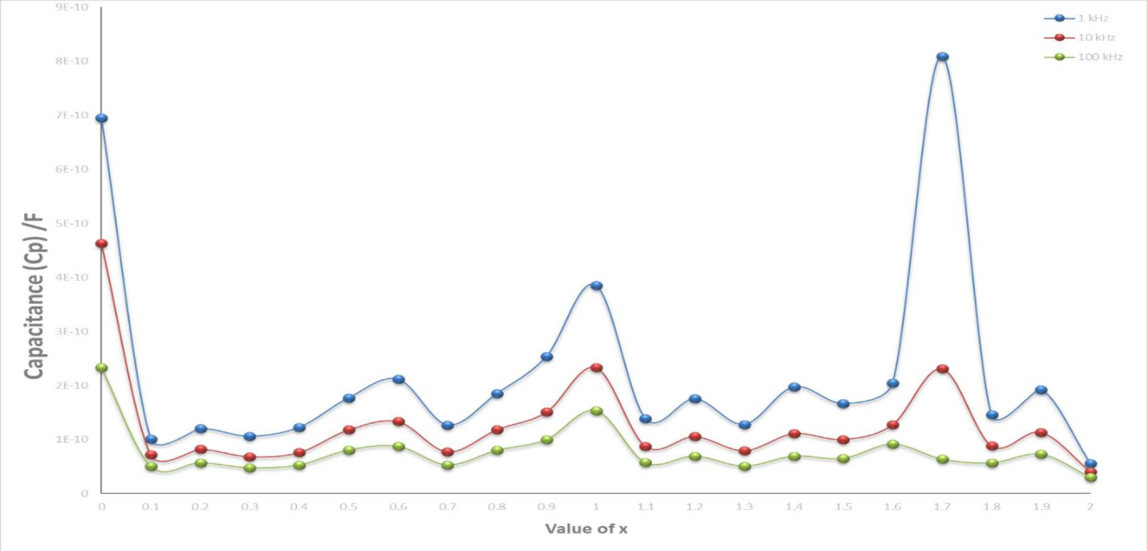

Figure 4.9: Capacitance (pF) of the $Bi_2Mn_xCo_{2-x}O_6$ combination.

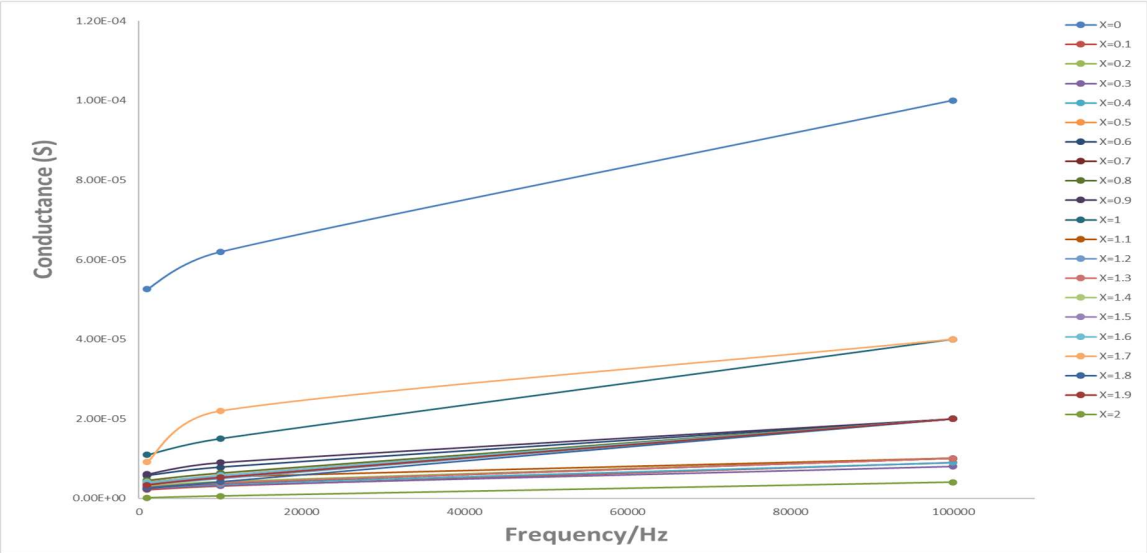

Figure 4.10: Conductance (μS) of $Bi_2Mn_xCo_{2-x}O_6$ combination.

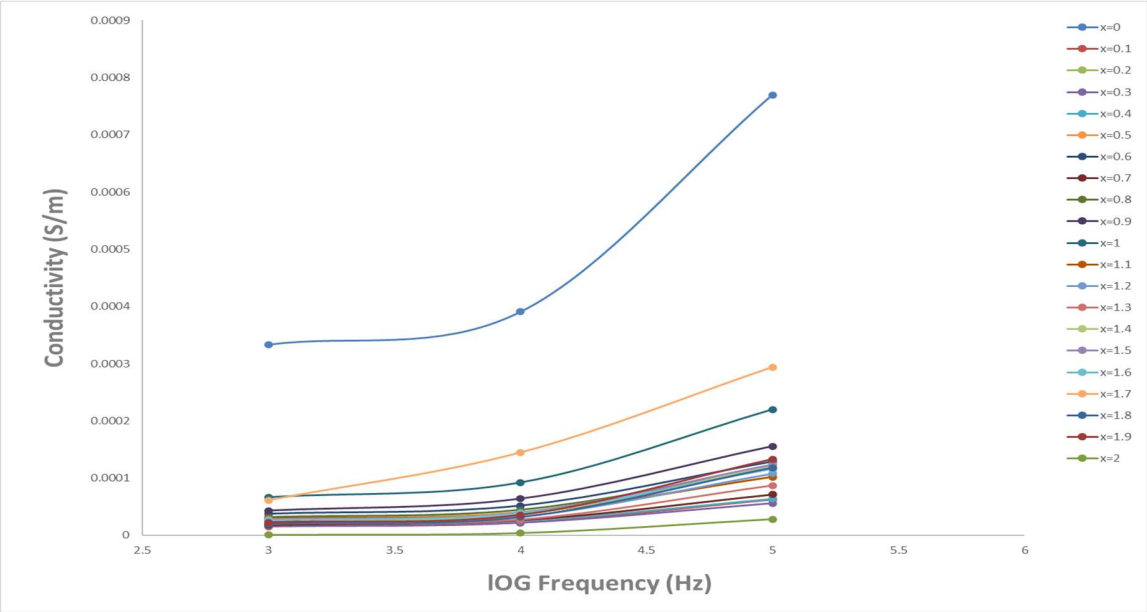

Figure 4.11: Conductivity of $Bi_2Mn_xCo_{2-x}O_6$ perovskite.

The increase in capacitance, conductance and conductivity, with respect to frequency shows that the materials are responsive to higher frequencies. It can also be seen that the capacitance, conductance and conductivity have decreased with the increase in Mn content in the $BiCoO_3$ compound at 750 ℃ temperature. This can be said that Mn doping in the $BiCoO_3$ perovskite resulted in less ferroelectric properties because of the weak hybridization between the Mn and O ions because as reported by Cai *et al* in pure $BiCoO_3$, the hybridizations between Bi–O and Co–O play important roles for the nature of the ferroelectricity and ferromagnetism.[13] This can be attributed to the naturally presence of oxygen vacancies in the $BiCoO_3$ perovskite. These vacancies produce defect dipoles with Co and Mn ions at grain boundaries. The bonds between dipoles defect inhibit the Co ions diffusion in the BMC ($Bi_2Mn_xCo_{2-x}O_6$) lattice and can create high segregation at grain boundaries with the increasing Mn content. This is also responsible for less solubility of Co ions in samples.[14]

Table (4.4) shows the Results of the electrical conductivity, dielectric constant (ε'), and dielectric loss (ε') of the $Bi_2Mn_xCo_{2-x}O_6$ combination at different frequency of 1000Hz, 10000Hz and 100000Hz.

Table 4.3: Results of the electrical conductivity, dielectric constant (ε'), and dielectric loss (ε') of the $Bi_2Mn_xCo_{2-x}O_6$ combination.

Value of x	Conductivity (S/m)			Dielectric constant (ε')			Dielectric constant (ε'')		
	1 kHz	10 kHz	100 kHz	1 kHz	10 kHz	100 kHz	1 kHz	10 kHz	100 kHz
0.0	3.34×10^{-7}	3.91×10^{-7}	7.7×10^{-7}	498.80	332.410	167.210	6002.52	702.960	138.390
0.1	1.51×10^{-8}	2.18×10^{-8}	6.22×10^{-8}	80.64	57.061	40.204	270.83	39.105	11.175
0.2	1.99×10^{-8}	2.74×10^{-8}	7.08×10^{-8}	90.01	61.509	42.678	358.12	49.256	12.730
0.3	1.59×10^{-8}	2.21×10^{-8}	5.61×10^{-8}	82.05	52.886	36.961	286.68	39.742	10.089
0.4	1.78×10^{-8}	2.54×10^{-8}	6.41×10^{-8}	97.53	60.586	42.167	320.24	45.694	11.531
0.5	2.91×10^{-8}	4.04×10^{-8}	1.02×10^{-7}	129.40	86.185	58.784	523.05	72.646	18.365
0.6	3.77×10^{-8}	5.19×10^{-8}	1.29×10^{-7}	158.80	100.110	65.565	677.74	93.234	23.141
0.7	1.77×10^{-8}	2.64×10^{-8}	7.13×10^{-8}	100.70	61.408	42.154	317.92	47.435	12.818
0.8	3.16×10^{-8}	4.44×10^{-8}	1.18×10^{-7}	145.80	93.287	63.032	567.91	79.733	21.124
0.9	4.31×10^{-8}	6.40×10^{-8}	1.56×10^{-7}	203.70	121.130	80.001	774.22	114.980	27.967
1.0	6.68×10^{-8}	9.23×10^{-8}	2.2×10^{-7}	266.60	161.44	106.260	1199.91	165.900	39.564
1.1	2.92×10^{-8}	3.81×10^{-8}	1.02×10^{-7}	114.20	72.192	47.106	524.52	68.500	18.345
1.2	2.31×10^{-8}	3.31×10^{-8}	1.08×10^{-7}	133.20	80.111	52.540	415.51	59.514	19.448
1.3	1.98×10^{-8}	2.73×10^{-8}	8.73×10^{-8}	101.40	63.149	40.276	356.61	49.018	15.688
1.4	2.82×10^{-8}	3.66×10^{-8}	1.21×10^{-7}	154.50	86.992	54.277	506.61	65.722	21.721
1.5	2.74×10^{-8}	4.00×10^{-8}	1.24×10^{-7}	140.60	84.652	54.859	492.29	71.898	22.334
1.6	2.65×10^{-8}	3.91×10^{-8}	1.16×10^{-7}	155.60	97.274	69.617	476.84	70.316	20.877
1.7	6.12×10^{-8}	1.45×10^{-7}	2.94×10^{-7}	614.60	175.500	48.453	1099.93	259.870	52.821
1.8	2.05×10^{-8}	3.20×10^{-8}	1.18×10^{-7}	130.00	78.802	50.410	369.25	57.580	21.278
1.9	2.30×10^{-8}	3.56×10^{-8}	1.33×10^{-7}	149.90	88.455	56.707	412.60	64.059	23.901
2.0	9.55×10^{-10}	4.15×10^{-9}	2.81×10^{-8}	46.05	33.699	24.847	17.17	7.460	5.044

Figure (4.12) and Figure (4.13) show the relative permittivity (ε′) and dielectric loss (ε′′) for the $Bi_2Mn_xCo_{2-x}O_6$ compounds with the x values ranging from 0.0 to 2.0.

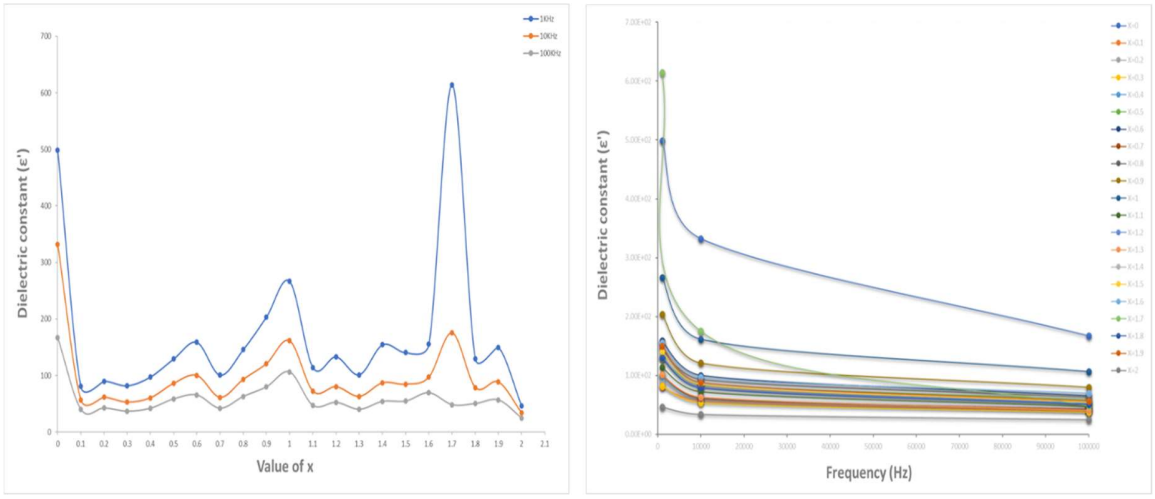

Figure 4.12: Dielectric constant (ε′) of $Bi_2Mn_xCo_{2-x}O_6$ perovskite.

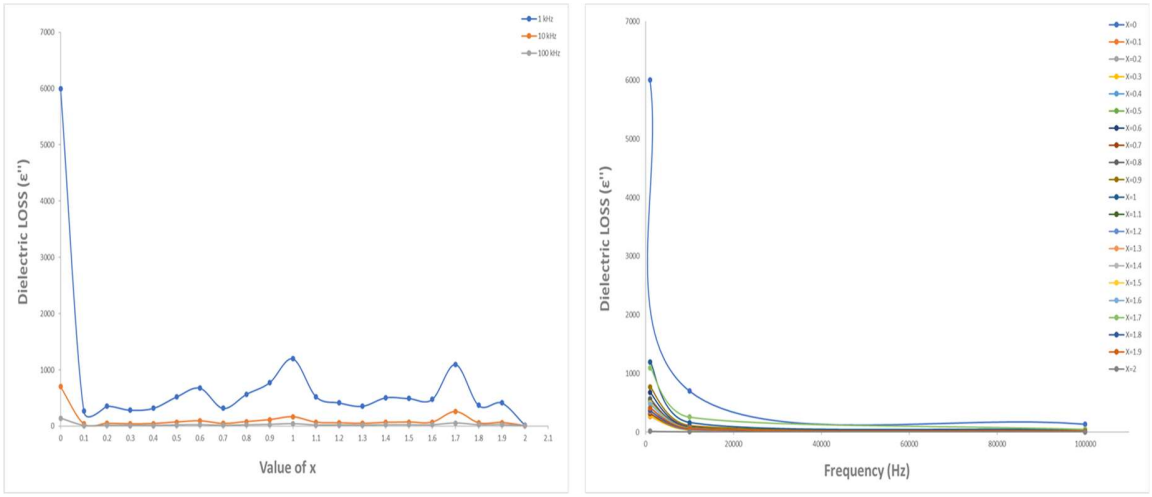

Figure 4.13: Dielectric loss (ε′′) of $Bi_2Mn_xCo_{2-x}O_6$ perovskite.

The dielectric constant and dielectric loss as a function of frequency from 1 kHz, 10 kHz and 100 kHz shown in graph are at constant temperature of 750 ℃. The dielectric constant and dielectric loss are decreasing with the increase in

frequency (100 kHz). This can be attributed to that the polarization is not responsive with the increasing frequency because of the sintering conditions and furnace atmosphere. Also, as the amount of Mn is increasing, these values tend to be decreasing except for the value at x=1.7 which is more prominent at lower frequency (1000 Hz). The trend in the graphs of dielectric loss and dielectric constant are related to the grain size and sintering conditions. When the $Bi_2Mn_xCo_{2-x}O_6$ samples were air sintered, (the first sintering at around 800 ℃), it resulted in increase in grain size with the increasing content of Mn in the $BiCoO_3$ compound. The reason is that Bi_2O_3 and Co_2O_3 both have low-melting point at 825 ℃ and 895 ℃, respectively and during sintering; the liquid phase must have been generated. In the solid-state reactions, the liquid phase helps in rearranging the oxide particles and leads to increase in the chemical potential at the contact site between oxide particles. Furthermore, this encourages mass transportation which eventually has a contribution in the growth of grain sizes.[11] However, the second stage sintering at 850 ℃ was carried out to control the grain size. Since the actual grain size could not be found out in this work, so it can be understood from these graphs that the grain size of the $Bi_2Mn_xCo_{2-x}O_6$ samples was average and not very large but could be smaller. Because the switch ability of domains is lesser in smaller grain size than the large grain size and the smaller grain size and intergrain pores increase the surface area of charge layer creating a charge accumulation in that space which finally resulted in lower dielectric constant.[12] Therefore, $Bi_2Mn_xCo_{2-x}O_6$ samples were observed to have low dielectric constant and dielectric loss. Also, in case of x=0.6, x=0.9 and x=1.0 the slightly higher dielectric loss and dielectric constant and at x=1.7 highest dielectric loss and dielectric constant at 750 ℃ temperature among other compositions could be assigned to the reason of hopping of electron among the transition metal ions and creating secondary phases such as $Bi_{12}MnO_{20}$ in x=0.6 and x=1.0 and $Bi_2Mn_4O_{10}$ in x=1.7 with the transformation of crystal structure from tetragonal to cubic and orthorhombic as confirmed by Rietveld analysis in the section (4.1).

The dielectric constants and dielectric loss for $Bi_2Mn_xCo_{2-x}O_6$ perovskite with respect to frequency at 750 ^{0}C temperature is shown in Figure (4.12) and (4.13). It can be seen that real and imaginary dielectric constant decreased with the increasing content of Mn in the $BiCoO_3$ perovskite.

The difference in peaks in the compounds with x=0.6, x=1.0 and x=1.7 are in the agreement of dielectric loss and dielectric permeability data. Moreover, the results show that the dielectric constant and dielectric loss of the combination at 1kHz was large when x= 1.7 and x=1.0. This also can be attributed to the reason same as for dielectric constant that smaller grain sizes and inter-grain pores increase the surface area of charge layer creating a charge accumulation in that space which finally resulted in lower real dielectric constant.[12]

4.3 Magnetic moment measurements

The calculated results of effective magnetic moment (μ_{eff})of the $Bi_2Mn_xCo_{2-x}O_6$ combination described in relationship of values of x have shown in Figure (4.14).

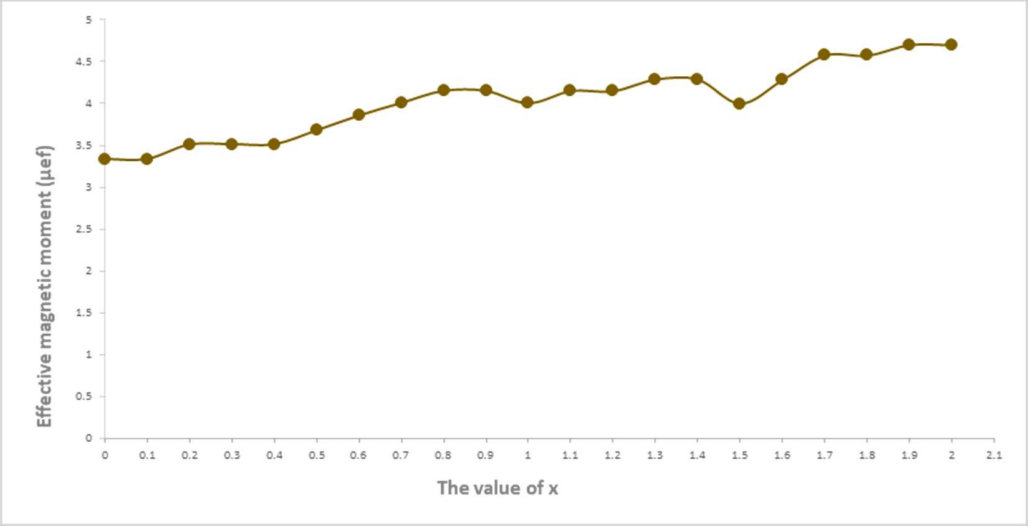

Figure 4.14: Effective magnetic moment (μ_{eff}) of $Bi_2Mn_xCo_{2-x}O_6$ perovskite.

The curve in Figure (4.14) showed the effective magnetic moment was of x=0.0 of 3.3 (μ_{eff}) and increase to up to 4.5 (μ_{eff}) which are in the agreement of the result in the report Mandal *et al*.[10] It is clear from the graph in figure (4.14) that the $Bi_2Mn_xCo_{2-x}O_6$ compound is not antiferromagnetic and become ferromagnetic with the increasing content of Mn. The reason of being ferromagnetic at room temperature can be attributed to the volatile nature of Bi and the involvement of high temperatures in sintering which make the presence of oxygen vacancies almost predictable in Bi based compounds.[15,16] The Co naturally shows high oxygen vacancies concentration which decomposes easily at higher temperatures around 700 K and higher pressure synthesis.[8,17] Since, the ambient pressure was used in the synthesis of $Bi_2Mn_xCo_{2-x}O_6$ compound so oxygen vacancies must be occupied at the specific lattice positions which can induce the stabilization of full antiferromagnetic, super-tetragonal and ferromagnetic monoclinic polar phases, depending on the lattice strain. Therefore, phase competition is enriched, and magnetic properties improved further.[14] And in this case, the presence of multiple phases as confirmed by the XRD analysis can be the reason of ferromagnetic behaviour in $Bi_2Mn_xCo_{2-x}O_6$ compound.

References

[1] N. Rangavittal, T. N. Guru Row, and C. N. R. Rao, *European Journal of Solid State and Inorganic Chemistry*.,1994, **31**, 409-422.

[2] G. Will, N. Masciocchi, W. Parrish and M. Hart, *Journal of Applied Crystallography*., 1987, **20**, 394- 401.

[3] U.Delicat, S.F.Radaev, M.Trömel, P.Behrens, Y.F.Kargin, and A.A.Mar'in, *Journal of SolidState Chemistry*., 1994, **110**, 66-69.

[4] P.L. Meena, R. Kumar, and K. Sreenivas. Phys. Chem. Math. Sci.,2014, **3**, 7-17.

[5] G.Gattow, and H. Schroder, *ZeitschriftfuerAnorganische und Allgemeine Chemie*., 1950, **318**, 176-189.

[6] M. Burianek, T. F. Krenzel, M. Schmittner, J. Schreuer, R. X. Fischer, M. Mühlberg, G. Nénert, H. Schneider, and T. M. Gesing, *International Journal of Materials Research*., 2012, **103**, 449-455.

[7] T. Ramachandran, N. E. Rajeevan, and P. P. Pradyumnan, Materials Sciences and Applications., 2013, **4**, 816- 821.

[8] A. A. Belik, S. Iikubo, K. Kodama, N. Igawa, S. Shamoto, S. Niitaka, M. Azuma, Y. Shimakawa, M. Takano, F. Izumi, and E. T. Muromachi, *Chemistry of materials*., 2006, **18**, 798–803.

[9] Q. Zhang, C. Kim, Y. Jang, H. Hwang, and J. Cho, *Applied Physics Letters*., 2010, **96**, 152901(1-3).

[10] P. Mandal, A. Iyo, Y. Tanaka, A. Sundaresan, and C. N. R. Rao, *J. Mater. Chem*., 2010, **20**, 1646–1650.

[11] Z. Liu,H. Hao, Z. Luo, C. Chen, Z. Yao, M. Cao, and H. Liu, *Journal of Materials Research*., 2021, **36**, 1037-1047.

[12] N. Buatip, N. Promsawat, N. Pisitpipathsin, O. Namsar, P. Pawasri, K.Ounsung, K. Phabsimma, S. T. Rattanachan, P. Janphuang, and S. Projprapai, *Integrated Ferroelectrics*., 2018, **187**, 45-52.

[13] M. -Q. Cai et al, *J. Chem. Phys*., 2007, **126**, 154708(1-6).

[14] C. Menéndez, D. Chu, and C. Cazorla, *NPJ Computational Materials*., 2020, **6**, 76(1-9).

[15] R. Das, S. Sharma, and K. Mandal, *Journal of Magnetism and Magnetic Materials*., 2016, **401**,129-137.

[16] H. Hojo, K. Oka, K. Shimizu, H. Yamamoto, R. Kawabe, and M. Azuma, *Adv. Mater*., 2018, **30**, 1705665(1-15).

[17] K. Oka, M. Azuma, W. Chen, H. Yusa, A. A. Belik, E. T. Muromachi, M. Mizumaki, N. Ishimatsu, N. Hiraoka, M. Tsujimoto, M. G. Tucker, J. P. Attfield, and Y. Shimakawa, *J. AM. CHEM. SOC*., 2010, **132**, 9438–9443.

5. The Bismuth-Manganese-Zinc oxide system

5.1 Rietveld Analysis

X-ray powder diffraction was conducted by the method mentioned in chapter 3 and performed for $Bi_2Mn_xZn_{2-x}O_6$ materials with the values x=0.0 to 2.2. The powder diffraction results were further refined by the Topas academic software which has shown the crystal properties of each composition. The XRD analysis for $Bi_2Mn_xZn_{2-x}O_6$ materials for the values x=0.0 to 2.0 has been shown in Figure (5.1).

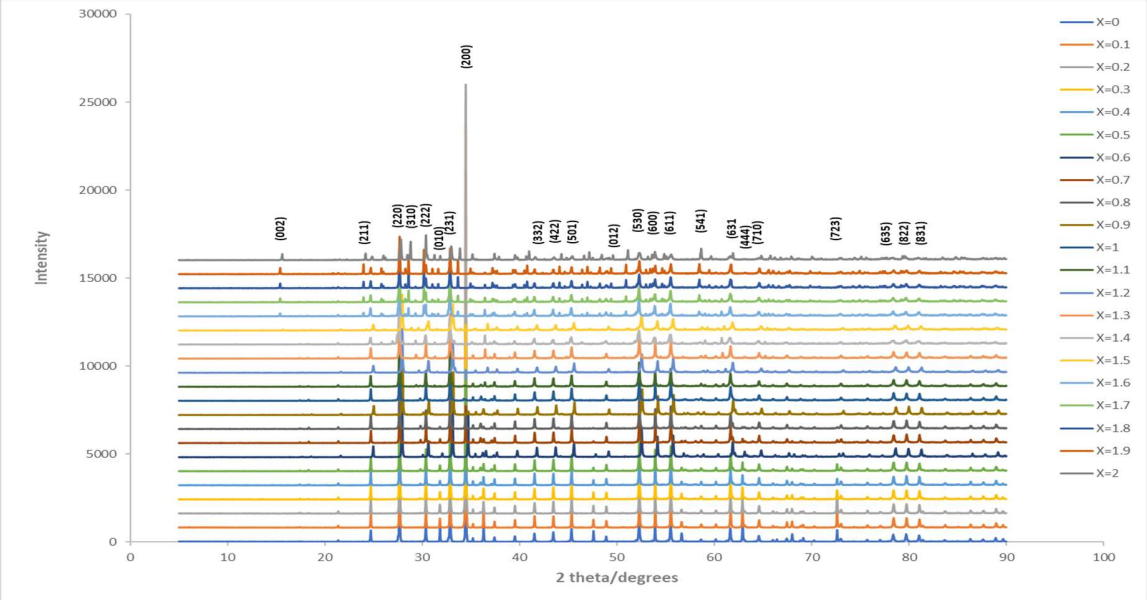

Figure 5.1: XRD results of $Bi_2Mn_xZn_{2-x}O_6$ for x= 0.0 to 2.0.

It can be seen that the structure is highly distorted due to co-doping of Zn and Mn in Bi-based systems. The addition of Mn in the $BiZnO_3$ resulted in the formation of many variants and it was difficult to achieve a single phase of any composition. The intense peaks such as (020), (200) and (012) observed in the XRD pattern showed that material is highly crystalline in nature. The peaks confirmed the presence of tetragonal and orthorhombic crystal structure (space

group; I23 and pbam) and is in agreement with the results obtained in the report by Hanet *et al*.[1] The presence of multiphases in all the compositions can be attributed to the kinetic of formations. The divalent Zn ions increase the redundant Bi^{3+} which are the dominant reason. The presence of Mn and Zn ions together in the system further creates a distorted perovskite structure. The addition of Mn creates an orthorhombic crystal structure, and the many secondary phases which is further explained in the figure (5.1). The presence of mixed crystal structures of rhombohedral and tetragonal phases is also reported in the research and can be obtained from the Gd-doped samples.[2] The samples have acentric structure, as reported by previous results.[2]

The XRD patterns confirmed the presence of impurities which could not be fully identified. But refinement has shown some of the information about their classifications which are shown in Table (5.1) and (5.2) and Figure (5.2) to (5.5).

Table 5.1: Characteristics and properties of the obtained data from the structure refinement by Topas Academic software of $Bi_2Mn_xZn_{2-x}O_6$ when x=1.1 and x=1.2.

The value of x	**1.1**			**1.2**	
Rwp	15.96%			15.25%	
Properties	$Bi_{12}ZnO_{20}$ [3]	$ZnMn_2O_4$ [4]	Mn_3O_4 [5]	$ZnMn_2O_4$ [4]	$Bi_{12}(Bi_{0.67}Zn_{0.33})O_{19.33}$ [6]
a	10.202	5.724	5.784	5.725	10.208
b					
c		9.217	9.421	9.228	
α=β=γ	90^0				
Space group	I23	141/amdS	141/amdZ	141/amd	I23
Cell volume	1061.839	301.964	315.176	302.452	1063.635
Number of equivalent positions	24	32		32	24
Number of independent parameters	24			19	

Table 5.2: Characteristics and properties of the obtained data from the structure refinement by Topas Academic software of $Bi_2Mn_xZn_{2-x}O_6$ when x=1.9 and x=2.0.

The value of x	1.9			2.0	
Rwp	17.34%			16.65%	
Properties	$Bi_{23}Zn_{1.64}O_{36}$ [7]	$Bi_2Mn_4O_{10}$ [8]	Mn_3O_4 [9]	$Bi_{12}MnO_{20}$ [10]	$Bi_2Mn_4O_{10}$ [8]
a	10.188	7.548	9.503	10.236	7.561
b		8.527	9.797		8.541
c		5.756	3.044		5.766
α=β=γ	90^0				
Space group	I23	Pmab	Pmab	I23	Pbam
Cell volume	1057.417	370.488	283.416	1072.377	372.398
Number of equivalent positions	24	32		24	8
Number of independent parameters	24			19	

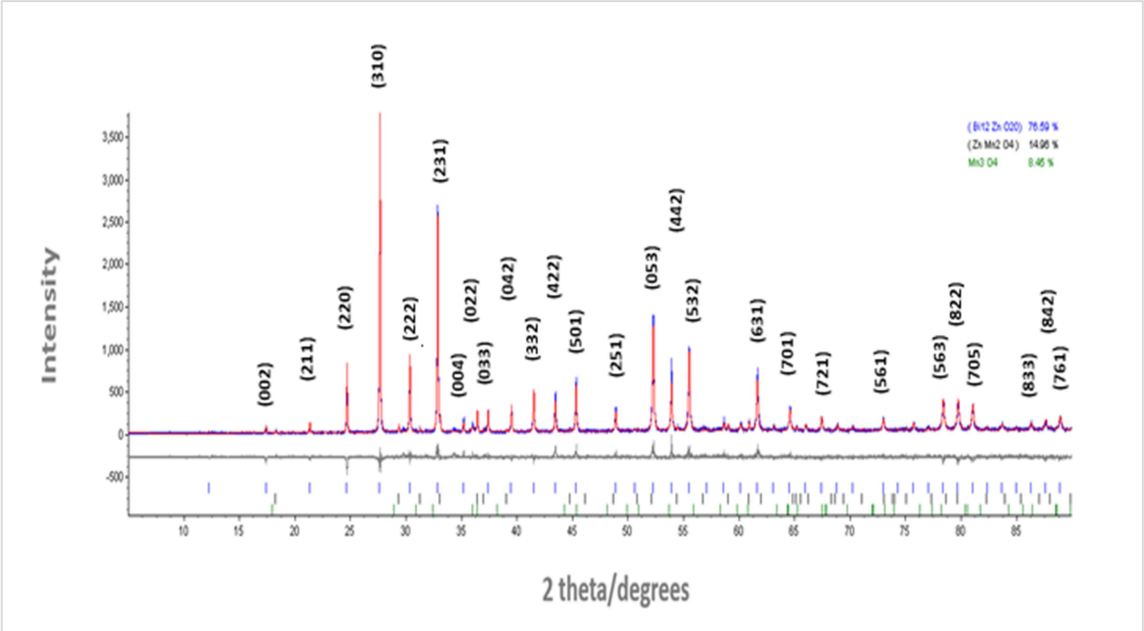

Figure 5.2: X-ray powder diffraction pattern Rietveld fit for $Bi_2Mn_{1.1}Zn_{0.9}O_6$ (x=1.1).

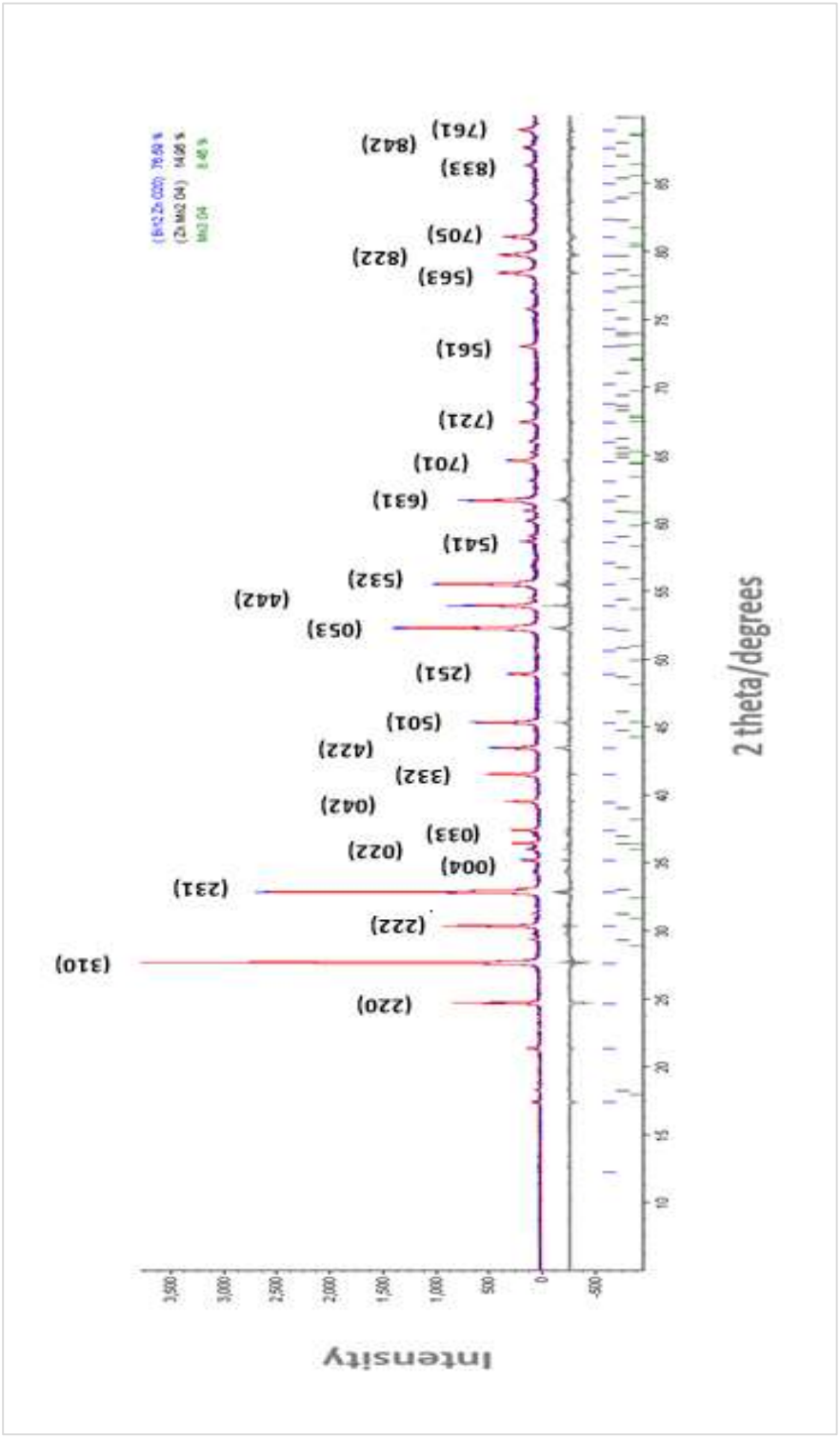

Figure 5.3: X-ray powder diffraction pattern Rietveld fit for $Bi_2Mn_{1.2}Zn_{0.8}O_6$ (x=1.2).

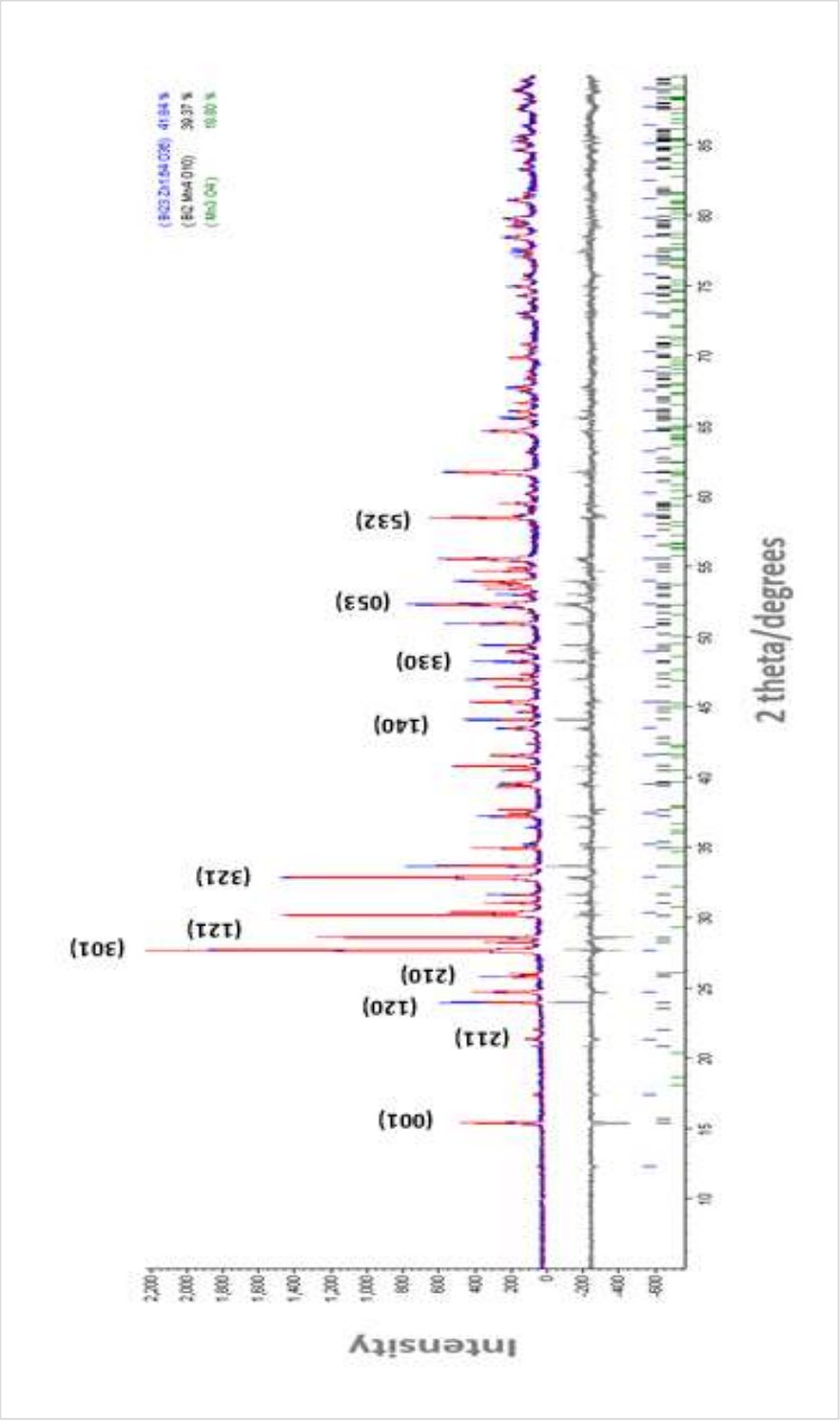

Figure 5.4: X-ray powder diffraction pattern Rietveld fit for $Bi_2Mn_{1.9}Zn_{0.1}O_6$ (x=1.9).

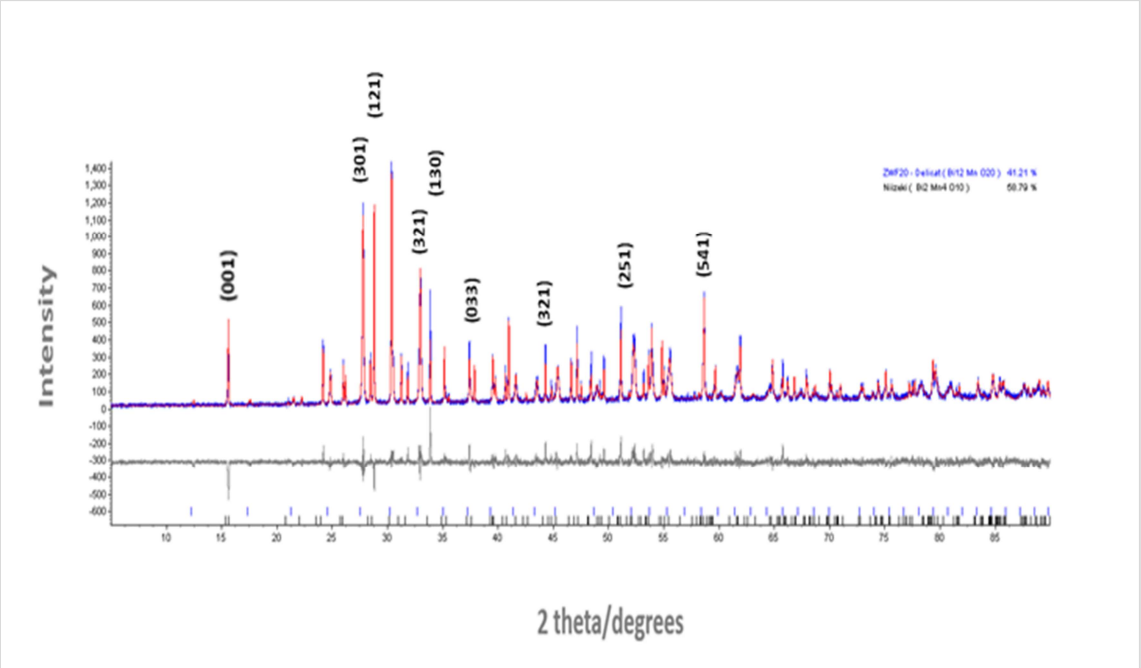

Figure 5.5: X-ray powder diffraction pattern Rietveld fit for $Bi_2Mn_2Zn_{0.0}O_6$ (x=2.0).

The refinement of $Bi_2Mn_xZn_{2-x}O_6$ materials for x=1.1, 1.2, 1.9 and 2.0 in the figure (5.2) to (5.5). The addition of Mn has shown systematic variation in structure parameters of samples of group Pbam and the value of b increases with the Mn addition which confirms the presence of orthorhombic structure. The cell volume decreased with the increase in Mn content, and this indicate that the average crystal sizes are $\mathrm{Mn} = 0.645\,\text{Å}$, and Zn=0.750 Å and the average ionic radii mismatch from the unit cell is therefore dominate over the crystallite size and cell volume. The decrease in volume cell can also be attributed the reason that dopant acts as inhibitors center for crystal size growth.[1,11]

5.2 Dielectric measurement

The graphs of capacitance (pF), conductance (μS), and AC conductivity (μS/cm) with respect to the value of x at 750 ℃ at different frequencies 1000 Hz, 10000 Hz and 100000 Hz of $Bi_2Mn_xZn_{2-x}O_6$ perovskite was listed in Table (5.3) and

(5.4), also has shown in Figures (5.6), (5,7) and (5.8). It can be seen that capacitance (pF), conductance (μS) and conductivity (μS/cm) increased with the increase in Mn content in $BiZnO_3$ and also with the frequency. This can be said that the $Bi_2Mn_xZn_{2-x}O_6$ material has better conductive properties with the Mn addition and shows good semiconductor nature.[12]

Table 5.3: The dielectric results of the $Bi_2Mn_xZn_{2-x}O_6$ combination.

Value of x	Capacitance			Conductance			Conductivity (S/m)		
	1 kHz	10 kHz	100 kHz	1 kHz	10 kHz	100 kHz	1 kHz	10 kHz	100 kHz
	C (pF)	C (pF)	C (pF)	G (μS)	G (μS)	G (μS)			
0.0	52.34	50.42	48.00	0.10	0.07	0.98	$6.78x10^{-7}$	$4.75X10^{-7}$	$6.64X10^{-6}$
0.1	34.20	31.18	29.92	0.02	0.06	0.61	$1.28 x10^{-7}$	$3.84X10^{-7}$	$3.91X10^{-6}$
0.2	20.05	19.40	17.98	0.003	0.04	0.48	$2.15 x10^{-8}$	$2.87X10^{-7}$	$3.44X10^{-6}$
0.3	28.40	25.70	23.47	0.01	0.10	0.88	$7.44 x10^{-8}$	$7.44X10^{-7}$	$6.55X10^{-6}$
0.4	46.60	40.78	36.10	0.03	0.23	1.80	$2.17X10^{-7}$	$1.67X10^{-6}$	$1.3X10^{-5}$
0.5	40.14	33.21	28.41	0.04	0.26	1.70	$2.88X10^{-7}$	$1.87X10^{-6}$	$1.23X10^{-5}$
0.6	54.38	44.68	37.31	0.04	0.38	2.54	$2.80X10^{-7}$	$2.48X10^{-6}$	$1.66X10^{-5}$
0.7	42.37	33.61	27.50	0.04	0.32	2.01	$3.36X10^{-7}$	2.5X10-6	$1.57X10^{-5}$
0.8	58.87	44.75	35.78	0.07	0.50	2.87	$5.24X10^{-7}$	$3.74X10^{-6}$	$2.15X10^{-5}$
0.9	71.50	51.38	39.31	0.10	0.70	3.77	$7.17X10^{-7}$	$5.02X10^{-6}$	$2.7X10^{-5}$
1.0	91.25	64.43	49.42	0.14	0.89	4.50	$8.77X10^{-7}$	$5.74X10^{-6}$	$2.9X10^{-5}$
1.1	99.51	64.73	47.06	0.18	1.12	5.55	$1.31X10^{-6}$	$8.19X10^{-6}$	$4.06X10^{-5}$
1.2	76.35	48.54	35.08	0.18	0.88	4.00	$1.34X10^{-6}$	$6.53X10^{-6}$	$2.97X10^{-5}$
1.3	90.66	58.35	42.57	0.21	1.05	4.58	$1.45X10^{-6}$	$7.24X10^{-6}$	$3.16X10^{-5}$
1.4	92.27	57.42	42.02	0.21	1.08	3.85	$1.41X10^{-6}$	$7.25X10^{-6}$	$2.58X10^{-5}$
1.5	86.30	51.82	39.32	0.22	1.00	3.11	$1.60X10^{-6}$	$7.25X10^{-6}$	$2.26X10^{-5}$
1.6	79.62	50.52	39.27	0.20	0.87	2.90	$1.51X10^{-6}$	$6.57X10^{-6}$	$2.19X10^{-5}$
1.7	87.25	58.21	46.9	0.21	0.88	2.90	$1.55X10^{-6}$	$6.48X10^{-6}$	$2.14X10^{-5}$
1.8	80.71	57.05	46.97	0.19	0.70	2.72	$1.41X10^{-6}$	$5.18X10^{-6}$	$2.01X10^{-5}$
1.9	99.41	78.15	63.23	0.20	0.83	4.57	$1.54X10^{-6}$	$6.41X10^{-6}$	$3.53X10^{-5}$
2.0	96.14	63.58	45.09	0.32	1.12	6.48	$2.30X10^{-6}$	$8.06X10^{-6}$	$4.66X10^{-5}$

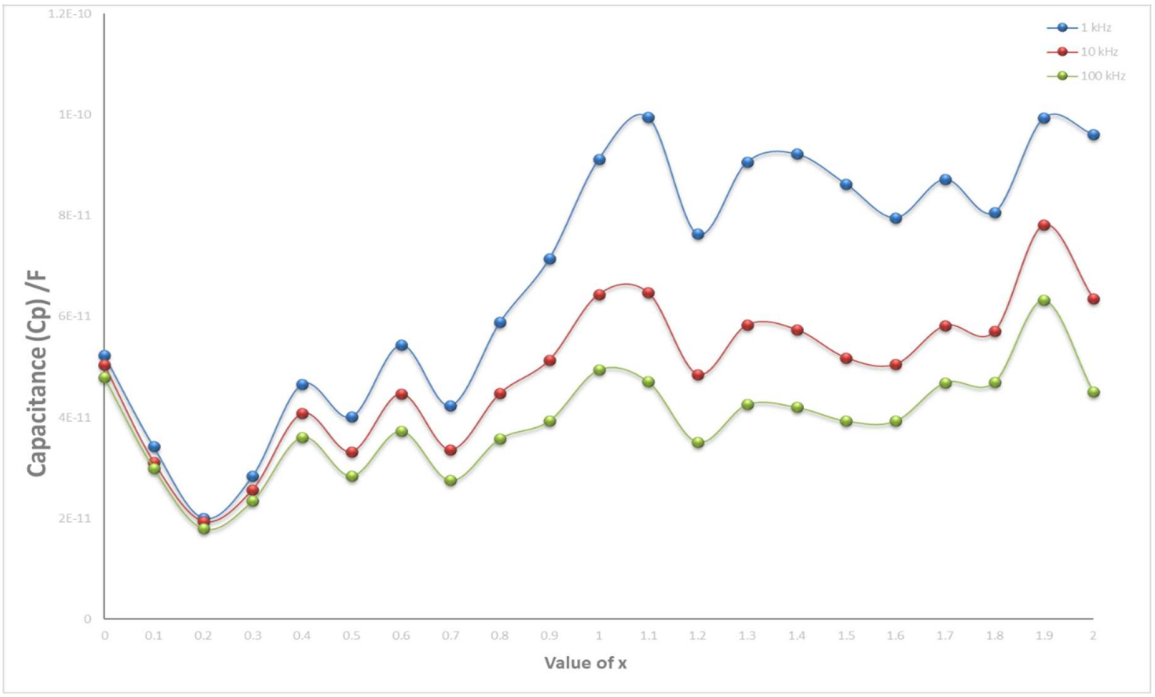

Figure 5.6: The capacitance of $Bi_2Mn_xZn_{2-x}O_6$.

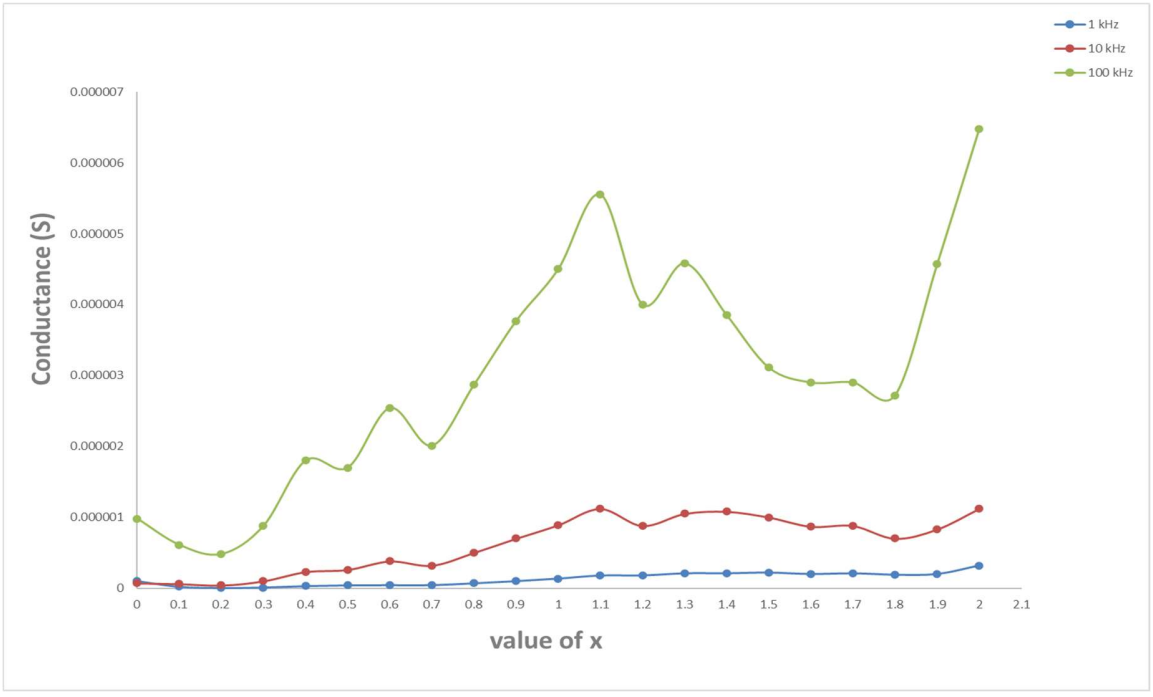

Figure 5.7: The conductance of $Bi_2Mn_xZn_{2-x}O_6$.

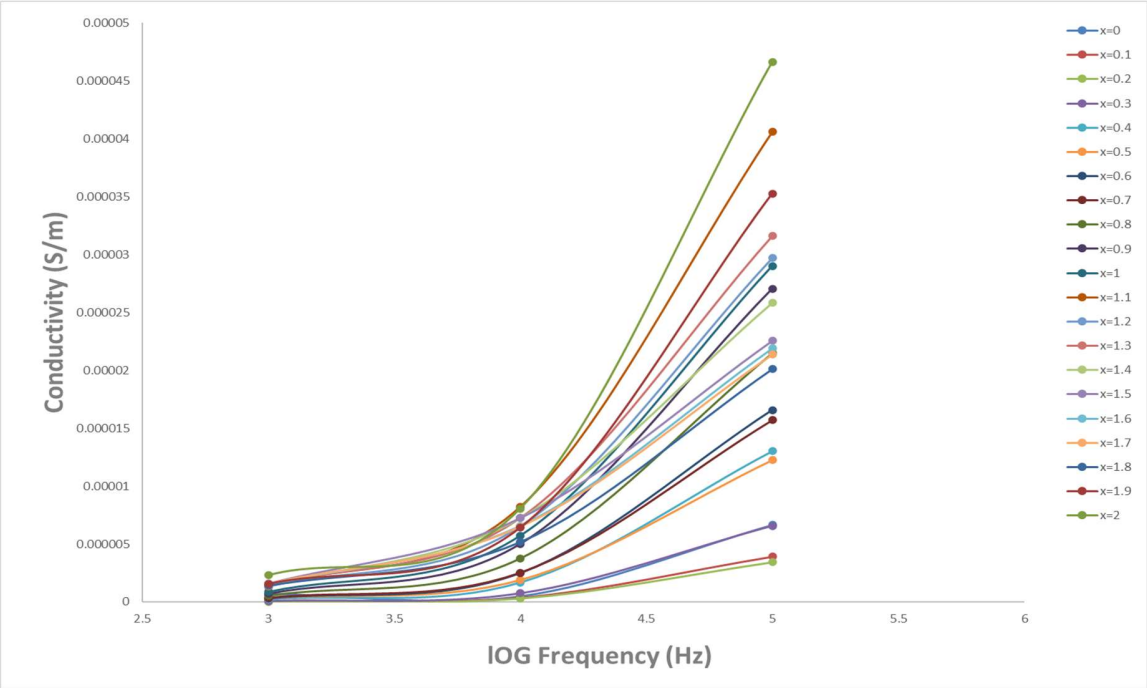

Figure 5.8: The electrical conductivity $Bi_2Mn_xZn_{2-x}O_6$.

The lower values of capacitance (pF), conductance (μS) and conductivity (μS/cm) at lower frequency show that transportation of charge carriers for long paths require less energy in the lower frequency part in the lower frequency region therefore it has better conductivity. However, the orientation mechanism or relaxation uniformly takes place by releasing high energy.[13] The flexible oxygen vacancies and the cations presence around the grain boundaries is the reason of high activation energy in the high-temperature zones.[14]

Furthermore, the multiferroic materials has microstructure composed of grains, grain boundaries and structural defects like impurity or porosity, and the martials generally shows high resistivity at low frequency because of contributions of grain boundaries to resistance and show low resistivity at high frequency because of grains offering resistance. In this way, high resistance showed by perovskite results in difficult in electron flow inside the material and therefore, comparatively heavy energy amount is required for electronic

exchange between $Mn^{3+} \Leftrightarrow Mn^{4+}$ions when added in the $BiZnO_3$ perovskite which ultimately show dielectric loss at lower frequency in the material. At the same time as, at higher frequencies which is actually a low resistivity area, less energy is required for electron transfer between the crystallographically equivalent, but the presence of various valent ions of Mn at the same lattice sites results in low dielectric loss in the perovskite materials. The conducting properties analysis was in agreement with the results of dielectric properties of $Bi_2Mn_xZn_{2-x}O_6$ perovskite.[15]

The dielectric constant of $Bi_2Mn_xZn_{2-x}O_6$ composition with respect to the values of x at different frequencies 1000 Hz, 10000 Hz and 100000 Hz at temperature 750 ℃ has shown in Figure (5.9).

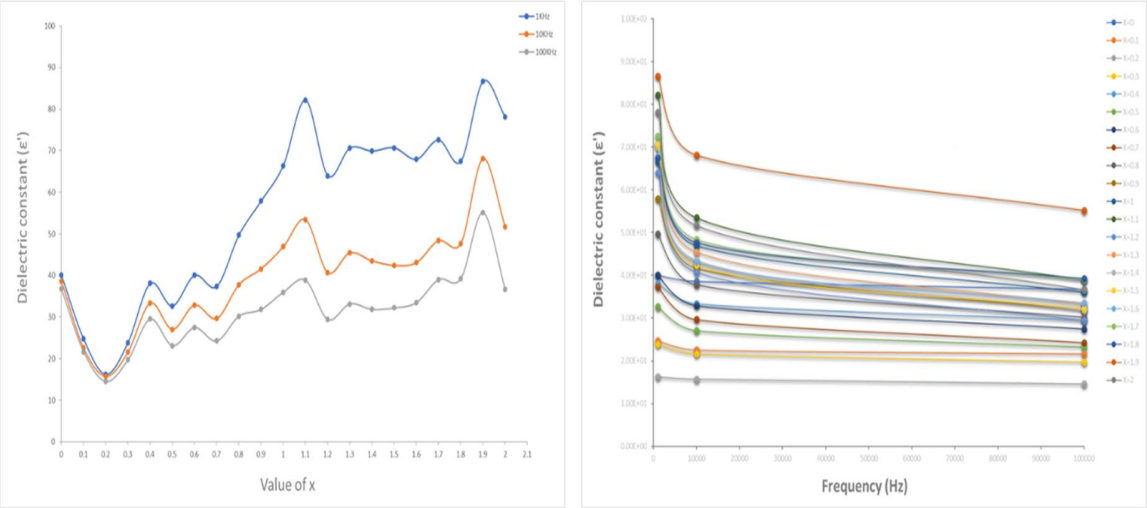

Figure 5.9: The dielectric constant $Bi_2Mn_xZn_{2-x}O_6$.

The graph clearly shows that the dielectric constant is increasing with the increasing content of Mn but it is decreasing with the frequency, such that highest frequency has lowest dielectric constant value for every composition and when x is above 0.3, there is an evidence of dielectric relaxation mechanism occurring as can be seen in figure (5.9).

This trend is associated with Maxwell–Wagner[16] pattern of interfacial polarization and can be further understood with Koop's macroscopic theory.[17] The larger values of dielectric constant at lower frequency indicate the homogeneous dielectric structure which further explains the space charge polarization. In this case, the motion of domain walls is influenced by in-homogeneities such as pores, grain structure. The higher polarization values and higher charge mobility are the reason of high dielectric constant. In $Bi_2Mn_xZn_{2-x}O_6$ composition, the interfacial polarization becomes notable due to high value of dielectric constant at lower frequency in the in the perovskite, while in the region of higher frequency, the contribution of electronic polarization dominated. And the occurrence of dielectric relaxation may be because of the thermal activation, intrinsic defects growth, and oxygen vacancies during chemical reaction at high temperature, and because of the increase in conductivity at higher temperature or frequency.[18]

The dielectric loss of $Bi_2Mn_xZn_{2-x}O_6$ perovskite with the varying x values at temperature 750 ℃ with different frequencies 1000 Hz, 10000 Hz and 100000 Hz has been shown in Figure (5.10).

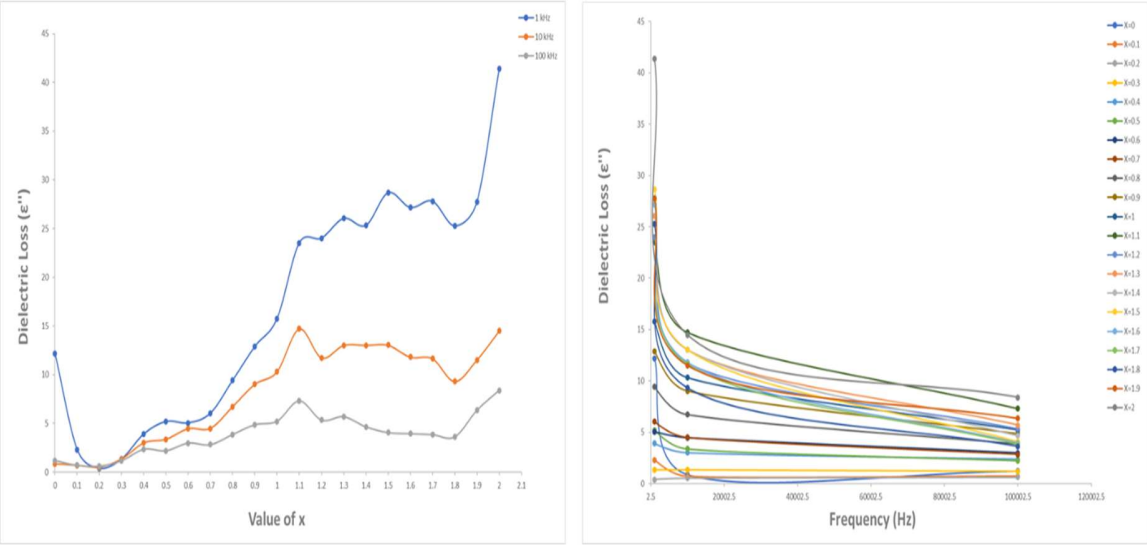

Figure 5.10: The dielectric loss $Bi_2Mn_xZn_{2-x}O_6$.

The trend observed in this graph is similar to what observed in the dielectric constant with the frequencies and increasing value of Zn. This type of behavior of dielectric loss can also be explained by Maxwell–Wagner's (2-layermodels) theory.[16] According to this model, the grains of $Bi_2Mn_xZn_{2-x}O_6$ perovskite have conducting behavior while the grain boundaries between the layers of atoms have poor conducting properties. Near the grain boundaries, the more energetic electrons are likely to be found in the entire electric-conduction region with the decreasing frequency. But in the region of higher frequencies, the more energetic electrons are likely to be found at the grains and therefore, the value of resistance increases at the region close to the grain boundaries. Hence, there will be less amount of energy required by the electrons for charge transferring in the high-frequency areas. But this required amount of energy will be high in the low-frequency regions. It can also be seen in the graph that some values have slightly higher dielectric loss and dielectric constant such as x=1.1 and 1.9, this increment can be due to the factors like 1) charge carriers scattering which are thermally active and 2) oxygen vacancies presence at higher temperatures and intrinsic defects.[12]

The real and imagery dielectric constant with the change in frequency at temperature 750 ℃ of $Bi_2Mn_xZn_{2-x}O_6$ perovskite with different x value. In these graphs, it can be seen that the values of ε' and ε'' are decreasing with the increase in frequency. This pattern can be attributed to the dispersion which is increasing with the frequency and the values of ε' and ε'' decreasing and eventually become constant or decreasing very slowly.[15]

In general, the dielectric dispersion can be described by four basic polarization phenomena present in the material which are electronic, ionic, dipolar and interfacial polarizations.[15] When the electric field is applied, the electronic cloud displacement in an atom related to nuclei results in electronic polarization and the inter-ionic separation formed by ionic bonds between negative and positive

ions is increased and resulted in ionic polarization. The occurrence of these two polarizations is normally at higher frequencies (at GHz/THz). Likewise, the orientation of dipoles has tendency to increase in the field direction and results in dipolar polarization while the charge accumulation at the electrode interfaces or at the inter-phase interface (in case of multiphase materials) results in interfacial polarization. However, in this study, the selected frequency range was between 1 kHz to 100 kHz and the perovskite developed with fine grained microstructure with thin grain boundaries and the likely to have possible coexistence of more interfaces. The dipolar and interfacial mechanisms have the main contribution in the dielectric polarization in the perovskite material.

When the Mn is added in the $BiZnO_3$ structure, the dispersion was observed to be increased with the increasing Mn content as the ε' and ε'' are higher in lower frequencies. There is likely to have existence of Mn in divalent and trivalent states when the bismuth ions were replaced by manganese ions in $Bi_2Mn_xZn_{2-x}O_6$ perovskite because of the stoichiometric imbalance in the synthesis and a corresponding electronic exchanges like $Mn^{3+} \Leftrightarrow Mn^{4+}$ ions leads to localized charge carriers displacement towards the interface and inducing dipole moment by dipolar polarization. This has a major contribution in increasing dielectric constant at lower frequency. Furthermore, as the inhomogeneous microstructures of grains and grain boundaries in these materials are considered, therefore the dielectric behavior can also be associated with the contribution related to space charge polarization.[19]

5.3 Magnetic moment measurements

The magnetic moment (μB) results with respect to the value of x at room temperature of $Bi_2Mn_xZn_{2-x}O_6$ perovskite has been shown in Figure (5.11).

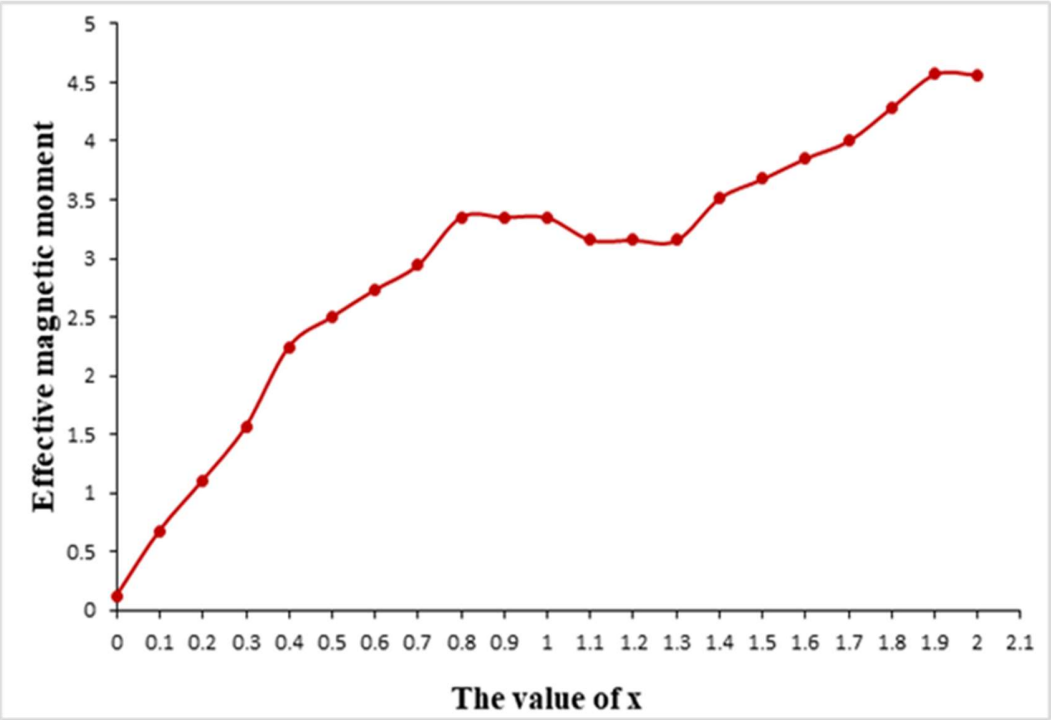

Figure 5.11: The effective magnetic moment of $Bi_2Mn_xZn_{2-x}O_6$.

It can be seen that values of magnetic moment increase with the increase in manganese content. This is due to that fact that when the Mn is added, it creates a distortion in the spiral spin structure and decreases the crystallite size. This distortion results in the conversion of helical structure to linear structure and thereby resulted in improved magnetic properties.[20,21] The μ_{eff}= 0.124 μB obtained for $BiZnO_3$ for the composition x=0.0 which increase to μ_{eff}= 4.5667 μB when x=2.0 for $BiMnO_3$. There are four ferromagnetic and two antiferromagnetic interactions for every Mn cation as reported by Chiba et al and Syono *et al*.[22,23] it can understood that the ferromagnetic interactions overcome the antiferromagnetic interactions at temperature less than critical temperature (room temperature), and as a result the ferromagnetism of $BiMnO_3$ appeared.[22,23]

$BiMnO_3$ is insulator in nature and this is possibly be related to the Mn-O-Mn bond angles which are normally from 160^0 to 140^0. When the bismuth cations partly be

replaced by Mn cations, the electrical resistivity decreases, but still shows a thermally activated behavior.[22, 23] However, the ferromagnetism disappears quickly and indicates that the double exchange mechanism is not the applicable in these materials; therefore, the ferromagnetism appears by the super exchange interactions in the orbital ordered states.[24]

5.4 UV-vis Spectroscopy

The results of UV-vis spectroscopy were obtained using the same technical and steps mentioned in chapter 3 to detect absorption of the $Bi_2Mn_xZn_{2-x}O_6$ compound. The UV-vis spectroscopy showed the potential volatility of the crystalline structure and the local atomic arrangement of the compound $Bi_2Mn_xZn_{2-x}O_6$. The observed data are illustrated in Figure (5.12). The absorbance curve of $Bi_2Mn_xZn_{2-x}O_6$derived from Kubelka-Munk (K–M) function given by $F(R)=\frac{(1-R)^2}{2R}$,[25] in which R is defined as reflectance value.

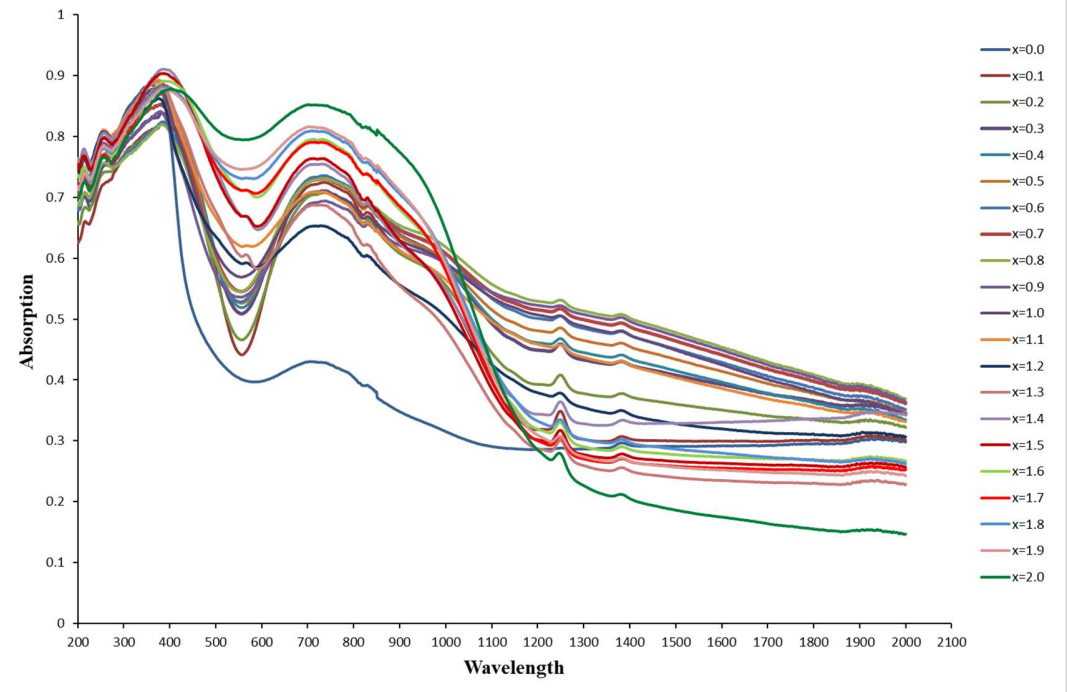

Figure 5.12: The UV-vis data of $Bi_2Mn_xZn_{2-x}O_6$.

The peaks trends observed in all the samples were as: the peaks of samples with x=0.0 to x=0.9 has absorbance edge shifting towards higher wavelength from 400-700nm which is called read shift. And then the samples with x=1.0 to x=2.0 has absorbance shifting towards lower wavelength from 400-700nm which is called blue shift. The red shift indicates the doping concentration is decreasing the band gap.[26,27] This can also be attributed to the dispersion of the size of nanoparticles in the samples.[28] The blue shift indicates that the further addition of doping concentration in Bi^{3+} ions showed excitonic absorptions with the increase in dopant because the lattice constant decreased with the doping concentration,[29] there may be many factors which reduces the band gap such as microstructures,[30] chemical structures and structural defects.[31,32] The doping of metal ion is a promising method to produce visible-light driven photo catalysts. Impurity levels can be created in the forbidden band through metal ion doping. Now, the band gap reduction can be occurred either an acceptor level at the bottom of original conduction band or by a donor level at the top of original valence band.[33] Oxygen vacancies also have tendency to reduce the band gap. As reported by Zhang *et al*.[34] The substitution of Na^{1+} ion in Bi based perovskite resulted in positioning of hole as an acceptor band above the valence band and the oxygen vacancy impurity band below the conduction band. The broadening of hole acceptor band with the increase in Na^{1+} content and the oxygen vacancies reduction can all be the reason of reduced band gap.

References

[1] Y. Han, Y. Ma, C. Quan, N. Gao, Q. Zhang, W. Mao, J. Zhang, J. Yang, X. a. Li and W. Huang, *Ceramics International*, 2015, **41**, 2476-2483.

[2] W. Hu, Y. Chen, H. Yuan, G. Li, Y. Qiao, Y. Qin and S. Feng, *Journal of Physical Chemistry C*, 2011, **115**, 8869-8875.

[3] S. Kirik, V. Kutvitskii and T. Koryagina, *Zh. Strukt. Khim.*, 1985, **26**, 90-95.

[4] M. NOGUES and P. POIX, 1972.

[5] D. Jarosch, *Mineralogy and petrology*, 1987, **37**, 15-23.

[6] S. Radaev, L. Muradyan, Y. F. Kargin, V. Volkov, V. Sarin, E. Rider and V. Simonov, *Kristallografiya*, 1990, **35**, 1126-1132.

[7] T. Mel'nikova, G. Kuz'micheva, N. Bolotina, V. Rybakov, Y. V. Zubavichus, N. Sadovskaya and E. Mar'ina, *Crystallography Reports*, 2014, **59**, 353-361.

[8] N. Niizeki and M. Wachi, *ZeitschriftfürKristallographie-Crystalline Materials*, 1968, **127**, 173-187.

[9] C. R. Ross, D. C. Rubie and E. Paris, *American Mineralogist*, 1990, **75**, 1249-252.

[10] U. Delicat, S.F.Radaev, M.Troemel, P. Behrens, Yu.F.Kargin andA.A Marin,*Journal of Solid State Chemistry.*, 1994,**110**, 66-69.

[11] P. Achary, S. K. Dehury and R. Choudhary, *Journal of Materials Science: Materials in Electronics*, 2018, **29**, 6805-6816.

[12] M. Padhy, S. K. Dehury, R. Choudhary and P. Achary, *Applied Physics A*, 2020, **126**, 1-13.

[13] M. A. E.-F. Gabal, Y. M. Al Angari and A. Y. Obaid, *ComptesRendusChimie*, 2013, **16**, 704-711.

[14] A. Belboukhari, E. Choukri, Y. Gagou, R. Elmoznine, N. Abdelmoula, A. Neqali, M. El Marssi, H. Khemakhem and D. Mezzane, *Superlattices and Microstructures*, 2014, **71**, 7-22.

[15] B. Dhanalakshmi, P. Kollu, B. P. Rao and P. S. Rao, *Ceramics International*, 2016, **42**, 2186-2197.

[16] R. P. Pawar and V. Puri, *Ceramics International*, 2014, **40**, 10423-10430.

[17] C. Koops, *Physical review*, 1951, **83**, 121.

[18] S. Khetre, A. Chopade, C. Khilare, H. Jadhav, P. Jagadale and S. Bamane, *Journal of Materials Science: Materials in Electronics*, 2013, **24**, 4361-4366.

[19] C.-W. Nan, M. Bichurin, S. Dong, D. Viehland and G. Srinivasan, *Journal of applied physics*, 2008, **103**, 1.

[20] J.-Z. Huang, Y. Wang, Y. Lin, M. Li and C. Nan, *Journal of Applied Physics*, 2009, **106**, 063911.

[21] S. Basu, S. Hossain, D. Chakravorty and M. Pal, *Current Applied Physics*, 2011, **11**, 976-980.

[22] H. Chiba, T. Atou and Y. Syono, *Journal of Solid State Chemistry*, 1997, **132**, 139-143.

[23] Y. Syono, H. Chiba and T. Atou, *Journal of the Magnetics Society of Japan*, 1998, **22**, S1_52-54.

[24] T. Atou, H. Chiba, K. Ohoyama, Y. Yamaguchi and Y. Syono, *Journal of Solid State Chemistry*, 1999, **145**, 639-642.

[25] P. Kubelka, *Zeitschrift fur technischePhysik*, 1931, **12**, 593-601.

[26] Y. Wang, P. J. Thomas and P. O'Brien, *The Journal of Physical Chemistry B*, 2006, **110**, 21412-21415.

[27] A. Sen, M. K. Hasan, Z. Islam, M. R. Al Hassan, T. Zaman, M. Matin and F. Gulshan, *Materials Research Express*, 2020, **7**, 016312.

[28] H. Shao, X. Bai, H. Cui, G. Pan, P. Jing, S. Qu, J. Zhu, Y. Zhai, B. Dong and H. Song, *Nanoscale*, 2018, **10**, 1023-1029.

[29] S. E. Mousavi Ghahfarokhi, M. Rahimi Larki and I. Kazeminezhad, *IEEE Transactions on Magnetics*, 2020, **56**.

[30] M. Bennett and P. James, *The Green bottom line: environmental accounting for management: current practice and future trends*, Routledge, 2017.

[31] S. Gómez-Salces, F. Aguado, F. Rodríguez, R. Valiente, J. González, R. Haumont and J. Kreisel, *Physical Review B*, 2012, **85**, 144109.

[32] P. S. Mocherla, C. Karthik, R. Ubic, M. Ramachandra Rao and C. Sudakar, *Applied Physics Letters*, 2013, **103**, 022910.

[33] X. Chen, S. Shen, L. Guo and S. S. Mao, *Chemical reviews*, 2010, **110**, 6503-6570.

[34] H. Zhang, W. Liu, P. Wu, X. Hai, M. Guo, X. Xi, J. Gao, X. Wang, F. Guo and X. Xu, *Nanoscale*, 2014, **6**, 10831-10838.

6. The Bismuth-Manganese-nickel oxide system

This chapter discusses the results of $Bi_2Mn_xNi_{2-x}O_6$ prepared by the solid-state synthesis, via two variations namely grinding (experiment 1) conducted by mixing of samples and the other one is ball mill ultra-high intensity grinding (experiment 2). The ball mill has excellent effect on the electrical transport properties of materials due to the impedance of carrier transport in nanostructure.[1] The effect of this variation was analysed through XRD, SEM, Dielectric properties, UV-vis spectroscopy, FT-IR and Magneto moment spectroscopy and the results are compared with both variations.

6.1 Rietveld Analysis

The x-ray powder diffraction analysis conducted has performed for $Bi_2Mn_xNi_{2-x}O_6$ material by the method described in chapter 3, for the values x=0.0 to 2.0, which has been shown in Figure (6.1) and (6.2).

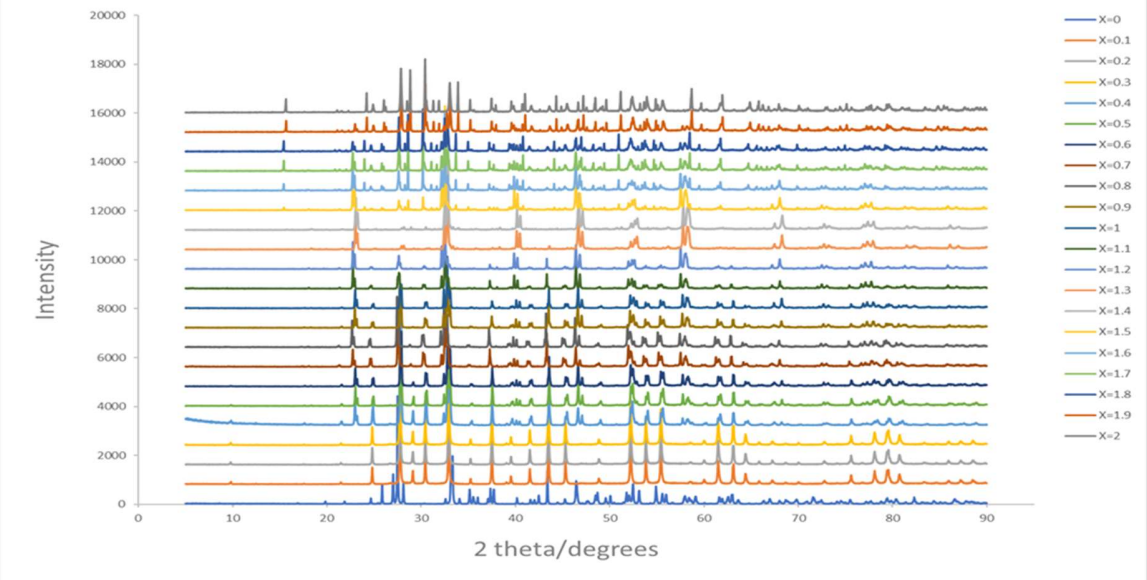

Figure 6.1: XRD results of $Bi_2Mn_xNi_{2-x}O_6$ for x= 0.0 to 2.0 (experiment 1).

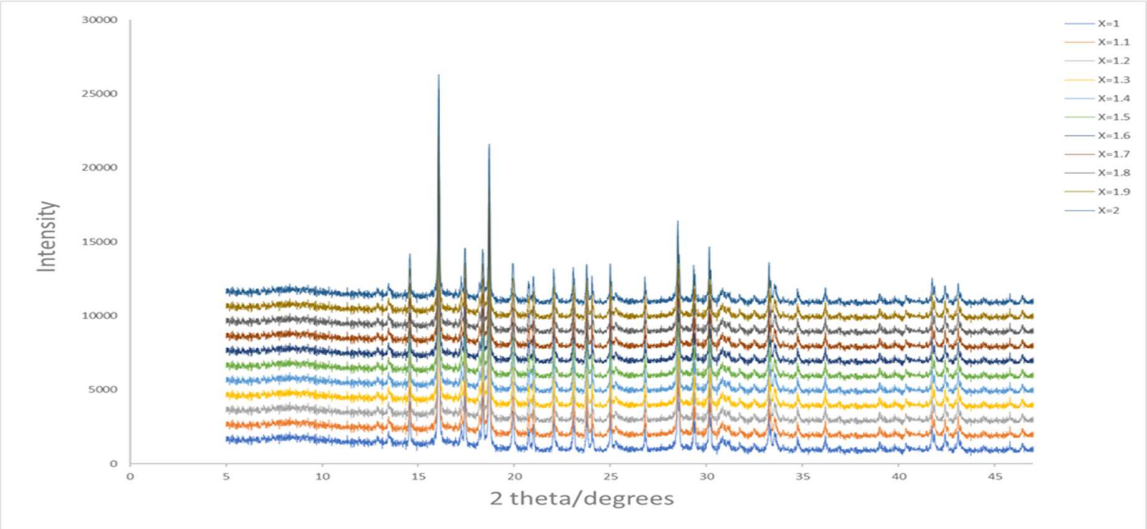

Figure 6.2: XRD results of $Bi_2Mn_xNi_{2-x}O_6$ for x= 1.0 to 2.0 (experiment 2).

The XRD patterns have confirmed the presence of impurities which could not be fully identified. The refinement provides information about their classifications which are shown in Table (6.1), (6.2), (6.3) and (6.4).

Table 6.1: The obtained data from the structure refinement by Topas Academic software of $Bi_2Mn_xNi_{2-x}O_6$ when x=0.0 and x=1.2 from experimental method 1.

The value of x	**0**		**1.2**		
Rwp	22.239%		19.12%		
Properties	NiO^1	$Bi_2O_3{}^2$	$Bi_2Mn_{\frac{4}{3}}Ni_{\frac{2}{3}}O_6{}^3$	$Bi_{12}MnO_{20}{}^4$	NiO^1
a	4.1648	5.835	5.501	10.220	4.179
b		8.134	11.141		
c		7.483	15.526		
α	90^0	90^0	90^0		
β		67.070^0			
γ		90^0			
Space group	Fm3m	P121/c1	Pn21m	I23	Fm3m
Cell volume	72.241	327.105	951.636	1067.400	72.962
Number of equivalent positions	192	4	4		192
Number of independent parameters	19		24		

Table 6.2: Characteristics and properties of the obtained data from the structure refinement by Topas Academic software of $Bi_2Mn_xNi_{2-x}O_6$ when x=1.3 and x=1.4 from experimental method 1.

The value of x	1.3			1.4
Rwp	15.06%			17.54%
Properties	$Bi_2Mn_{\frac{4}{3}}Ni_{\frac{2}{3}}O_6$[3]	$Bi_{12}MnO_{20}$[4]	$Bi_{18}Ni_8O_{36}$[5]	$Bi_2Mn_{\frac{4}{3}}Ni_{\frac{2}{3}}O_6$[3]
a	5.501	10.130	10.219	5.500
b	11.135			11.132
c	15.520			15.517
α=β=γ	90^0			
Space group	Pn21m	I23	I23	Pn21m
Cell volume	950.606	1039.441	1067.262	949.989
Number of equivalent	4	24		4
Number of independent parameters	23			42

Table 6.3: Characteristics and properties of the obtained data from the structure refinement by Topas Academic software of $Bi_2Mn_xNi_{2-x}O_6$ when x=1.2 and x=1.3 from experimental method 2.

The value of x	1.2			1.3		
Rwp	15.03%			11.77%		
Properties	$(Bi_{19.68}Ni_{4.32})Ni_2O_{40}$[6]	$Mn(NiMn)O_4$[7]	Bi_2O_3[8]	$(Bi_{19.68}Ni_{4.32})Ni_2O_{40}$[6]	$Mn(NiMn)O_4$[7]	Bi_2O_3[8]
a=b=c	10.113	8.383	11.047	10.112	8.365	11.084
α=β=γ	90^0					
Space group	I23	Fd-3mS	Fm-3	I23	Fd-3mS	Fm-3
Cell volume	1034.355	589.153	1348.269	1033.947	585.288	1361.556
Number of equivalent	24	192	96	24	192	96
Number of independent	24			24		

Table 6.4: Characteristics and properties of the obtained data from the structure refinement by Topas Academic software of $Bi_2Mn_xNi_{2-x}O_6$ when x=1.4 from experimental method 2.

The value of x	**1.4**		
Rwp	13.96%		
Properties	$Bi_{12}MnO_{20}$[4]	$Mn(NiMn)O_4$[7]	Bi_2O_3[9]
a	10.179	8.432	3.915
b			
c			6.289
α	90^0		90^0
β			
γ			120°
Space group	I23	Fd-3mS	P-3m1
Cell volume	1054.676	599.399	83.479
Number of equivalent positions	24	192	12
Number of independent parameters	24		

The refinement results here are for both experimental methods (1 and 2) and compare the synthesis via the ball mill grinding and manually grinding effect on the properties (in this section, structural properties) of all the samples. The powder diffraction results were further refined by the Topas academic software which has shown the crystal properties of each composition as shown in Figures (6.3) to (6.9).

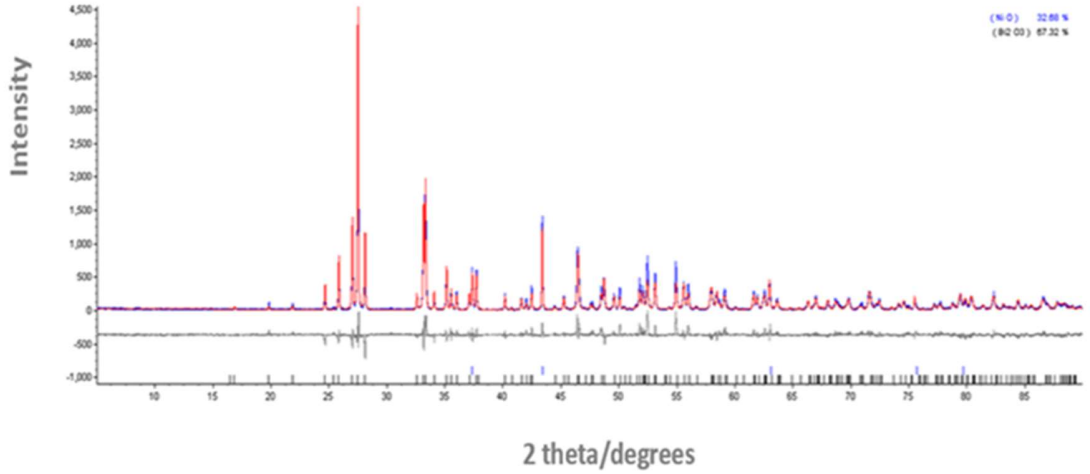

Figure 6.3: X-ray powder diffraction pattern Rietveld fit for $Bi_2Mn_0Ni_2O_6$ (x=0) from experimental method 1.

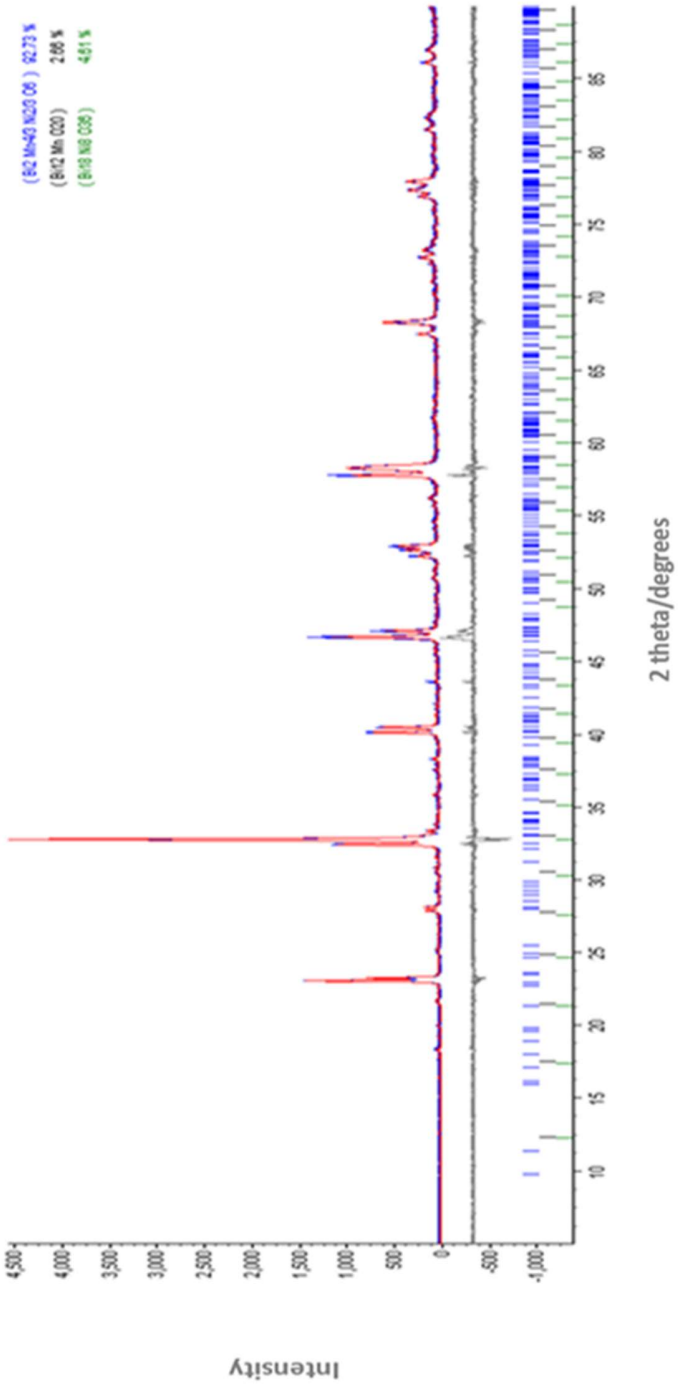

Figure 6.4: X-ray powder diffraction pattern Rietveld fit for $Bi_2Mn_{1.2}Ni_{0.8}O_6$ (x=1.2) from experimental method 1.

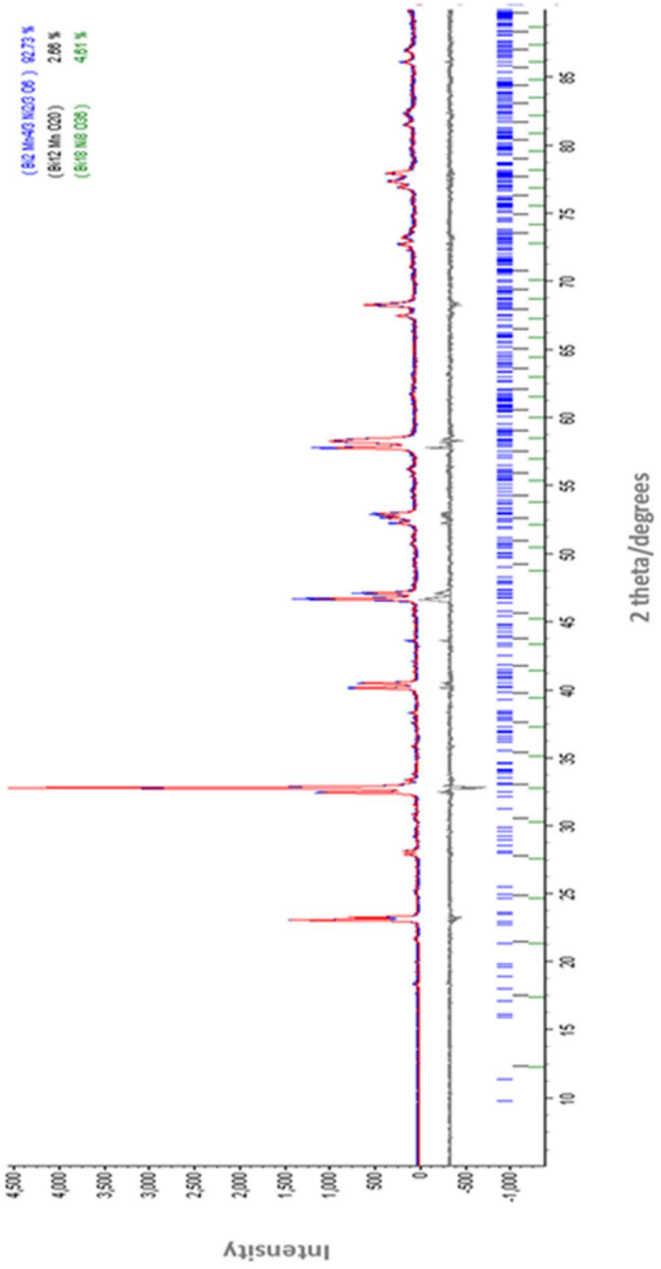

Figure 6.5: X-ray powder diffraction pattern Rietveld fit for $Bi_2Mn_{1.3}Ni_{0.7}O_6$ (x=1.3) from experimental method 1.

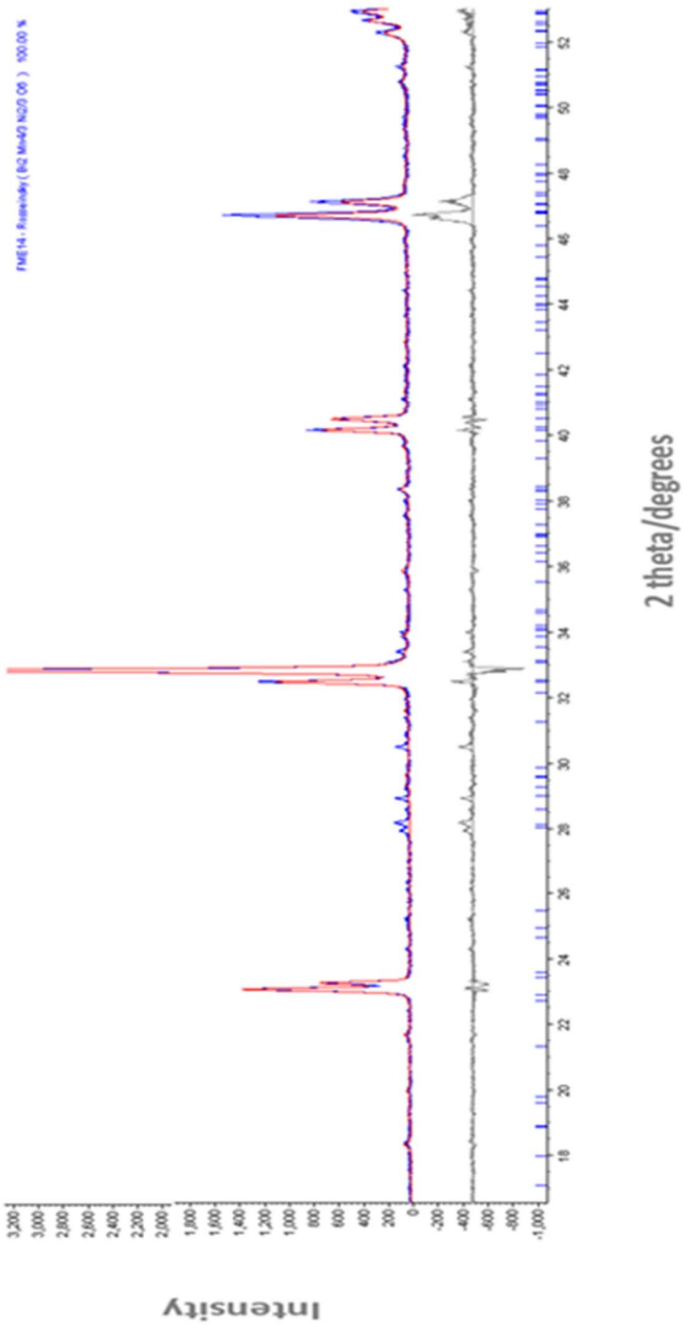

Figure 6.6: X-ray powder diffraction pattern Rietveld fit for $Bi_2Mn_{1.4}Ni_{0.6}O_6$ (x=1.4) from experimental method 1.

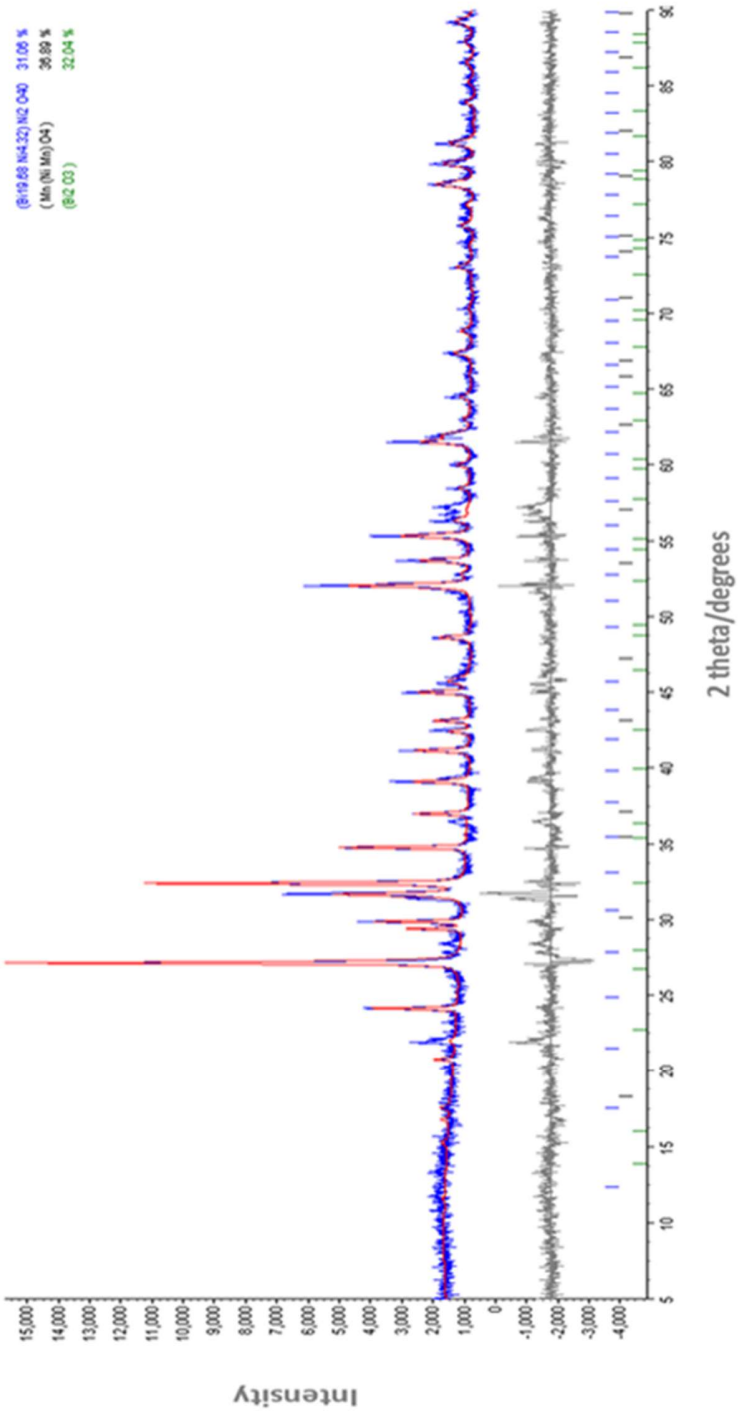

Figure 6.7: X-ray powder diffraction pattern Rietveld fit for $Bi_2Mn_{1.2}Ni_{0.8}O_6$ (x=1.2) from experimental method 2.

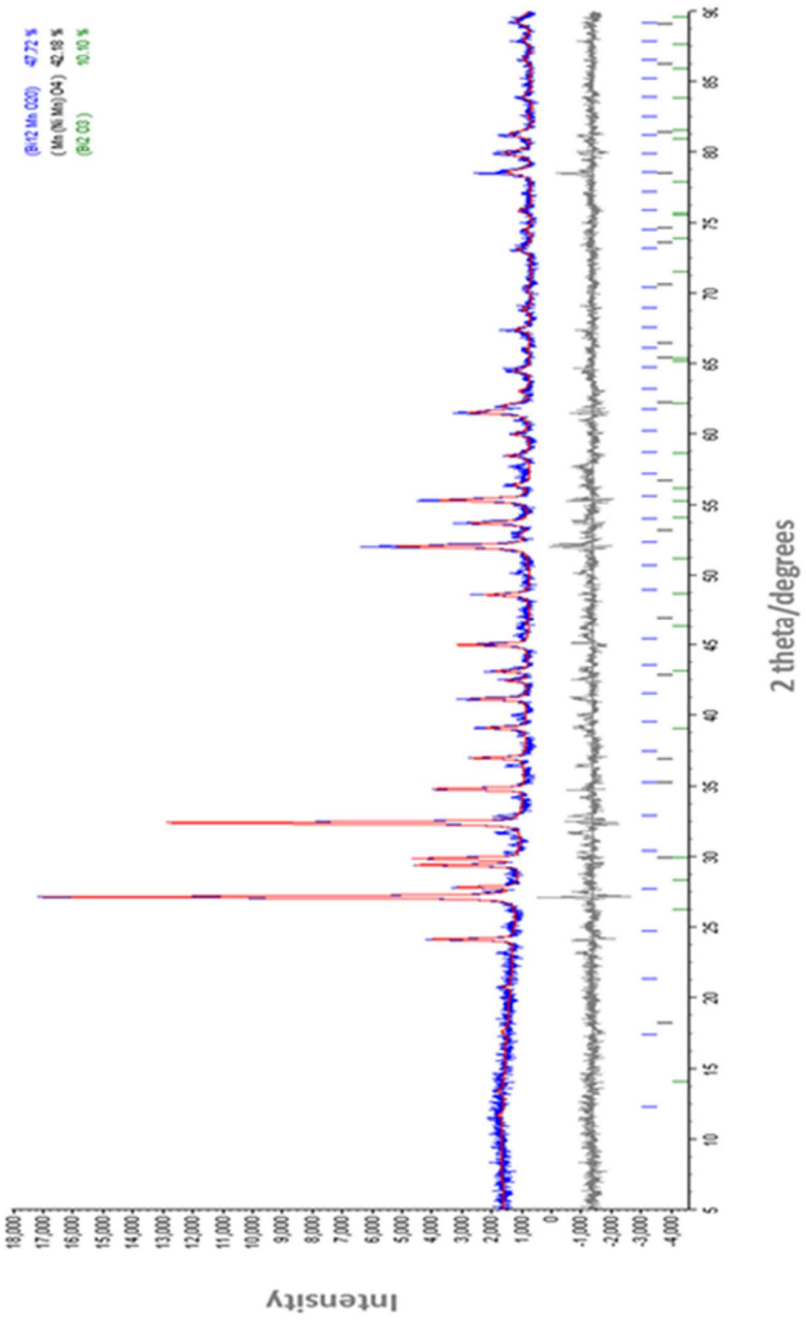

Figure 6.8: X-ray powder diffraction pattern Rietveld fit for $Bi_2Mn_{1.3}Ni_{0.7}O_6$ (x=1.3) from experimental method 2.

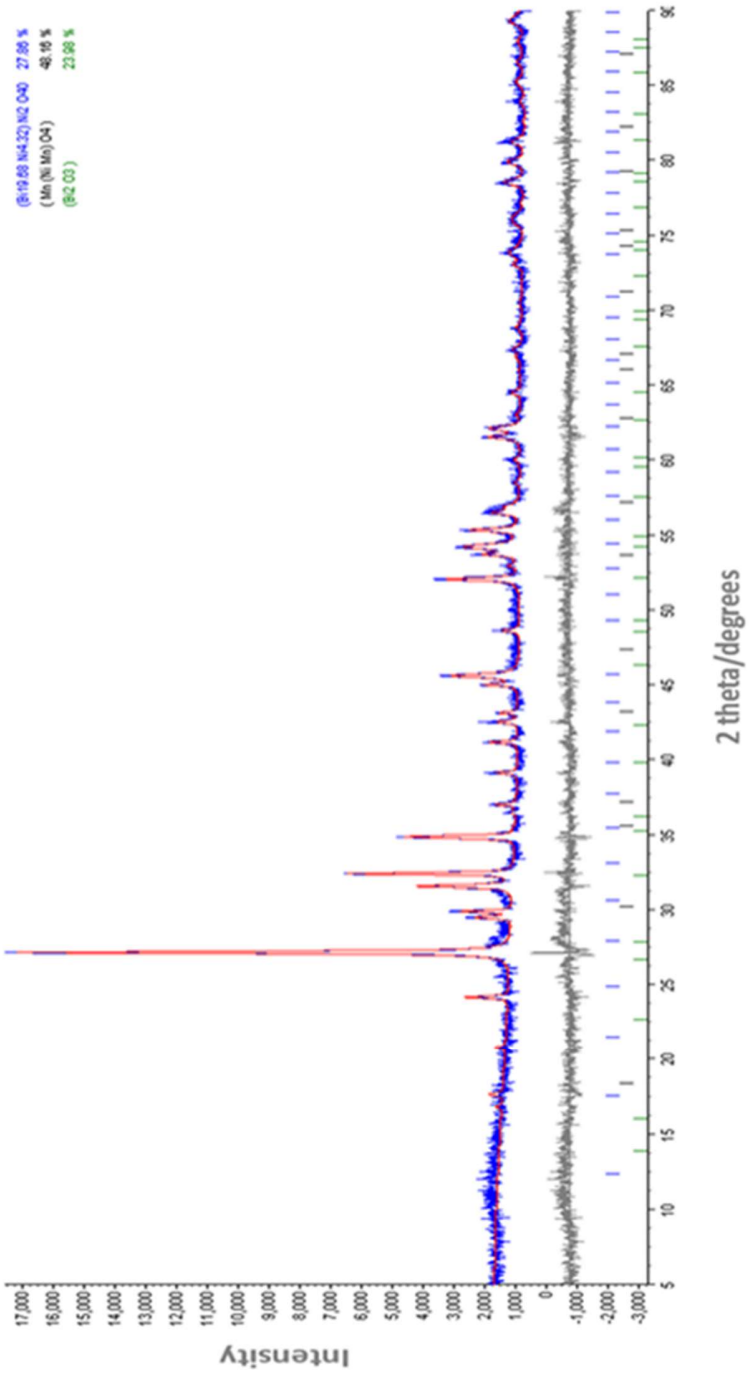

Figure 6.9: X-ray powder diffraction pattern Rietveld fit for $Bi_2Mn_{1.4}Ni_{0.6}O_6$ (x=1.4) from experimental method 2.

It can be seen that structure becomes distorted due to doping of Mn in $BiNiO_3$ system. The addition of Mn in the $BiNiO_3$ resulted in the formation of many variations and for that reason it was difficult to achieve single phase in any composition. The refinement of all the sample have shown to have monocline ($P121/c1$ space group) cubic crystal structure with ($I23$ and $Fm3m$) space group.

This can be seen that the intensity of peaks is decreased by the addition of Mn in $BiNiO_3$ systems. This can be due to the difference of ionic radius of Mn=0.645 nm and Ni= 0.069 nm and addition of Mn in crystal structure distorted the cell length.[2,3] Ni is basically a ferromagnet material, therefore when it is added to any material or any material added to its system, the properties are transferred to the material.[4] This is explained in the magnetic properties of $Bi_2Mn_xNi_{2-x}O_6$. Furthermore, the addition of Mn in the system contributes to the sharp increase of the oxygen vacancies in the $BiNiO_3$ system and resulted in a higher crystal structure distortion and deformation. The changing in doping concentration, changes the concentration of oxygen ions, and also the original tetrahedral radii of the Bi^{3+} and Ni^{2+} locations, contributes to the change in the parameters of crystal lattice[5] as explained in the refinement results. The extended peaks in X-ray diffraction pattern confirm the size of crystallites in nanometer. The intensity of X rays diffraction peaks decreases as well as the addition of NiO is decreased with increase in Mn resulted in the X-ray pattern as shown in figure (6.1) and figure (6.2).[6]

It can be seen that the refinement of experimental method 2 has better results from the experimental method 1. This can be attributed to fine grain size obtain from ball milling which resulted in better structural properties and ferroelectric properties (mentioned in the next section). The Mn addition has shown a variation in structure parameters of the samples of monoclinic to cubic with a distorted structure. The cell volume decreased with the increase in Mn content, and this indicate that the average ionic radii of Mn and Ni mismatch on unit cells

has dominated over the crystallite sizes and cell volumes. The decrease in volume cell can also be attributed the reason that dopant acts as inhibitors center for crystal size growth.[2, 7]

6.2 Dielectric measurement

Figure (6.10) shows the graphs of conductivity of $Bi_2Mn_xNi_{2-x}O_6$ compound by experiment 1 analysis. The graph shows the conductivity of $Bi_2Mn_xNi_{2-x}O_6$ compound as a function of value x from 0.0 to 2.0 at 750 ℃ temperature with different frequencies 1000 Hz, 10000 Hz and 100000 Hz. The graphs shows that conductivity increases with the increase in Mn content till the value x=1.4 and then starts decreasing. Also, as the frequency increases, the conductivity also increases. The increase in conductivity with the rise in frequency shows good conducting properties of material with the Mn addition and also shows good semiconductor nature of the $Bi_2Mn_xNi_{2-x}O_6$ compound with manual grinding.[8]

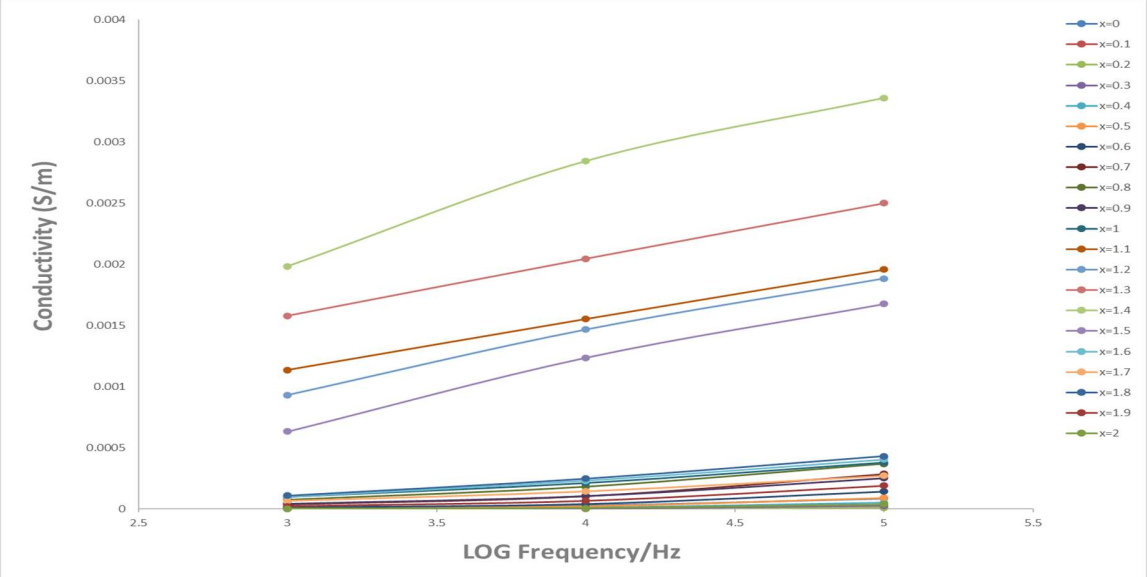

Figure 6.10: The electrical conductivity $Bi_2Mn_xNi_{2-x}O_6$ of experiment 1.

Figure (6.11) shows the conductivity of $Bi_2Mn_xNi_{2-x}O_6$ compound by experiment 2 analysis. The graph shows the conductivity of $Bi_2Mn_xNi_{2-x}O_6$ compound as a function of value x from 0.0 to 2.0 at 750^0C temperature at the range of frequencies from 1000 Hz, 10000 Hz and 100000 Hz.

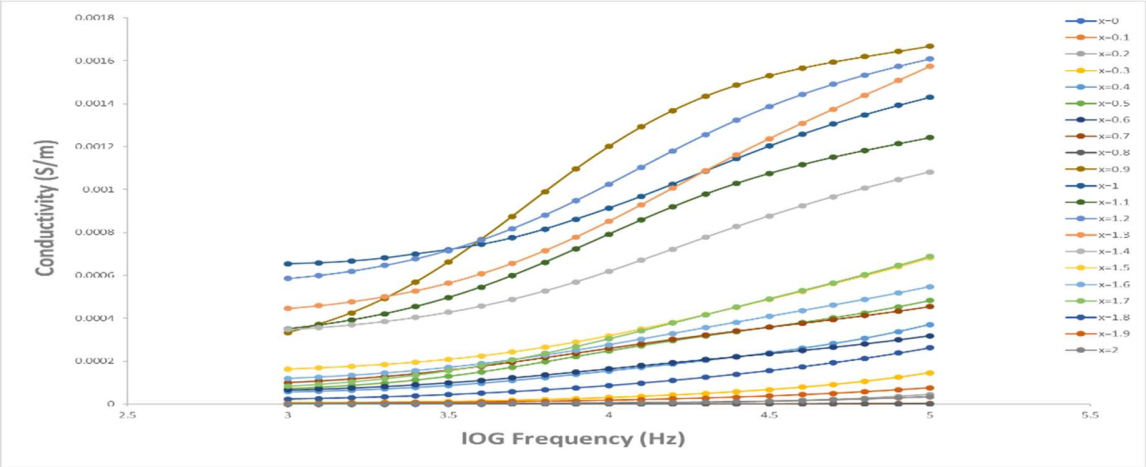

Figure 6.11: The electrical conductivity $Bi_2Mn_xNi_{2-x}O_6$ of experiment 2.

The graphs show conductivity increases with the increase in Mn content and as the frequency increases, conductivity also improves with the ball mill grinding. When comparing the results of conductivity of both experiments (1 and 2), the results obtained from experiment 2 (ball mill grinding) are better than the experiment 1 (manual grinding). This can be attributed to that ball mill grinding resulted in fine grains size which increases the surface energy of particles and the bond angle of Ni-O-Ni affected more by the fine grinding which resulted in asymmetry of the structure. This asymmetry improves the ferroelectric properties of materials and therefore improved conductivity resulted by the ball mill grinding of perovskite samples.[9-11]

In general, the response of conductivity by increasing frequency in multiferroics can be attributed to the hopping or polaron (quasi particles) mechanisms of free charge carriers in the material. When electric field is applied, the movement of

electrons in perovskite tends to polarize or distort the nearby lattice to form polarons. If this distortion/deformation is along the lattice of the order of lattice constant, the small polarons are formed while the formation of large polarons occurs when the distortion exceeds beyond the lattice constant. Large polaron are normally responsible when the conductivity is decreasing with increase in frequency and the small polaron are explains the behavior of increasing conductivity with increase in frequency.[12, 13] Also, it can be seen in the graph's conductivity is increasing with the frequency which confirms that conduction mechanism is largely because of small mechanisms arising from the charge carrier movement such as Mn^{3+}, Mn^{4+} only. And slight variation in linearity in both graphs is because of the mixed polarons (small/large) conduction which originates from the possible existence of Bi/O vacancies by Bi evaporation excluding the charge carriers mentioned-above.[14]

The data of dielectric constant and dielectric loss was obtained from LCR meter, at 750 ℃ temperature for $Bi_2Mn_xNi_{2-x}O_6$ for vales x=0.0 to 2.0 at the frequency 1 kHz, 100 kHz and 100 kHz for experimental method 1 and at a range of frequency from 1 kHz to 100 kHz from experimental method 2 has been displayed in Figure (6.12) and (6.13).

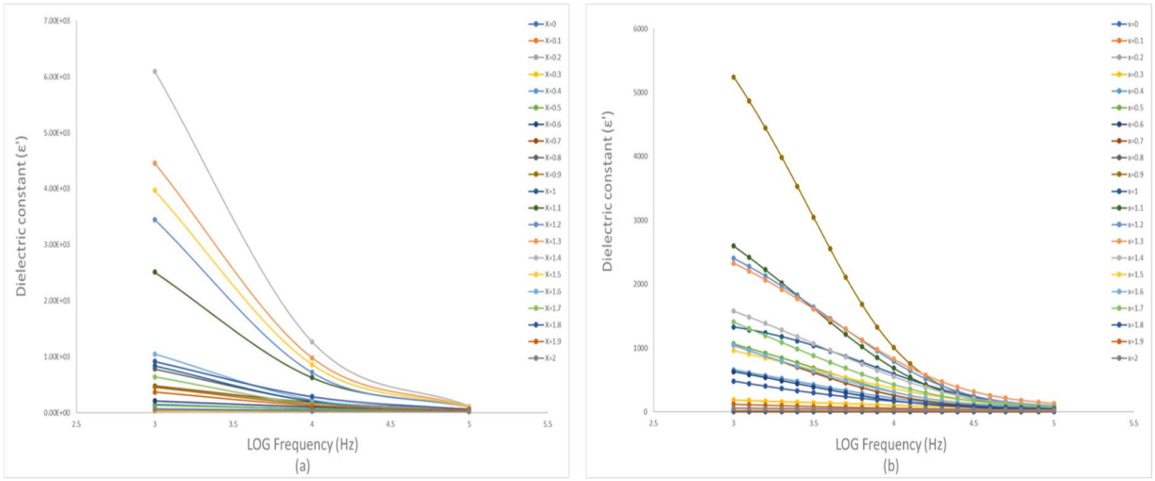

Figure 6.12: The dielectric constant $Bi_2Mn_xNi_{2-x}O_6$ of (a) experiment 1, (b) experiment 2.

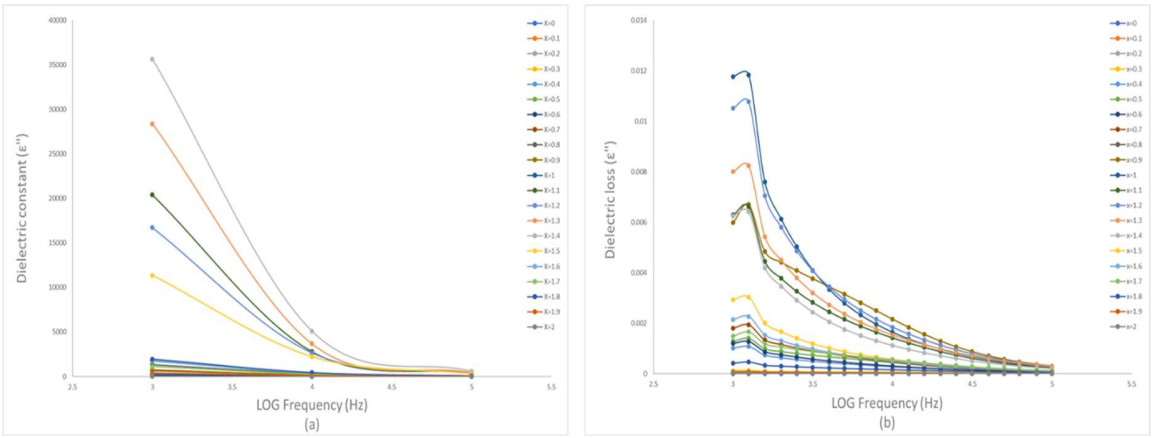

Figure 6.13: The dielectric loss $Bi_2Mn_xNi_{2-x}O_6$ of (a) experiment 1, (b) experiment 2.

The dielectric constant and dielectric loss as a function of frequency shows that addition of Mn increases the dielectric properties till x= 1.5 and then starts decreasing from experimental 1. This is also to be mentioned here that dielectric properties are decreasing with the increase in frequency.

Figure shows the values of dielectric loss and dielectric constant for $Bi_2Mn_xNi_{2-x}O_6$ compound as function of x for experimental method 2. This can be seen in the graphs that values of dielectric constant increasing with the increase in Mn content but decreasing with increase in frequency. When comparing the graphs of dielectric loss and dielectric constant as function of x=0.0 to x=2.0 for experimental method 1 and 2, the method 2 seems to have better dielectric properties. This can be due to the ball mill grinding resulted in fine grains size which increases the surface energy of particles and the bond angle of Ni-O-Ni affected more by the fine grinding which resulted in asymmetry of the structure. This asymmetry improves the ferroelectric properties of materials and therefore improved conductivity resulted by the ball mill grinding of perovskite samples.[9-11] Also, ball mill has better effects on the charge in the materials due to the impedance of this carriers transport in nanostructure.[1]

The values of dielectric loss and dielectric constant for both experimental results are decreasing with the increase in frequency an become almost constant or decreasing slowly as can be seen in figures (6.12) and (6.13) can be attributed to the behavior of bi-based perovskite explained by the Maxwell-Wagner two-layer model and Koop's theory. The non-homogenous structures of the dielectric materials are expected to have good electrical conducting behavior of grains separated by a thin grain boundary which is resistive in nature. And in this case, when the voltage applied to the materials is become reduced by passing through the grain boundaries and forming a polarization of space charges over the grain boundaries. This space charge polarization is normally controlled by the free charges that are present in the grain boundaries and by the electrical conductivity of the material. In accordance with the Koop's theory, the dielectric constant in lower frequencies is originated from the grain boundaries because the presence of high electrical resistivity in the grain boundaries results in higher dielectric constant values at lower frequencies. Furthermore, the dielectric constant in the higher frequency is originated from the grains resulted in the lower dielectric constant at high frequencies. As a result, the values of the dielectric loss and dielectric constant are low at high frequencies. And these values are high frequency due to might also have some affects from oxygen vacancies, dislocations, impurities, and structural defects.[9-11]

6.3 Scanning Electron Microscopy and Energy Dispersive X-Ray Spectroscopy

The SEM analysis was conducted on the $Bi_2Mn_xNi_{2-x}O_6$ on the value of x=1.3 this sample was prepared by the ball mill grinding and mixing to determine the effect of nickel doping concentration on the microstructural properties of the perovskite compound. The SEM result has been illustrated in Figure (6.14).

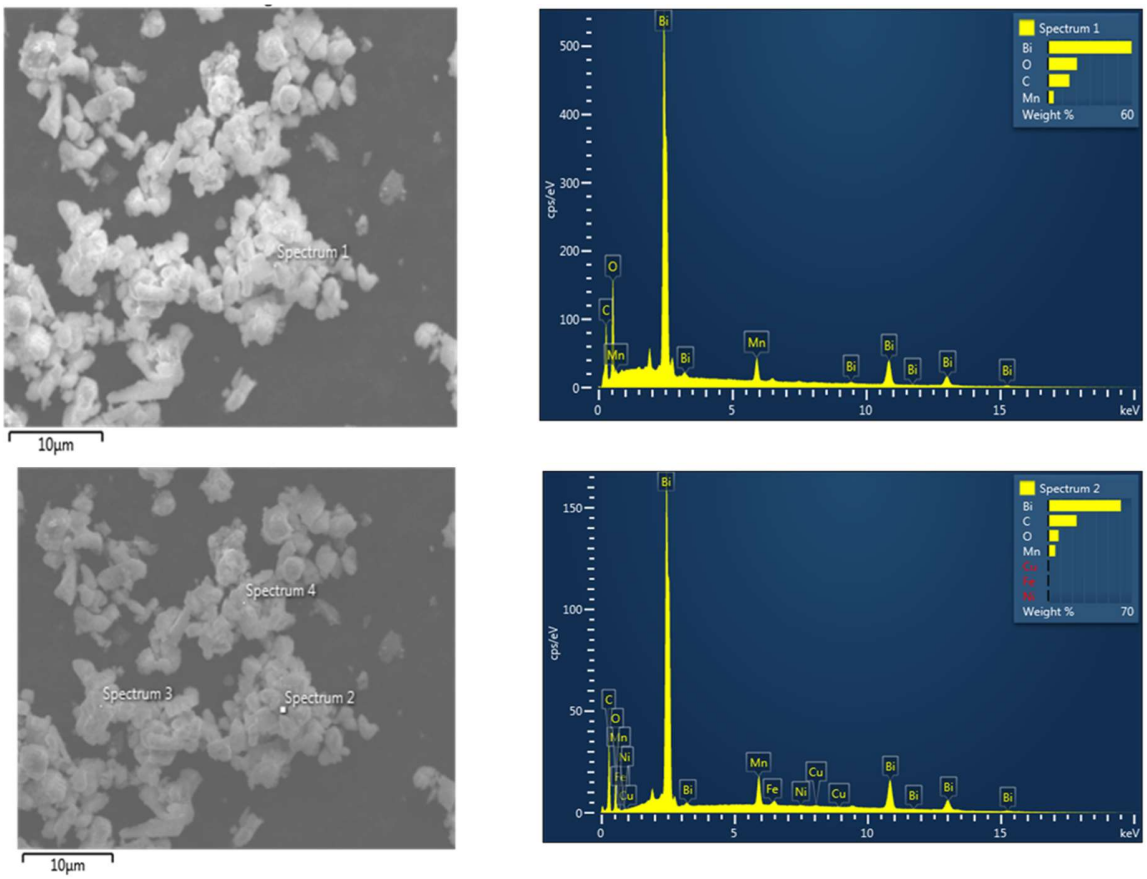

Figure 6.14: SEM images of $Bi_2Mn_xNi_{2-x}O_6$ on the value of x=1.3.

In Figure (6.14) it can be that all nickel concentrations have formed aggregates of polyhedral and rounded grains and the with different particle size distribution ranging from 0.3 to 4.0 μm approximately. It is expected that this grain size would further be increased in the composition with high Mn amount as confirmed by the reports Khajonrit *et al*.[15] The increase in crystallite size with the decrease in nickel content, as a result of grain growth-inhibitor effect of Ni^{2+} due to the surface energy of the Ni doped Bi-based systems[16] and the precipitation of manganese-nickel oxides phases at the grain boundaries, restraining the grain growth and reducing the grain sizes during the sintering of material. The EDX analysis also performed to confirm the presence of various compound and these results are in agreement with the Rietveld analysis. Furthermore, the different morphology of grain in graphs has been observed as the grain size is not smooth and inhomogeneous structure with lower grain size. This can be attributed to the

presence of different phase as confirmed by refinement with different cell volume and crystallite size. In this particular composition, the bigger size grain would be associated with the impurities like $Bi_2Mn_{\frac{4}{3}}Ni_{\frac{2}{3}}O_6$ and $Bi_{18}Ni_8O_{36}$. With high cell volume and the larger phase are precipitated through α-Bi- based oxides which acts as a nuclei agent of the transformation.[17].

6.4 UV-vis Spectroscopy

The figure (6.15), and show the graphs of UV-vis spectroscopy of $Bi_2Mn_xNi_{2-x}O_6$ as a function of wavelength of different value of x=0.0-2.0 for both experimental methods 1 and 2. It can be seen in both graphs that the all the sample in both methods have the samples have broad peaks in the ultraviolet region (about 400 nm) and this is displace to a lower wavelength as the amount of Mn is increasing in the samples which is known to have displacement of blue shift. This shift can be due to the smaller size of the particles.

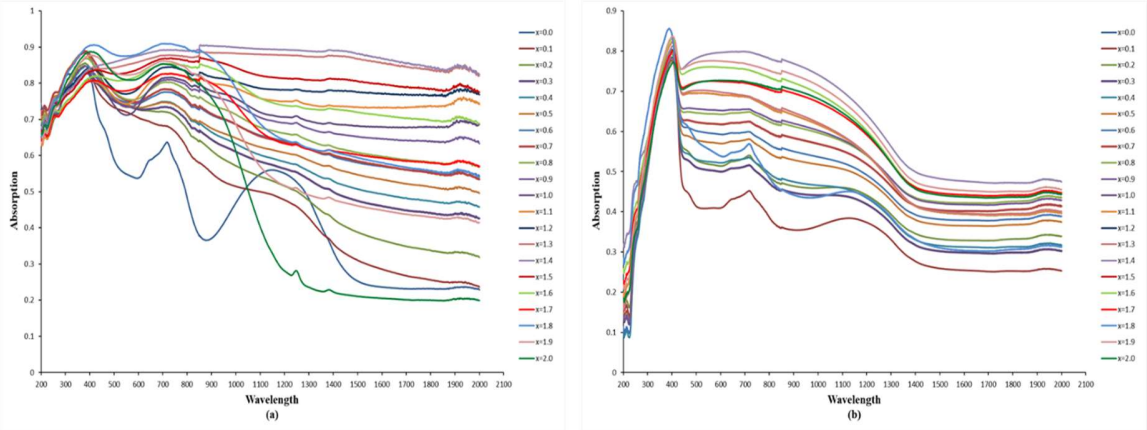

Figure 6.15: The UV-vis data of $Bi_2Mn_xNi_{2-x}O_6$ of (a) experiment 1, (b) experiment 2.

The difference of both experimental method 1 and 2 in the UV-vis spectroscopy of $Bi_2Mn_xNi_{2-x}O_6$ is the intensity of peaks. In experimental method 2, figure has more intense peak as compared to method 1. The increases in intensity of peaks are due to the distortion in bond angle of $[BiO_6]$-$[BiO_6]$ clusters that is resulted

by the addition of Mn in the compound and forming $[BiO_6]$-$[Mn_x/Ni_x$-$O_y]$ clusters.[18] The charge carriers prefer to make transitions to the conduction band from cluster transition energy level, which acts as prominent transition states, because this required less energy.[19,20]

6.5 FT-IR Spectroscopy

In general, the FT-IR analysis provides a good estimation of presences of various bonds (metallic and non-metallic) and confirms the reaction occurrence between the elements (like in case of doping) depending on the types of samples. The FT-IR analysis for x=0.0, 1.2, 1.3 and 1.4 are shown in Figure (6.16).

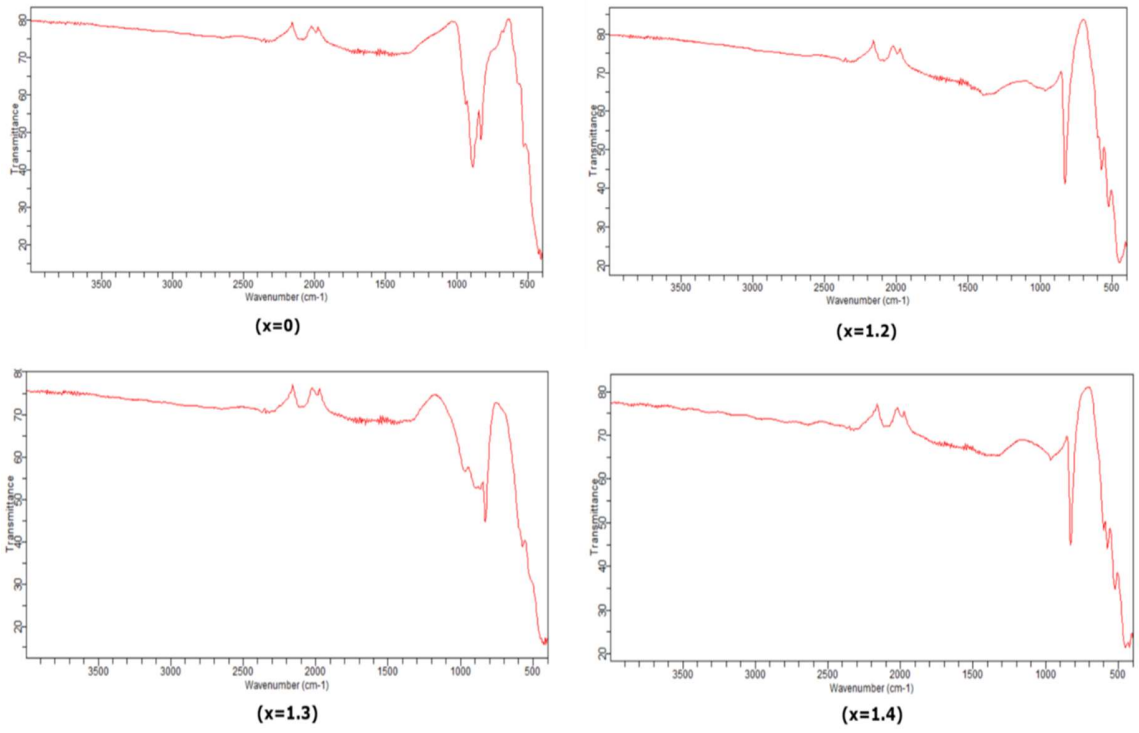

Figure 6.16: The FT-IR $Bi_2Mn_xNi_{2-x}O_6$ of experiment 2.

In this work, the FT-IR analysis is carried out on the selected samples of experimental method 2 which are x=0,1.2, 1.3 and 1.4 that are in agreement

with the XRD results and have shown some interesting properties as discussed in XRD. The compounds being metallic in nature, therefore, metal oxide bonds are present which normally dominant in the range of 200-800 cm^{-1}. The peaks present at around 600 cm^{-1} for x=0.0 in figure and around 700 cm^{-1} for the value of x=1.2, 1.3 and 1.4 confirms the bending vibration of Bi-O bond in all the compounds. The peaks visible at around 800-900 cm^{-1} show the stretching of Bi-O-Bi bonds in all the graphs. The addition of Mn does not affect the $BiNO_3$ but shift the peak bands with the increase in Mn content. And the intensity of peak is increased with Mn addition which confirms the metal-oxide-metal bond interactions.[21, 22] The peaks present at around 1300cm^{-1} confirms the presence of nitrate group in all the samples.[23,24] Other than that the weak peaks present in the range of 1800 cm^{-1} - 2200 cm^{-1} is related to the thermal conditions of the samples while FT-IR analysis as reported in the research.[25] Therefore, it can be said the peak shifting towards loner wavelength conforms the interaction of bonds occurred by adding Mn in $BiNiO_3$.

6.6 Magnetic moment measurements

The magnetic susceptibility and effective magnetic moment were determined from Magneto moment spectroscopy for $Bi_2Mn_xNi_{2-x}O_6$ compound at room temperature as a function of x for both experimental methods 1 and 2. Figure and show the Magneto moment spectroscopy for $Bi_2Mn_xNi_{2-x}O_6$ compound as a function of x for experimental method 1 as has been illustrates in Figure (6.17) and (6.18).

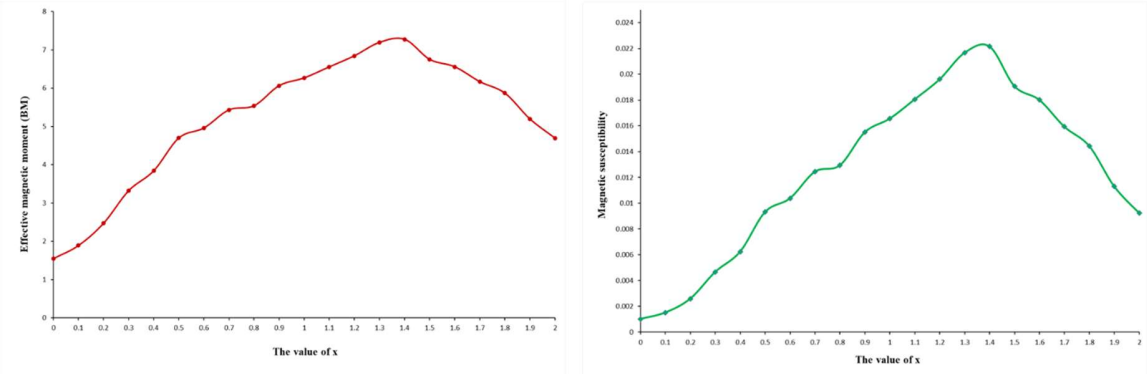

Figure 6.17: The magnetic susceptibility and effective magnetic moment of $Bi_2Mn_xNi_{2-x}O_6$ combination of all value of x (0.0 to 2.0) in experiment 1.

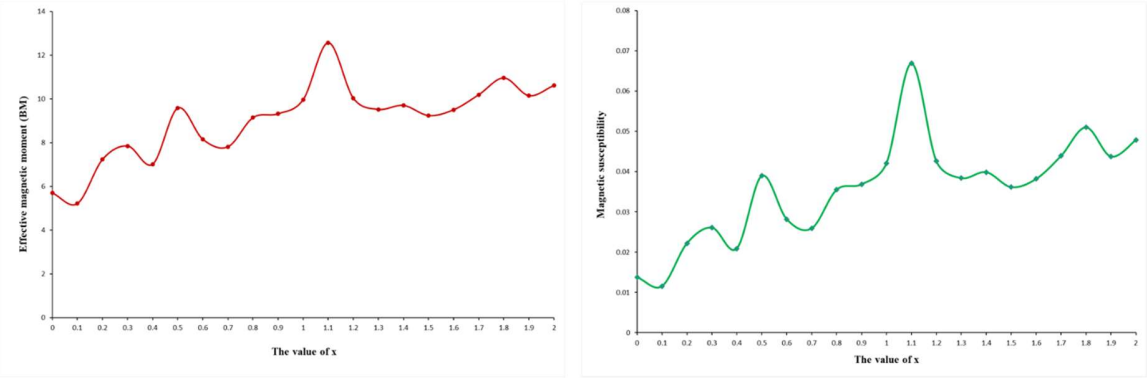

Figure 6.18: The magnetic susceptibility and effective magnetic moment of $Bi_2Mn_xNi_{2-x}O_6$ combination of all value of x (0.0 to 2.0) in experiment 2.

It can be seen that magnetic properties are improved with the addition of Mn till the value x=1.5. This trend is in agreement of dielectric properties of this sample. The addition of Mn transformed the samples from antiferromagnetic to ferromagnetic and the ferromagnetic properties become improved. Figure and show the Magneto moment spectroscopy for $Bi_2Mn_xNi_{2-x}O_6$ compound as a function of x (0.0 to 2.0) for experimental method 2. The magnetic properties are improved with the addition of Mn and transformed the samples from antiferromagnetic to ferromagnetic and the ferromagnetic properties are gradually improved. When the magnetic properties of both experimental method 1 and 2 are compared, the experimental method 2 has better magnetic properties than method 1. The reason is the decrease in particle size and crystallite size due to ball milling has exhibited strong ferromagnetic properties

The magnetic properties of $Bi_2Mn_xNi_{2-x}O_6$ compound as a function of x (0.0 to 2.0) are observed to be increasing in both cases. There could be four reasons for this improvement of magnetic properties at room temperature of Mn-doped samples in BNO material. The first reason is high magnetic of moment of the Mn ($5\mu B$)[11] as compared to Ni($3.5\mu B$).[26] The second reason in increasing the magnetic properties of the samples is the smaller the size of their nanoparticles which in experimental method was greater. When the Mn amount is added to the sample,

the average nanoparticles is decreased which prevents the spin rotational period from completion in bi-base compound and therefore the macroscopic magnetization in the samples is increased. The third reason is the change in bond angle of O-Ni-O and results in greater distortion and samples become asymmetric which further results in improved magnetic properties. And lastly, it can be because of change of crystal structure from monoclinic to cubic.[27,28]

References

[1] R. W. Cairns, and E. Ott, *J. Am. Chem. Soc.*, 1933, **55**, 527-533.

[2] L.G. Sillén, *Naturwissenschaften*., 1940, 28, 206-207.

[3] J. B. Claridge, H. Hughes, C. A. Bridges, M. Allix, M. R. Suchomel, H. Niu, X. Kuang, M. J. Rosseinsky, N. Bellido, D. Grebille, O. Perez, C. Simon, D. Pelloquin, S. J. Blundell, T. Lancaster, P. J. Baker, F. L.Pratt, and P. Shiv Halasyamani, *J. Am. Chem. Soc.*, 2009, **131**, 14000 – 14017.

[4] U. Delicat, S. F .Radaev, M.Troemel, P. Behrens, Yu. F. Kargin and A. A. Marin, *Journal of Solid State Chemistry*., 1994, **110**, 66-69.

[5] A. Ramnan, J. Gopalakrishna., and C.N.R. Rao, Materials Research Bulletin., 1981, 16, 169 -174.

[6] N. Rangavittal, T. N. Guru Row, and C. N. R. Rao, *European Journal of Solid State Inorganic Chemistry*., 1994, **31**, 409-422.

[7] P. K. Baltzer, and J. G. White, *Journal of Applied Physics.*, 1958, **20**, 445-447.

[8] D. S. Aidhy, S. B. Sinnott, E. D. Wachsman, S. R. Phillpot, and J. C. Nino, *Journal of Solid State Chemistry*., 2009, **182**, 122 -1228.

[9] T. Atou, H. Faqir, M. Kikuchi, H. Chiba, and Y. Syono, *Materials Research Bulletin.,* 1998, **33**, 289-292.

[10] S. Seo, Y. Jeong, M.-W. Oh and B. Yoo, *Journal of Alloys and Compounds.*, 2017, **706**, 576-583.

[11] Y. Han, Y. Ma, C. Quan, N. Gao, Q. Zhang, W. Mao, J. Zhang, J. Yang, X. a. Li and W. Huang, *Ceramics International.*, 2015, **41**, 2476-2483.

[12] C. Regmi, Y. K. Kshetri, T.-H. Kim, R. P. Pandey, S. K. Ray and S. W. Lee, *Applied Surface Science.*, 2017, **413**, 253-265.

[13] C. Regmi, T.-H. Kim, S. K. Ray, T. Yamaguchi and S. W. Lee, Research on Chemical Intermediates., 2017, **43**, 5203-5216.

[14] M. Zdorovets and A. Kozlovskiy, *Ceramics Internationa.l*, 2020, **46**, 14548-14557.

[15] S. Trukhanov, V. Fedotova, A. Trukhanov, S. Stepin and H. Szymczak, *Crystallography Reports.*, 2008, **53**, 1177-1180.

[16] P. Achary, S. K. Dehury and R. Choudhary, *Journal of Materials Science: Materials in Electronics*., 2018, **29**, 6805-6816.

[17] M. Padhy, S. K. Dehury, R. Choudhary and P. *Achary, Applied Physics A*., 2020, **126**, 1-13.

[18] H. Shokrollahi, *Powder technology*., 2013, **235**, 953-958.

[19] R. Safi and H. Shokrollahi, *Progress in Solid State Chemistry.*, 2012, **40**, 6-15.

[20] S. E. M. Ghahfarokhi, M. R. Larki and I. Kazeminezhad, *Vacuum*., 2020, **173**, 109143.

[21] D. Adler and J. Feinleib, *Physical Review B.*, 1970, **2**, 3112.

[22] I. Austin and N. F. Mott, *Advances in physics.*, 1969, **18**, 41-102.

[23] S. Mazumdar, M. Khan, M. F. Islam and A. A. Hossain, *Journal of Magnetism and Magnetic Materials*., 2015, **390**, 61-69.

[24] J. Khajonrit, N. Prasoetsopha, T. Sinprachim, P. Kidkhunthod, S. Pinitsoontorn and S. Maensiri, *Advances in Natural Sciences: Nanoscience and Nanotechnology*., 2017, **8**, 015010.

[25] M. Biswal, J. Nanda, N. Mishra, S. Anwar and A. Mishra, *Adv. Mater. Lett*., 2014, **5**, 531-537.

[26] L. Betancourt-Cantera, A. Bolarín-Miró, C. Cortés-Escobedo, L. Hernández-Cruz and F. Sánchez-De Jesús, *Journal of Magnetism and Magnetic Materials*., 2018, **456**, 381-389.

[27] S. Schmidt, E. T. Kubaski, D. P. Volanti, T. Sequinel, V. D. N. Bezzon, A. Beltrán, S. M. Tebcherani and J. A. Varela, *Inorganic Chemistry*., 2015, **54**, 10184-10191.

[28] S. Singh, R. Sharma, G. Joshi and J. K. Pandey, *Korean Journal of Chemical Engineering*., 2017, **34**, 500-510.

[29] S. Singh, R. Pendurthi, M. Khanuja, S. Islam, S. Rajput and S. Shivaprasad, *Applied Physics A*., 2017, **123**, 1-10.

[30] L. Liu, J. Jiang, S. Jin, Z. Xia and M. Tang, *CrystEngComm*., 2011, **13**, 2529-2532.

[31] T. Liu, Y. Zhao, L. Gao and J. Ni, *Scientific reports.*, 2015, **5**, 1-5.

[32] K. Saravanakumar, M. M. Ramjan, P. Suresh and V. Muthuraj, *Journal of Alloys and Compounds.*, 2016, **664**, 149-160.

[33] C. García-Ruiz, *Advances in Materials Science Research. Nova Science Publishers: New York, USA*., 2012, **7**, 202-220.

[34] N. Omrani and A. Nezamzadeh-Ejhieh, *Journal of Molecular Liquids*., 2020, **315**, 113701.

[35] W. Ferenc, A. Walków-Dziewulska, J. Sarzynski and B. Paszkowska, *Eclética Química*., 2006, **31**, 53-59.

[36] T.-J. Park, G. C. Papaefthymiou, A. J. Viescas, A. R. Moodenbaugh and S. S. Wong, *Nano letters*., 2007, **7**, 766-772.

[37] S. Chauhan, M. Kumar, S. Chhoker, S. Katyal, H. Singh, M. Jewariya and K. Yadav, *Solid State Communications.*, 2012, **152**, 525-529.

7.Conclusions and Future Works

7.1 Conclusions

This work was focused on the Perovskite materials that have ferroelectric and ferromagnetic properties simultaneously which are known as multiferroic materials. The quaternary perovskite oxides were prepared with the composition of $Bi_2Mn_xCo_{2-x}O_6$, $Bi_2Mn_xNi_{2-x}O_6$ and $Bi_2Cr_2Ni_{2-x}O_6$. Total nine compositions were prepared with the 21 different combinations depending on the varying value of x but 3 are presented here because of obtaining satisfactory results.

Solid state method was used to prepare the samples at three different sintering temperatures 800 ^{0}C, 850 ^{0}C and 875 ^{0}C at ambient pressure to determine the effect of sintering temperature on the varying value of x in the perovskite structure. The characterization techniques used to determine the properties of these compounds are X-ray diffraction and Rietveld refinement for structural analysis, Dielectric measurement for electrical properties, Magnetic moment spectroscopy for magnetic properties, Fourier transform infra-red spectroscopy (FT-IR) and UV-vis spectroscopy for optical properties and Scanning electron microscopy for microstructural properties.

The analysis of $Bi_2Mn_xCo_{2-x}O_6$ has showed different properties. XRD and Rietveld analysis has confirmed the presence of multiple phases in all the compositions and no single phase was achieved. The reason is the utilization of ambient pressure in the synthesis which could not stabilize the perovskite structure. The dielectric constant and dielectric loss as a function of frequency from 1 kHz, 10 kHz and 100 kHz at constant temperature of 750 ^{0}C was observed to be decreasing with the increase in frequency and Mn content. The capacitance,

conductance and conductivity were decreased with the increase in Mn content compound at 750ºC temperature in $Bi_2Mn_xCo_{2-x}O_6$. Mn doping in the $BiCoO_3$ perovskite resulted in less ferroelectric properties because of the weak hybridization between the Mn and O ions. The magnetic moment analysis at room temperature of $Bi_2Mn_xCo_{2-x}O_6$ compound showed that this antiferromagnetic material becomes ferromagnetic with the increasing content of Mn. The reason of being ferromagnetic is the volatile nature of Bi and the involvement of high temperatures in sintering which make the presence of oxygen vacancies almost predictable in the Bi-based perovskite.

The analysis of $Bi_2Mn_xZn_{2-x}O_6$ has revealed many interesting properties. The XRD analysis confirmed that structure is highly distorted due to doping of Mn in $BiZnO_3$ system. The addition of Mn in the $BiZnO_3$ resulted in the formation of many impurities and it was difficult to achieve single phase in any composition. Furthermore, the peaks confirmed the presence of tetragonal and orthorhombic crystal structure. The dielectric measurement showed that the Capacitance (pF), Conductance (μS) and conductivity (μS/cm) of x values at 750ºC at different frequencies 1000 Hz, 10000 Hz and 100000 Hz of $Bi_2Mn_xZn_{2-x}O_6$ perovskite increased with the increase in Mn content in $BiZnO_3$. This compound has better conductive properties the Mn addition and also revealed semiconductor nature of the compound. The dielectric constant and dielectric constant increased with the increasing content of Zn but decreasing with the frequency. The magnetic moment analysis at room temperature of $Bi_2Mn_xZn_{2-x}O_6$ perovskite has showed that magnetic moment increases with the increase in Mn content. This is due to that the Mn addition which distorted the spiral spin structure and also decreases the crystallite size. The UV-vis spectroscopy showed the potential volatility of the crystalline structure and the local atomic arrangement of the compound and confirmed the reduction in band gap.

The $Bi_2Mn_xNi_{2-x}O_6$ prepared from the solid state synthesis method was with two variations; manually grinding (experiment 1) and the ball mill grinding (experiment 2) for samples mixing. The overall results of experimental method 2 were better from the experimental method 1. This is due to the fine grain size obtaining from ball milling which resulted in better structural properties. The XRD results showed that the addition of Mn in the $BiNiO_3$ resulted in the formation of many impurities and for that reason it was difficult to achieve single phase in any composition. The refinement of all the sample have shown to have monocline and cubic crystal structures. The dielectric results of both experiments (1 and 2) have shown that ball mill grinding resulted in fine grains size which increases the surface energy of particles and also the bond angle of Ni-O-Ni affected more by the fine grinding which resulted in asymmetry of the structure. The SEM analysis was conducted on the $Bi_2Mn_xNi_{2-x}O_6$ for x=1.3 by the ball mill grinding and showed that the Ni content has formed aggregates of polyhedral and rounded grains and the with different particle size distribution ranging from around 0.3 to 4.0μm. The UV-Vis spectroscopy of both experimental method 1 and 2 has showed that method 2 has more intense peak as compared to method 1. The increases in intensity of peaks are due to the distortion in bond angle of $[BiO_6]$-$[BiO_6]$ clusters that is resulted by the Mn addition and forming [BiO6]-$[Mn_x/Ni_x\text{-}O_y]$ clusters. The FT-IR analysis has shown that the peak shifting towards lower wavelength confirms the interaction of bonds occurred by adding Mn in $BiNiO_3$. The magnetic properties were observed to be improved with the addition of Mn and transformed the samples from antiferromagnetic to ferromagnetic properties which further improved gradually. The experimental method 2 has better magnetic properties than method 1 because of the decrease in particle size and crystallite size due to ball milling which showed strong ferromagnetic properties.

7.2 Future work

The recommendations for future work for this thesis are as:

It is recommended to change the pressure along with the temperature during synthesis because Bi-based perovskite requires high pressure combined with high temperature to produce a Perovskite and obtain single phase structure.

It is also recommended to conduct SEM analysis on every composition because grain size has major effect on the dielectric and structural properties which could not be full identified because of the unknown grain size

It is recommended to conduct analysis for the study of grain and grain boundaries such as impendence spectroscopy and its effect on the dielectric properties because most of the feature remained unknown due to absence of the knowledge of grain and grain boundaries conductivity.

It is recommended to add more compounds in the future studies because the substitution of elements on A-site Bismuth (Bi^{+}) of perovskite such as lead (Pb^{+}) and tin (Sn^{+}) because these are known to have more interesting effect on the ferroelectric and ferromagnetic properties.